Synthesis, Structure and Relaxor to Ferroelectric Crossover in the Lead-Strontium Zirconate-Titanate Perovskite Solid Solution System

by

Wenhan Dong

B.Sc., University of Waterloo, 2017

Thesis Submitted in Partial Fulfillment of the
Requirements for the Degree of
Master of Science

in the
Department of Chemistry
Faculty of Science

SIMON FRASER UNIVERSITY
Spring 2021

Declaration of Committee

Name:	**Wenhan Dong**
Degree:	**Master of Science (Chemistry)**
Title:	**Synthesis, Structure and Relaxor to Ferroelectric Crossover in the Lead-Strontium Zirconate-Titanate Perovskite Solid Solution System**
Committee:	**Chair: Paul C.H. Li** Professor, Chemistry
	Zuo-Guang Ye Supervisor Professor, Chemistry
	Hua-Zhong Yu Committee Member Professor, Chemistry
	Corina Andreoiu Committee Member Professor, Chemistry
	Krzysztof Starosta Examiner Professor, Chemistry

Abstract

In order to investigate the structures and physical properties of intriguing relaxor ferroelectrics, a novel solid solution, $(1-x)(Pb_{0.5}Sr_{0.5})(Zr_{0.5}Ti_{0.5})O_3$-$xPbTiO_3$ (PSZT-PT), of complex perovskite structure was synthesized by solid-state reaction method. The ceramics of the PSZT-PT system were characterized by X-ray diffraction (XRD), dielectric spectroscopy, ferroelectric testing and transmission electron microscopy (TEM). Detailed structural analyses based on the refinements of XRD patterns by both the Pawley and Rietveld methods reveal a structural transformation from the cubic to tetragonal symmetry as the concentration of PT (x) increases, with a mixture of the two phases in the composition range of $x \approx 0.10 \sim 0.25$.

Subsequently, the dielectric properties of the PSZT-PT solid solution were characterized as a function of temperature at various frequencies (10 Hz to 1 MHz). The results indicate a crossover from typical relaxor behaviour to normal ferroelectric state with increasing concentration of PT. The characteristics of relaxor behaviour and its evolution were analyzed by the Vogel-Fulcher law and Curie-Weiss law in terms of the dielectric peak temperature (T_{max}) shift with frequency, the freezing temperature (T_f) and the Burns temperature (T_B). Furthermore, the measurements of polarization versus electric field demonstrate that, as the concentration of PT increases, the ferroelectric hysteresis loop of the PSZT-PT solid solution transforms from a narrow curve to a wide-open loop with enhanced remanent polarization and coercive field, confirming the relaxor to ferroelectric transformation. The domain structures of PSZT-PT were imaged and analyzed by means of TEM. The results show the presence of polar nano-domains in the relaxor composition, which transform into microscopic domains in the ferroelectric compound, revealing the transformation from the relaxor to ferroelectric state on the nano- to micro-scale. The mechanism of the crossover was illustrated from the effects of the substitution of ferroelectrically active lead titanate.

Finally, the evolutions of the crystal structures and physical properties of the PSZT - PT solid solution are presented in the forms of structural and dielectric phase diagrams, providing a clear picture of the crossover from relaxor to ferroelectric state in this pseudo-binary system, and the phase diagram of the $PbZrO_3$ - $PbTiO_3$ - $SrTiO_3$ ternary system is established.

Keywords: Relaxor ferroelectrics, Crossover, Ferroelectricity, Perovskite solid solution

This thesis is dedicated to my dear parents,

Thank you for your love and support.

Acknowledgements

First and foremost, I would like to express my deep gratitude and sincere appreciation to my senior supervisor, Dr. Zuo-Guang Ye, who provided me the opportunity to do this research. With his guidance, support and encouragement, I have learned a lot in academic skills and gained invaluable life experience during my master study.

I would also like to thank my supervisory committee members, Dr. Hua-Zhong Yu and Dr. Corina Andreoiu for their constructive suggestions and advice. I would like to further thank Dr. Krzysztof Starosta for being my internal examiner.

I am also grateful to all the members of Dr. Ye's research group, both previous and present, for their enormous support and valuable friendship, including Yi Yuan, Neha Claire, Vidhi Chauhan and Maryam Bari. I would like to give my special thanks to Dr. Bixia Wang for her mentorship to nurture my academic knowledge and corrections made to my thesis, and Dr. Alexei A. Bokov for his guidance.

I would like to express my gratitude to the staff of 4D LABS and Department of Chemistry for their financial and facility support.

Finally, I would like to thank my parents Qin Chen and Zhigan Dong for their support, encouragement and endless love.

Table of Contents

List of Tables

List of Figures

List of Acronyms

ε''	Imaginary part of permittivity
ε_r^*	Complex permittivity
C	Curie constant
d_{33}	Piezo-coefficient
E	Electric field
E_a	Activation energy
FE	Ferroelectric phase
G	Free energy
k_{33}	Electromechanical coupling factor
K_B	Boltzmann constant
K_p	Planar electromechanical coupling factor
MPB	Morphotropic phase boundary
n	Refractive index
P	Polarization
pC/N	Piezoelectric coefficient unit
PE	Paraelectric phase
PMN	$Pb(Mg_{1/3}Nb_{2/3})O_3$
PMN-PT	$(1-x)Pb(Mg_{1/3}Nb_{2/3})O_3$-$xPbTiO_3$
P_r	Remanent polarization
P_S	Spontaneous polarization
PSZT	$(Pb_{0.5}Sr_{0.5})(Zr_{0.5}Ti_{0.5})O_3$ or $(Pb_{1-x}Sr_x)(Zr_{1-x}Ti_x)O_3$
PSZT-PT	$(1-x)(Pb_{1-y}Sr_y)(Zr_{1-y}Ti_y)O_3$ - $xPbTiO_3$
PT	$PbTiO_3$
PZ	$PbZrO_3$
PZT	$Pb(Zr_{1-x}Ti_x)O_3$
R_{wp}	R-weighted-pattern, goodness of fit parameter for Rietveld
ST	$SrTiO_3$
t	Tolerance factor
T	Temperature

tan δ	Dielectric loss
T_B	Burns temperature
T_C	Curie temperature
T_{CW}	Curie-Weiss temperature
TEM	Transmission electron microscope
T_f	Freezing temperature
T_{max}	Temperature of maximum permittivity
V	Voltage
XRD	X-ray diffraction
ε'	Dielectric permittivity (dielectric constant)
θ	Bragg angle or angle of incidence
λ	Wavelength

Chapter 1.

Introduction

This thesis presents the investigation of novel lead-reduced ferroelectric and relaxor ferroelectric ceramic materials with the purpose of studying the crossover between relaxor and normal ferroelectric and having a comprehensive understanding of the electrical as well as the structural properties.

This chapter provides a general introduction of the basic concepts and background information, which includes the perovskite structure, piezoelectric properties, ferroelectric properties, relaxor ferroelectric properties, $PbZr_{1-x}Ti_xO_3$ solid solution, $SrTiO_3$ and quantum paraelectric.

1.1. Perovskite Structure

Perovskite material is one of the most studied functional materials because of its unique and outstanding electrical properties. The general formula of perovskite oxides is ABO_3, where A and B are cations and O is oxygen. As shown in Figure 1.1, six oxygens form an oxygen octahedron in a unit cell of the perovskite structure, and they are located at the face centers of the cube. A-site cations are located at the corners of the unit cell with a coordination number of 12, which is the total number of points of attachment to the cation, and a valence ranged from +1 to +3, which indicates the number of other atoms can combine with this atom. B-site cations occupy the center of the oxygen octahedral with a relative smaller size compared to that of A-site cations. The valence of B-site cations is from +4 to +6 with a coordination number of 6. In the non-polar unit cell, the dipole moment can be induced due to the off-center displacement of B-site cations.

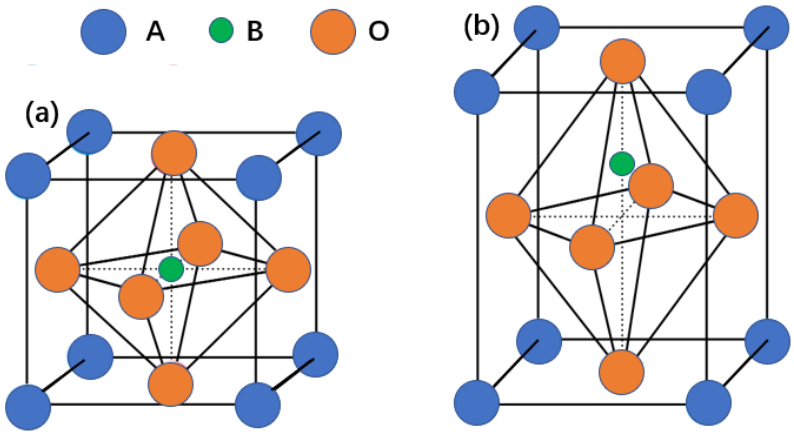

Figure 1.1 **ABO_3 perovskite structure with (a) cubic, non-polar unit cell, and (b) tetragonal, polar unit cell.**

In a perovskite structure, two or more ions are generally allowed to occupy crystallographic equivalent sites. Consequently, a complex structure with formulas like $(A_1A_2)BO_3$, $A(B_1B_2)O_3$, (A_1A_2) $(B_1B_2)O_3$, etc., can be formed. In various combinations of cations, the total valence of A and B cations must equal +6 to satisfy the charge balance with the -6 valence from oxygen anions.

The stability of perovskite structure can be predicted by the tolerance factor (t) (Eq. 1.1), which describes the deviation from an ideal cubic perovskite structure:

$$t = \frac{r_A + r_O}{\sqrt{2}\,(r_B + r_O)} \quad , \qquad \text{(Eq. 1.1)}$$

where r_A, r_B and r_O are the ionic radii of the cations at A and B sites and the oxygen anion, respectively. For an ideal cubic structure, the tolerance factor is 1. A perovskite unit cell can be considered theoretically stable when the value of t is between 0.88 and 1.09 [1]. The distortion in perovskite structure can be observed when the cations in the unit cell are too large or too small. In the previous studies of a low symmetry distortion, it is found that the tolerance factor is less than 1 for a rhombohedral or monoclinic structure, and greater than 1 for a tetragonal structure [2].

The perovskite structure provides an excellent frame, which can accept a variety of chemical modifications like ionic substitutions and non-stoichiometry, leading to a wide range of new or improved functional materials, including the piezoelectrics and ferroelectric materials that are central to this thesis work. On the other hand, the

complexity of the perovskite structure offers a unique venue to investigate the relationship between the crystal structures and physical properties of functional materials, which is also one of the main objectives of this work.

1.2. Piezoelectric Properties

Piezoelectric materials are applied in various fields such as engine, actuator, medical ultrasonic imaging, SONAR, etc [3]. The unique property of these materials is the effect of energy conversion between electrical form and mechanical form. Specifically, as a mechanical force is applied on piezoelectric materials, a voltage will be generated. This is defined as the direct piezoelectric effect and could be described by equation 1.2. The phenomenon of an internal strain induced by an applied electric field is known as the reverse (or converse) piezoelectric effect, which can be expressed by equation 1.3:

$$P_i = d_{ij} T_j, \qquad \text{(Eq. 1.2)}$$

$$S_j = d_{ji} E_{i,} \qquad \text{(Fq. 1.3)}$$

where P_i represents the induced electrical polarization, T_j is the mechanical stress applied on the material, E_j is the electric field applied, S_i is the induced strain and d_{ij} is the piezoelectric coefficient [4], [5]. The subscripts *i* and *j* represent the tensor notation of the physical properties of the materials. As shown in Figure 1.1, i can be 1,2,3 and j can be 1,2, …, 6. For the strain values, i = 1,2,3 represent the linear components, and j = 4,5,6 are the shear components [5]. The piezoelectric coefficient measured in the direction of applied electric field is known as the longitudinal coefficient (ij = 11, 22, 33), and that measured in the direction perpendicular to the electric field is the transverse coefficient (ij = 12, 23, 31). The remaining coefficients are shear coefficients (ij = 14, 15, 16,…34, 35, 36). (Figure 1.2)

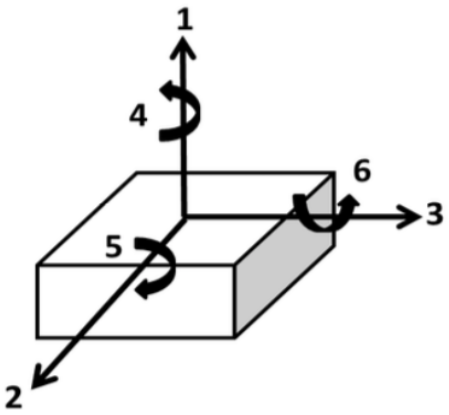

Figure 1.2 The tensor notation of j from 1 to 6

Electric coupling factor k specifies the efficiency of interconversion between electrical and mechanical energies, which can be defined by the following equations:

$$k^2 = \frac{mechanical\ energy\ stored}{electrical\ energy\ applied} \quad \text{or} \quad k^2 = \frac{electrical\ energy\ stored}{mechanical\ energy\ applied}$$

The *k*-factor carries different subscripts depending on different measuring modes. For instance, k_{33} is the coupling factor for longitudinal vibrations of rod-shaped piezoelectric materials, and k_p is the planar coupling factor for a thin disc in which the radial coupling is measured between the electric field applied in the direction of ceramic internal polarization and the mechanical vibrations produced along the radial directions.

1.3. Ferroelectric Properties

1.3.1. Ferroelectric Domains and Hysteresis Loop

Ferroelectric material is a subgroup of piezoelectric material. It has a spontaneous polarization that can be reoriented by an applied electric field. The spontaneous dipole in the ferroelectric material arises mainly from the displacement of B-site cation from the center of the unit cell. Without the external electric field, the spontaneous dipoles are randomly oriented. In some regions of ferroelectric materials, dipoles may be aligned in the same direction. Such regions with dipoles sharing the same orientation are called domains, and domain walls are the interfaces between these domains (Figure 1.3).

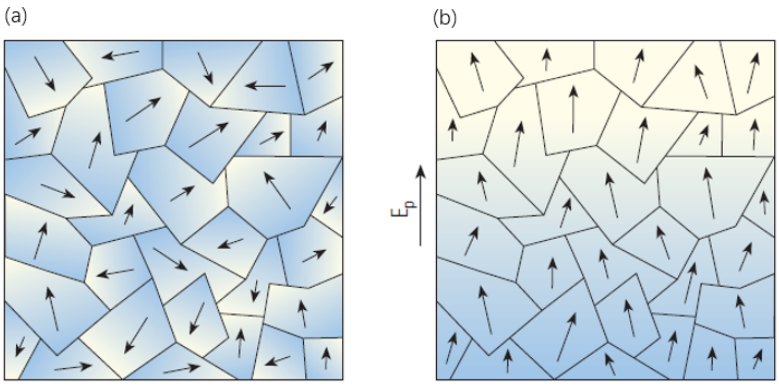

Figure 1.3 Domains in ferroelectric ceramics with (a) the spontaneous polarizations oriented randomly in the absence of an external electric field, and (b) polarizations aligned with the direction of an applied poling electric field E_p (adapted from Ref. [6]).

The reorientation of the dipoles in response to the electric field can be characterized as a hysteresis loop. As shown in Figure 1.4, the dipoles of domains are oriented randomly without electric field applied (Point A). As the electric field increases, the dipoles are gradually aligned with the direction of the field and the polarization increases linearly at initial stage (segment curve A towards $+P_s$ of the upper-right graph). The polarization reaches the saturation polarization ($+P_s$) under a sufficiently high electric field, where all dipoles in different domains are aligned with the direction of the electric field (theoretically). Thereafter, as the electric field is removed ($+P_s$ to $+P_r$ on the graph), the polarization decreases but does not become zero at E = 0, where a remanent polarization ($+P_r$) exists. Applying an electric field in the opposite direction will lead to a decrease in polarization ($+P_s$ to $-E_c$ on the upper-left graph), and the electric field that is needed to eliminate the remanent polarization is called the coercive field ($-E_c$). With further increase of the reversed electric field ($-E_c$ to $-P_s$ on the lower-left graph), the orientation of dipoles will become completely aligned with the direction of this field, and finally the saturation polarization ($-P_s$) in the opposite direction will be reached. Once the reversed electric field is removed ($-P_s$ to $-P_r$ on the graph), a remanent polarization ($-P_r$) in the opposite direction can be observed ($-P_r$). Applying a positive coercive electric field ($+E_c$) reduces the remanent polarization to zero, and the hysteresis loop is completed in this way ($-P_r$ to $+E_c$ on the graph).

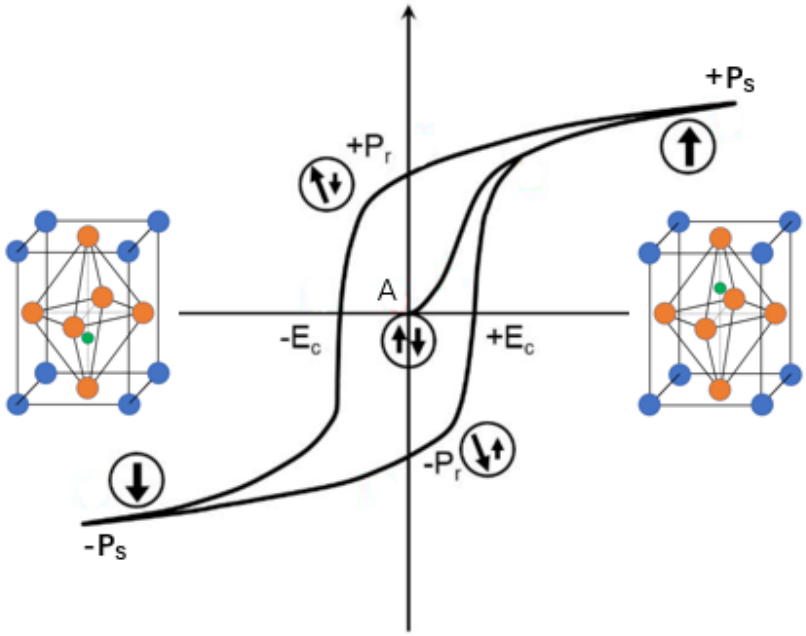

Figure 1.4 **A typical hysteresis loop of ferroelectric materials with arrows indicating domains under different electric fields. The corresponding dipole orientations and switchings are illustrated with the example of perovskite unit cells aside.**

1.3.2. Phase Transitions and Curie Temperature

Ferroelectric materials usually exhibit ferroelectric properties only when the temperature is below a phase transition temperature, which is called the Curie temperature (T_C). Above T_C, the materials show a paraelectric phase and have a non-polar and typically central symmetric structure. Below T_C, the materials are in the ferroelectric phase and have a non-central symmetric and polar structure, and the spontaneous polarization mainly occurs due to the displacement of B-site cations. The ferroelectricity arises from the distortion of the structure, and the symmetry of the ferroelectric phase is lower than the one in the paraelectric phase. Figure 1.5 (a) (b) (c) represent a relationship between the free energy and polarization. In Figure 1.5 (a), the material is in the ferroelectric phase with two potential wells, and each potential well has a local minimum, which is the stable state in free energy. By applying a negative electric field, the polarization state can be switched from $+P_s$ to $-P_s$, and vice versa. When the temperature approaches T_C, the energy barrier between the two potential wells reduces towards zero and the potential curve becomes flattened, as shown in Figure 1.5 (b). When

the temperature is above T_C, two potential wells merge into one, and there is only one stable state with a single local minimum on the potential graph, as shown in Figure 1.5(c).

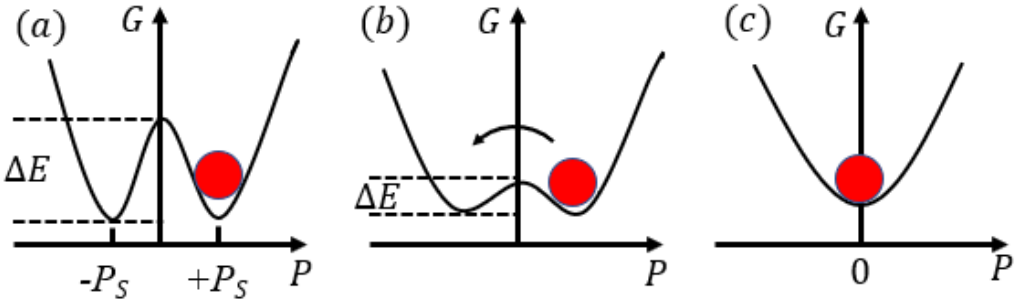

Figure 1.5 The two dimensional free energy diagram in terms of polarization (P) versus free energy (G) for a ferroelectric material, (a) below the Curie temperature (T_C), (b) around the T_C, and (c) above the T_C.

Figure 1.6 is an illustration of dielectric permittivity as a function of temperature for normal ferroelectric materials. Ferroelectrics show ferroelectric properties when temperature is lower than the Curie temperature T_C. As temperature approaches the ferroelectric to paraelectric phase transition temperature T_C, the dielectric permittivity increases and becomes maximum at T_C, which is called “dielectric anomaly” or dielectric peak. In addition to the dielectric peak, anomalies in other physical properties such as optical and thermal properties can be observed at this phase transition.

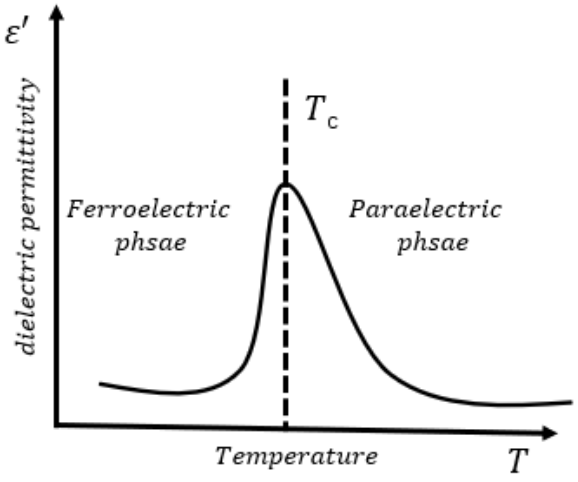

Figure 1.6 Variation of the dielectric permittivity as a function of temperature for normal ferroelectric materials. The sharp peak indicates the phase transition at the Curie temperature.

In the paraelectric phase of a ferroelectric material, the temperature dependence of dielectric constant follows the Curie Weiss law [4], as shown in equation.1.4:

$$\varepsilon' = \frac{C}{T - T_{cw}}, \qquad \text{(Eq. 1.4)}$$

where C is the curie constant, T is the absolute temperature in Kelvin, T_{CW} is the Curie-Weiss temperature and ε' is the dielectric permittivity.

1.4. Relaxor Ferroelectric Properties

Relaxor ferroelectric materials are a class of disordered crystals possessing peculiar structures and properties [4]. These materials are a subgroup of ferroelectric materials and have attracted extensive attention in the material science field. Due to their promising performance in dielectric properties, these materials are considered as good candidates for applications in novel memory devices and multi-layer energy storage capacitors, etc [6].

1.4.1. Characteristics of Relaxor Ferroelectric Materials

The common feature of relaxors is compositional disorder, which is the random arrangement of various ions among the crystallographically equivalent lattice sites [7]. The relaxor ferroelectrics form when at least two kinds of different ions occupy at A and/or B sites in perovskite structure ABO_3, including the stoichiometric complex compounds $A(B_1B_2)O_3$, e.g. $Pb(Mg_{1/3}Nb_{2/3})O_3$ [8], and the non-stoichiometric complex structure $(A_1A_2)(B_1B_2)O_3$, e.g., $Pb_x\ La_{1-x}(Zr_yTi_{1-y})_{1-x/4}O_3$ [9]. In more recent research on relaxor materials, many homovalent and complex perovskite solid solutions have been reported, such as $Ba(Zr_{1-x}Ti_x)O_3$ [10], and $(1-x)Pb(Mg_{1/3}Nb_{2/3})O_3$-$xPbTiO_3$ [11]. In these relaxor materials, the random distribution of cations leads to the compositional disorder, which then forms randomly oriented dipoles and local random fields. As a result, the long-range ferroelectric order is absent and short-range dipole orders are observed as nanoscale polar regions.

Relaxor ferroelectrics are different from normal ferroelectrics in many aspects. Firstly, relaxor materials show a broad and diffuse peak in the graph of dielectric constant (ε) versus temperature (T). An illustration of the temperature dependence of dielectric

permittivity of the canonical relaxor material $Pb(Mg_{1/3}Nb_{2/3})O_3$ is shown in Figure 1.7 [12]. Compared to the sharp dielectric peaks in normal ferroelectrics, a relatively broad peak of dielectric constant can be observed in relaxor ferroelectrics. In relaxor materials, as measurement frequency increases, the temperature of the maximum dielectric constant (T_{max}) increases and the value of maximum dielectric constant decreases, showing a characteristic frequency dispersion, as oppose to normal ferroelectrics that show frequency independent dielectric maxima.

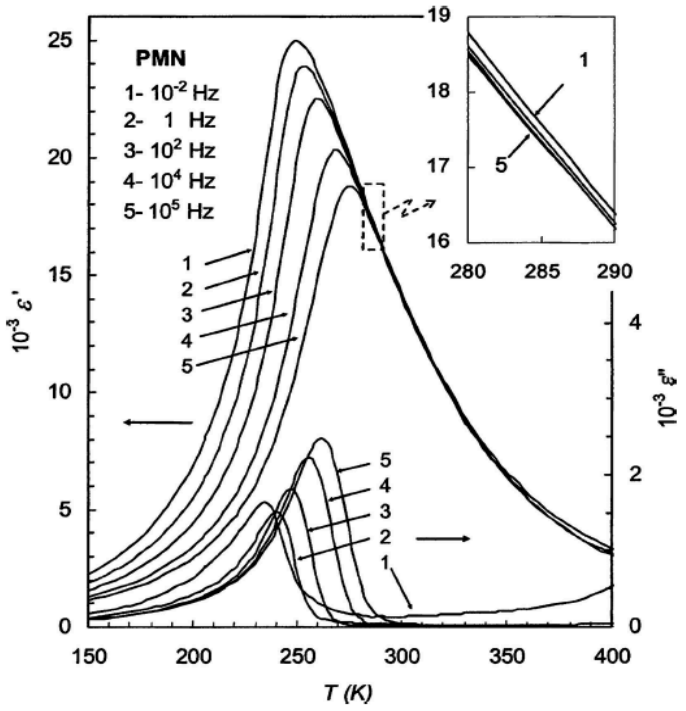

Figure 1.7 Temperature dependence of the relative permittivity at selected frequencies in a canonical relaxor ferroelectric $Pb(Mg_{1/3}Nb_{2/3})O_3$ single crystal (adapted from Ref. [13]).

Relaxor materials can also be characterized by the absence of any-macroscopic phase transition associated with the dielectric maximum. Different from normal ferroelectric, relaxors undergo the transition from paraelectric to ergodic relaxor phase without accompany of the macroscopic structural transformation [12]. Figure 1.8 demonstrates the different states (phases) and the phase transition temperatures in relaxor materials. At high temperature, relaxors exhibit a non-polar paraelectric phase. As temperature decreases, they transform into an ergodic relaxor phase at the Burns temperature (T_B), which is typically far above T_{max}. In this phase, the nanoscale polar

regions with randomly orientated and distributed dipole moments appear, and these polar nano regions (PNR) are considered to be responsible for the peculiar properties of relaxors. Upon cooling, the size of PNRs grows gradually and their dynamic fluctuation slows down, giving rise to the dielectric maxima around T_{max}. At a low enough temperature (T_f), which is typically hundreds degree below T_B, the PNRs become completely frozen and relaxor state will transform into a nonergodic phase. Because of non-macroscopic phase transition, the average symmetry of the crystal remains as cubic.

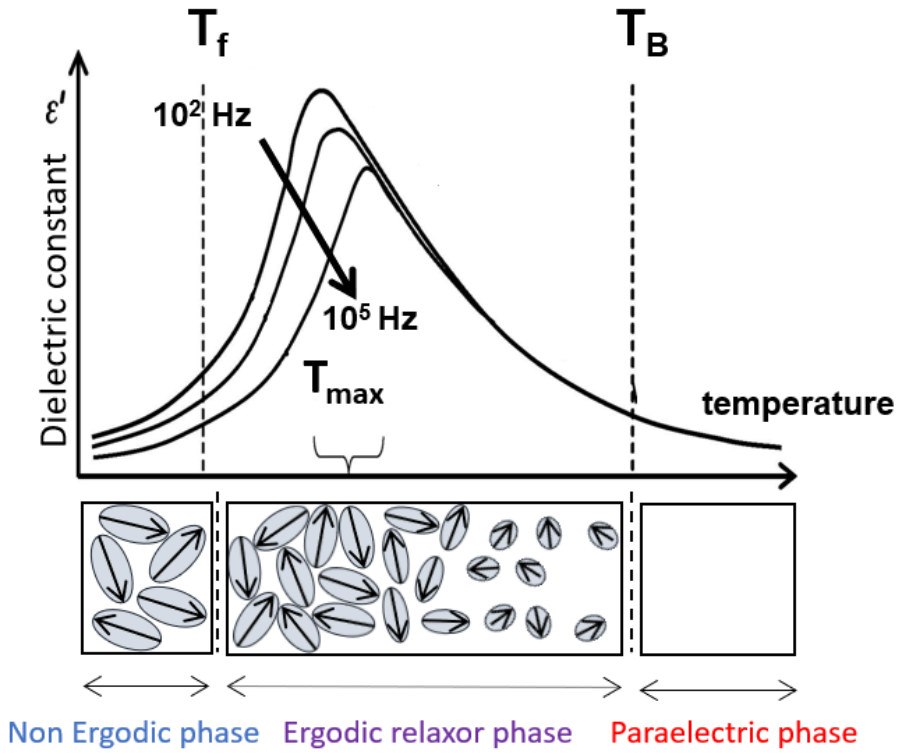

Figure 1.8 **An illustration of different phases at different temperatures in a canonical relaxor material like $Pb(Mg_{1/3}Nb_{2/3})O_3$ and the corresponding size of polar nano-regions (PNR), where arrows represent the total dipole moment in the corresponding nano domains.**

1.4.2. Polar Nano Regions (PNR)

Macroscopically, the ergodic relaxor phase possesses the same average structural symmetry as the paraelectric phase. However, in the nanoscale, relaxor materials contain regions of randomly oriented local polarizations, which are usually called polar nanoregions (PNRs) [13]. The fluctuation of orientation and magnitude of dipoles in PNRs gives rise to the peculiar properties in relaxor materials, such as characteristic

dielectric dispersion, high electrostriction, excellent dielectric performance, etc. The thermal dynamic change in PNRs can be observed as the relaxor material undergoes transition from the ergodic phase to the non-ergodic phase. As the temperature decreases below the freezing temperature, the temporal fluctuations of dipoles in PNRs vanish and the static local polarization can be observed [14].

Various models have been proposed to explain the PNR (or nano domains) in relaxor, and they can be subdivided into two categories. In the first category of models, PNRs are considered as a result of local “phase transitions” or phase fluctuations so that the crystal consists of nano-size islands embedded into a non-polar cubic matrix retaining from the paraelectric phase [15], [16]. The second category of models assumes that the phase transition occurs in all regions of crystals and the crystal consists of low-symmetric nanodomains separated by domain walls[17], [18].

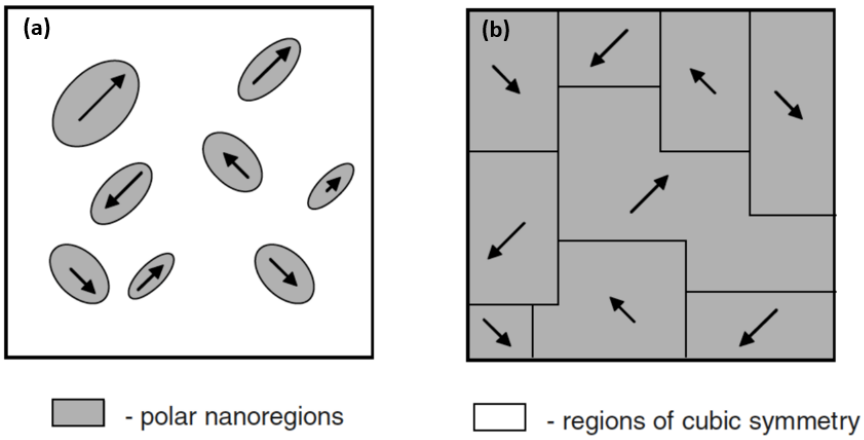

Figure 1.9 The schematic of polar nanoregions described in (a) the first model, and (b) the second model for relaxors, as described in the text (adapted from Ref. [13]).

In the early research by V. A. Isupov *et al*. [19], the model of the first category of PNR domains was developed and studied. It was proposed that chemical inhomogeneity caused by the disordered distribution of B-site cations will lead to the different local Curie temperatures. In this case, the T_{max} can be considered as the average Curie temperatures of different local regions. Because of the chemical disorder, the phase transition is spread out over a temperature range [19], [20]. However, in the later research, it was found that the diffuse phase transition is not related to the relaxation observed in relaxor materials [21]. The nature of interactions between PNRs was then studied by D. Viehland *et al.* [22].

In this work, the data of $90PbMg_{1/3}Nb_{2/3}O_3$-$10PbTiO_3$ (PMN-10PT) was applied in the model to determine if the data give evidence for a static freezing temperature. It was found that the relaxation in relaxor becomes extremely low as the temperature decreases below T_{max}, which is considered as the onset of relaxor freezing. The Vogel-Fulcher (VF) relation, which was used long ago to treat the relaxation in spin glasses [23]–[25] was firstly investigated in relaxor in Viehland's work. The VF relation is expressed as:

$$\tau = \tau_0 \exp[\frac{E_a}{k_B(T_{max} - T_f)}] \ , \qquad \text{(Eq. 1.5)}$$

where τ is the relaxation time for the reorientation of dielectric polarizations, τ_0 is the high-temperature limit of relaxation time, E_a is the activation energy, k_B is the Boltzmann constant, T_{max} indicates the temperature of the permittivity maximum, and T_f is the static freezing temperature, at which the relaxation time becomes infinite [26]–[28]. Thus, the relation is only applicable when T_{max} is larger than T_f. The activation energy is generally considered to be the product of mean cluster volume v and an anisotropy energy k_{anis}[29]. The electrocrystalline anisotropy energy represents the energy barrier for the rotation of the polarization between different orientations. Since the volume also determines the activation energy, the relatively small difference in the size of polar regions will lead to a large change in its fluctuation frequency [22]. In the works of L. E. Cross [30], a superparaelectric model was suggested to explain the activation energy of PNR domains. The activation energy barrier between equivalent states is directly proportional to the size of the nano polar regions. As temperature decreases, the thermal fluctuation of the polarization slows down, which results in the freezing of dipoles caused by the cooperative interactions between adjacent diploe moments.

The VF relation can be converted into the version shown below (Eq. 1.6) to better describe the relaxor behaviour:

$$f = f_0 \exp[-\frac{E_a}{k_B(T_{max} - T_f)}] \, , \qquad \text{(Eq. 1.6)}$$

where f_0 is the Debye frequency. The second category was developed and studied by Westphal *et al.* [17] and Kleemann [31]. They believed in the existence of strong random field, which causes the dielectric response of PMN. Kleemann [31] supposed that the 'superparaelectric' model was investigated without the connection with a random field, but

rather considered as the constituents of some types of cluster glass. In their opinions, both types of interactions, random bonds and random fields should be taken into account together with compositional and space charge fluctuations in a disordered relaxor system [31]. It was proposed that the quenched random fields are at the origin of the observed tremendous slowing down of the dipole dynamics of PMN, which eventually freezes into a nanoscale polar domains. The second order phase transition is not observed because the random fields conjugate to order parameter. Below the Curie temperature, the long-range ordered ferroelectric state breaks into tremendous nanoscale domains. The intense sources of random fields are inherent in the disordered solid solution with random distribution of Mg^{2+} and Nb^{5+} cations. The compositional fluctuations that create space charges and electric field fluctuations are on atomic length scales. In the TEM analysis by E. Husson *et al.* [32], quenched compositional fluctuations extending over 3 nm with one-by-one ordering of Mg^{2+} and Nb^{5+} cations were observed. These compositional fluctuations establish the negatively charged domains. In general, the second model of PNRs describes the domains by considering the significance of random fields, various types of interactions, chemical texture and compositional fluctuations [33].

The two categories of PNR models have the common point in them: chemical inhomogeneity leads to the local structure distortion and gives rise to the nano-size polar clusters and PNR, which can be observed as short-range ordered regions embedded in the disordered matrix. For example, in $Pb(B'_{1/2}B''_{1/2})\ O_3$ perovskites, the ordering of B-site cations causes structural symmetry to change from a disordered Pm-3m structure to an ordered Fm-3m structure. In the ordered symmetry, the B' cations alternate with B" cations along the <110> direction with 1:2 ordering [12]. A charge-balanced "random-site" model was proposed to explain the distribution of ordered and disordered matrixes. As shown in Figure 1.10, one of the B-sublattices is occupied exclusively by B^{5+} ions, and the B^{5+} or B^{2+} locates randomly in the other B-sublattices in a 2:1 ratio so that the local stoichiometry is preserved [34]. The degree of compositional disorder can greatly influence the ferroelectric and relaxor properties. For example, the disordered $Pb(In_{1/3}Nb_{2/3})O3$ (PIN) crystals are relaxor ferroelectrics, but in the ordered state, they are antiferroelectrics with a sharp phase transition [21], [35] confirming the general rule that the relaxor behaviour can only be observed in disordered crystals.

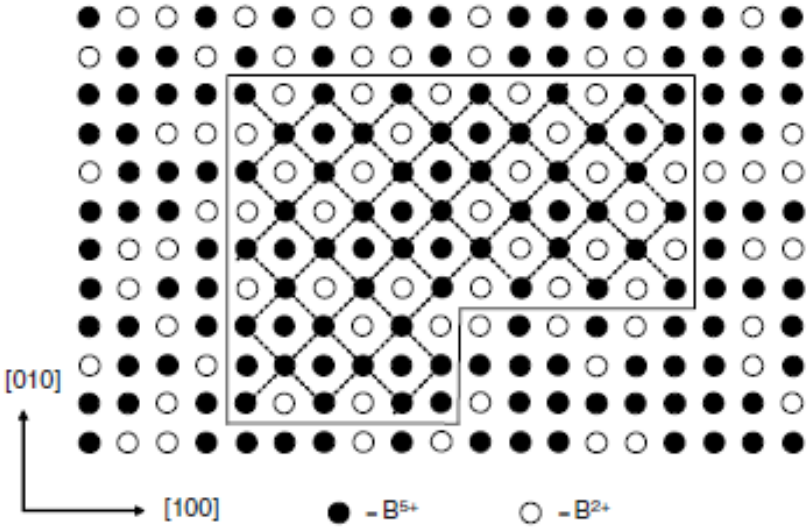

Figure 1.10 **A schematic drawing of the ordered chemical nanoregion CNRs (the area delimited by the solid line) embedded in the disordered matrix in $Pb(B^{2+}_{1/3}B^{5+}_{2/3})O_3$ perovskites according to the random-site model. One of the two sublattices inside CNR (shown by dashed lines) is formed by B^{5+} ions only (adapted from Ref. [13]).**

1.5. The $PbZr_{1-x}Ti_xO_3$ solid solution

A solid solution is the continuous sequence of substances with compositions intermediate between two distinct solid phases, called end members [1]. Components can be designed to substitute for one another on the atomic level in the solid solution series. From one end member to another, the intermediate members show structures and properties that vary continuously as composition changes. For example, the solid solution of $PbTiO_3$ and $PbZrO_3$ can be prepared and synthesized by following the reaction:

$$(1- x)PbZrO_3 + xPbTiO_3 \longrightarrow Pb(Zr_{1-x}Ti_x)O_3$$

At room temperature, $PbTiO_3$ exhibits a ferroelectric phase with a tetragonal crystal structure and $PbZrO_3$ is an antiferroelectric phase with an orthorhombic structure. As the result of substitution of B-site cation Ti^{4+} for Zr^{4+}, a binary solid solution of $Pb(Zr_{1-x}Ti_x)O_3$ (PZT) forms. The Curie temperature of PZT varies from 220 °C to 490 °C as composition changes. For compositions with lead titanate (PT) content below 10%, the PZT is antiferroelectric with an orthorhombic structure below T_C. And all the solid solutions containing more than 10 % PT concentration are ferroelectric at room temperature. When

the temperature is above T_C, a paraelectric phase with a cubic structure can be observed for all the compositions.

One of the characteristics that make this system special is that the low temperature phase diagram (Figure.1.11 [36]) is divided vertically into two parts of different crystal symmetry: rhombohedral for the Zr-rich side and tetragonal for the Ti-rich side. The boundary between the two phases is called morphotropic phase boundary (MPB), which was first proposed by Jaffe et al. [37] For compositions close to the MPB region, the useful properties such as electromechanical coupling factor (k_{33}), piezoelectric coefficient (d_{33}), remanent polarization (P_r) and dielectric permittivity (ε′) all reach their maximum values, respectively. The highest piezoelectric response (~ 350 pC/N) was found for the MPB composition with x = 0.47 in this system [38].

PZT ceramics have been widely used in electronic and transduction industries for decades. However, the microstructures of PZT materials and the atomistic phenomena are still under debate. So far, several theories have been proposed to explain the intricate structures and behaviours of PZT solid solution. Historically, Cao *et al.* [39] believed that the coexistence of tetragonal and rhombohedral phases near the MPB region leads to the increase of dielectric permittivity. There are six equivalent polarization directions in the tetragonal structure and eight in rhombohedral structure [39]. It was argued that because of the two polymorphs, there are fourteen equivalent polarization directions in total, which allows materials to be polarized into fourteen possible directions under the influence of an external electric field [39].

In 1999, Noheda *et al.* found, by means of synchrotron X-ray diffraction, the presence of a monoclinic phase near the MPB region in the PZT system, which can be considered as the bridge between the tetragonal phase of lead titanate-rich side and the rhombohedral phase of lead zirconate-rich side [40]. The introduction of the monoclinic phase also provides more possible directions of polarizations. Later, several researches investigated the models involving coexistence of various structures such as monoclinic, rhombohedral and tetragonal phases [41]–[43]. Jin *et al.* [44] found that a nanoscale coherent mixture of microdomains can be interpreted as an adaptive ferroelectric phase, whose microdomain-averaged crystal lattice is monoclinic [44]. This model was then studied by Wang *et al.* by considering the nano-twin super lattices in the microstructure of PZT [45]. There are two possible monoclinic phases existing in the MPB region, which can

be denoted as M_A and M_B phases. The difference between these two phases is the cation displacements. The M_A phase has cation displacements between the rhombohedral and tetragonal positions, whereas the M_B phase is between rhombohedral and orthorhombic positions [46].

The phases near MPB region was further studied by pair distribution function analysis (PDF) based on the total synchrotron scattering data in the work of Zhang *et al.* [36]. The study reveals that long-range average rhombohedral and both long- and short-range monoclinic regions coexist at all compositions. As shown in Figure 1.11, a boundary between the monoclinic (M_A) structure and another monoclinic (M_B) structure has been found and marked as a dashed line in the graph. In addition, a minimized domain structure was found in the transmission electron microscopy study of Schönau *et al.* [43]. Instead of normal micro-sized domain, the minimized domain exists in the MPB regions and facilitates the reorientation of domains, which results in the enhanced piezoelectric properties. More investigations need to be carried out to reveal the nature of phase transition near MPB region and overall compositions.

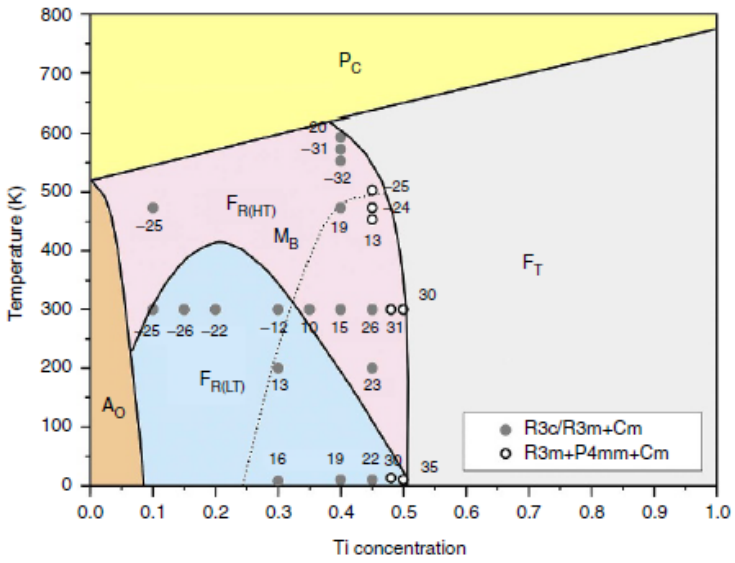

Figure 1.11 The phase diagram of PZT. The dashed line indicates the crossover between M_B and M_A structures. The marked phase regions are cubic P_C, orthorhombic A_O, the ferroelectric phases tetragonal F_T, rhombohedral $F_{R(LT)}$ and rhombohedral $F_{R\ (HT)}$, using the notation of Jaffe *et al*. (adapted from Ref. [36]).

1.6. Modifications to PZT Ceramics

To meet the requirements for practical applications, PZT ceramics can be modified by substitutions of various ions to enhance or optimize the properties. Binary, ternary or quaternary systems have been prepared by doping different ions into PZT, such as La^{3+}, K^{+}, Na^{+}, Nb^{5+}, Fe^{3+}, etc. When a donor cation substitutes for the ions in PZT, this type of modified PZT is called “soft” PZT [47]. Cation vacancies will be created and local stress in the lattice will decrease, which facilitates the motion of domain walls [1], making the material "softened". For example, Nb^{5+} can be used for the replacement of Ti^{4+} and/or Zr^{4+}, and La^{3+} can be applied for the replacement of Pb^{2+}. In these cases, the motion of domain walls will be enhanced, which results in modified properties such as low coercive field (E_c), high dielectric loss (tan δ), large permittivity, high electromechanical coupling factor (k_p) and high piezoelectric coefficients. Acceptor ions create oxygen vacancies, which form defect dipoles. For example, Fe^{3+} can be used to replace Ti^{4+} and/or Zr^{4+}, and K^{+} and Na^{+} can be applied to substitute Pb^{2+}. When an electric field is applied in the poling process, the induced defect dipoles can be aligned in accordance with domain structure [48]. Thus, the domain structure can be stabilized or "hardened", which leads to high coercive field, low piezoelectric coefficients, low dielectric constant and low dielectric loss. This type of modified PZT materials is called “hard” PZT [49].

PZT system can also be combined with other perovskite complex systems such as $Pb(Mg_{1/3}Nb_{2/3})O_3$ or $Pb(Zn_{1/3}Nb_{2/3})O_3$. Because two or more types of cations occupy B-site cations, relaxor behaviour is observed in these complex systems [14], [50]. The addition of these systems to PZT brings desired features such as smaller grain size, higher density and lower sintering temperature. Many lead-free materials are also applied to the modification of PZT and to reduce the lead content. For example, the PZT - $AgSbO_3$ solid solution is a lead reduced system with a decent dielectric constant ($\varepsilon' > 2000$) and a large electromechanical coupling factor ($k_p > 75\%$) [51].

1.7. $SrTiO_3$ - An Incipient Ferroelectric & Quantum Paraelectric Material

Strontium titanate ($SrTiO_3$) is a typical perovskite compound. At room temperature, $SrTiO_3$ is in a paraelectric phase and has a cubic perovskite structure with a lattice parameter of 3.905Å and the space group of *Pm*-3*m* [52]. Only at very low temperature,

strontium titanate exhibits piezoelectric characteristics [53]. The dielectric constant of $SrTiO_3$ is 300 at room temperature, and it increases significantly upon cooling below 20 K [54] (Figure 1.12).

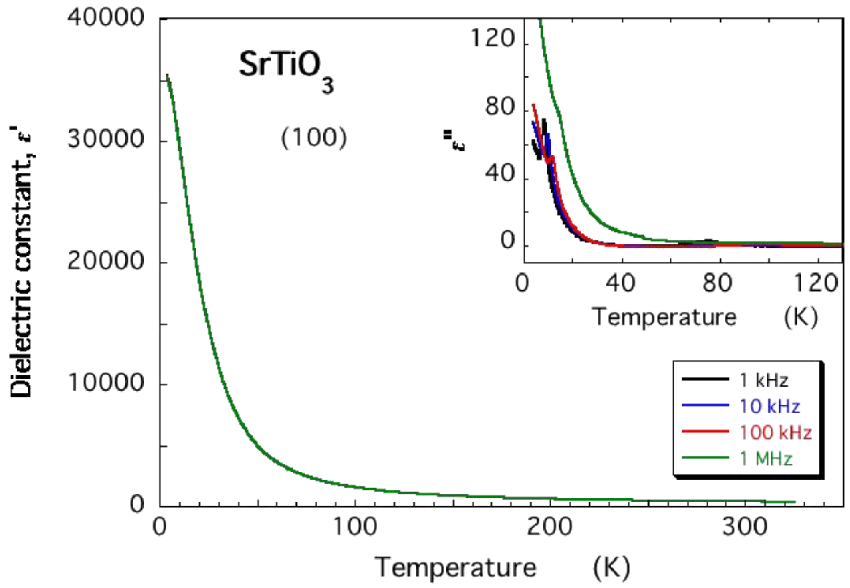

Figure 1.12 Dielectric constant of $SrTiO_3$ as a function of temperature measured at different frequencies (adapted from Ref. [55]).

$SrTiO_3$ belongs to a restricted family of dielectric materials, called quantum paraelectrics. A handful of other quantum paraelectric materials with perovskite structure include $EuTiO_3$ and $CaTiO_3$. The quantum paraelectrics are also called incipient ferroelectrics due to their ferroelectric instability [55]. Different from normal ferroelectric materials, the ferroelectricity in strontium titanate is suppressed by quantum fluctuations and it shows a paraelectric phase from high temperatures down to very low temperatures, preventing ferroelectricity from developing [56]. Quantum fluctuation is sensitive to ionic mass and it usually exists in materials with light atoms/ions, and it has important effect on structural and thermodynamic properties of materials [57]. However, as an exception, strong quantum fluctuation effect can be observed in $SrTiO_3$ even though it has relatively heavy atoms [57]. The quantum fluctuation can be prescribed and understood from fundamental Heisenberg uncertainty principle (Eq. 1.7), and in the ferroelectric system or quantum paraelectric system, the fluctuation refers to fluctuation of the ionic displacement:

$$\Delta p * \Delta q \geq \hbar/2, \qquad \text{(Eq. 1.7)}$$

where Δq is the uncertainty of atomic position (ionic displacement), which can be described as structural difference between different phases. Δp is the uncertainty of momentum, and $\hbar$ is the Plank constant. Considering the energy of the system, the corresponding uncertainty principle can be expressed as the formula below (Eq. 1.8):

$$\Delta E \geq \hbar^2/(8m\Delta q^2), \qquad \text{(Eq. 1.8)}$$

where ΔE is the zero-point energy that prevents the distorted phases in the system. In some quantum paraelectric materials, the structural and energetic differences between phases are very small [56]. As a result, the non-zero fluctuation of the ionic displacement associated with the zero-point oscillation, which acts as a quantum-mechanical displacive limit (S_{min}), may be high enough to suppress the distorted phases. As a consequence, the phase transition temperature (T_C) becomes zero (Figure 1.13) [58]. Above S_{min}, the sample approaches the classic ferroelectric behaviour. For the region below S_{min}, no phase transition can be observed. In this case, the zero-point energy-induced quantum suppression may take place even though massive ions exist in the quantum paraelectric materials.

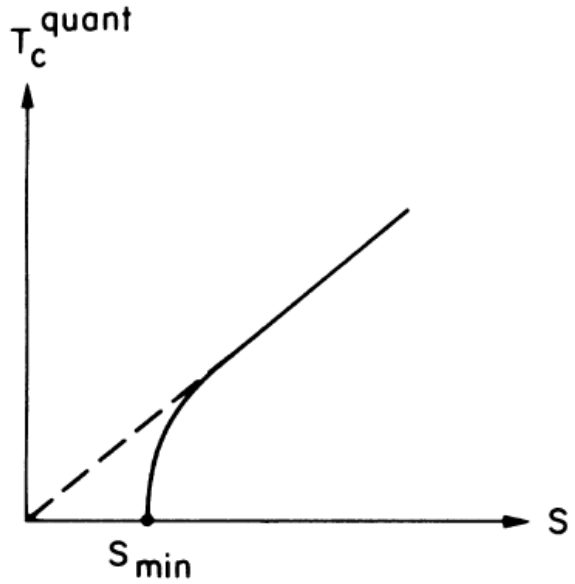

Figure 1.13 The correlation between quantum-mechanical transition temperature (T_C^{quant}) and the quantity of local displacement fluctuations (S) originates from the zero-point oscillations. S_{min} denotes the quantum-mechanical displacive limit where the transition temperature vanishes. (adapted from Ref. [59]).

As temperature decreases, $SrTiO_3$ undergoes an antiferrodistortive transition from cubic *Pm*-3*m* to tetragonal *P*4*mm* at 105 K due to the rotation of the TiO_6 octahedra. The softening of the polar phonons can be observed with the decrease of temperature, which indicates the trend of the formation of polar state. However, the softening of phonons saturates at a certain level instead of freezing to zero at low temperature. As a result, no ferroelectric phase transition takes place in $SrTiO_3$. The ferroelectric phase was suggested to be suppressed by strong quantum fluctuations in the $SrTiO_3$ system, giving rise to quantum paraelectric state [59].

1.8. Objectives and Organization of the Thesis

Since 1970s, PZT-based materials have become the most extensively used electro-ceramic materials in a wide range of industrial and technological applications, with a global market value of $12.3 billion in 2014 and an annual growth rate of 13.2% per year [60]. Over the last two decades, relaxor-based piezo-/ferroelectric materials have attracted great attention owing to their excellent performance of piezoelectric properties. Solid solution of $(1-x)Pb(Mg_{1/3}Nb_{2/3})O_3$-$xPbTiO_3$ (PMN-PT) is one of the representatives of these relaxor-based materials, and it is potentially useful for high-end electromechanical transducer applications from ultrasound imaging to adaptive optics and energy harvesting [61], [62]. However, some inherent drawbacks still exist in these relaxor based systems. For example, their low coercive field (E_c) and Curie temperature (T_C) make them unsuitable for applications under high electric field or at high temperatures. In addition, the high content of lead in these systems have raised much environmental and health concerns.

In order to explore new high performance ferroelectric materials to replace PZT and PMN-PT, a broad field of research on relaxor-ferroelectrics has been opened up. To overcome the limitations of the PZT and PMN-PT systems, a great deal of research has been focused on the design of new solid solutions particularly. However, on a widespread industrial scale, there are still no lead-free ferroelectric materials in production that have better versatility and performance than the lead-based materials [63]. Furthermore, the mechanism of relaxor behaviour is still poorly understood, and the relationship between PNR domains and relaxor ferroelectric properties of these systems remains to be established. Thus, the investigation of the transformation from relaxor to normal ferroelectrics can help us understand the differences between them, and provide us a path

to study the mechanism behind relaxor ferroelectric behaviours. Meanwhile, useful systems of lead-reduced ferroelectric materials will be designed and synthesized, which will provide us with more options of relaxor-based functional materials.

In this research, we investigate a novel ternary multifunctional solid solution system, which consists of quantum paraelectric strontium titanate ($SrTiO_3$), antiferroelectric lead zirconate ($PbZrO_3$) and ferroelectric lead titanate ($PbTiO_3$). In particular, we explore the pseudo-binary system of $(1-x)(Pb_{1-y}Sr_y)(Zr_{1-y}Ti_y)O_3$ - $xPbTiO_3$ (PSZT-PT) to study the effects of the substitution of PT for the $SrTiO_3$-modified PZT (PSZT).

As mentioned in Sec. 1.7, strontium titanate is a quantum paraelectric and incipient ferroelectric material. At room temperature, strontium titanate has a perovskite cubic structure. As temperature decreases, strontium titanate undergoes an anti-ferrodistortive transition from cubic to tetragonal phase at 105 K. However, this structural transition is not accompanied with a ferroelectric phase transition. At very low temperatures, the ferroelectricity is suppressed by quantum fluctuation, and strontium titanate remains in the paraelectric phase.

On the other hand, lead titanate is a typical ferroelectric material with a tetragonal perovskite structure at room temperature. It has the lattice parameters of a = 3.894 Å and c = 4.140 Å , and a tetragonality (c/a ratio) of around 1.063 [64]. Lead titanate undergoes a structural transition from the tetragonal to a cubic at the Curie temperature of 490°C [65]. Thanks to its high Curie temperature, lead titanate is a promising material for high-temperature applications. However, it is difficult to prepare high-quality pure lead titanate, because the high crystalline anisotropy (c/a ratio greater than 1.063) induces many internal stresses at the cubic-tetragonal transition and the lead titanate ceramic samples become fragile upon cooling through the Curie point [66], [67]. To improve the density and quality of lead titanate, isovalent ions, such as Ca^{2+}, Ba^{2+}, Sr^{2+}, or aliovalent ions, such as Sm^{3+}, Gd^{7+} and La^{3+} are used to substituted for the Pb^{2+} ions to reduce the lattice anisotropy, making it possible to produce dense and hard ceramics with a high-mechanical strength [68]. Furthermore, it was reported that the addition of these ions lowers the sintering temperature and consequently suppresses Pb volatilization, enhancing both mechanical strength dielectric and electrical properties of PZT ceramics [66], [69]–[71].

Lead zirconate is a typical antiferroelectric material and it has a phase transition in the vicinity of T_C = 230 °C [72]. It adopts an orthorhombic structure at room temperature with the *Pbam* symmetry [73]. The antiferroelectricity in lead zirconate originates from the antiparallel displacements of Pb^{2+} cations when the temperature is below the Curie temperature [72], [74]. Results of the XRD refinement revealed that the Pb^{2+} ions are displaced towards the $\{110\}_{pc}$ plane [75]. When an electric field is applied, the direction of the displacement of lead ions will be aligned with the direction of the electric field, and a structural transition from the antiferroelectric orthorhombic to a ferroelectric (rhombohedral) phase is induced, leading to double hysteresis loops in the polarization - electric field relation.

The novel ternary system studied in this work can be represented in the ternary phase diagram shown in Fig. 1.14, in which three end members are set as the three points of the equilateral triangle, and the bottom line of the triangle represents the solid solution compositions of the well-known binary PZT system. However, inside the triangle phase diagram, the phases, structures, phase boundaries and properties, as well their variations with composition are not yet known, and remain to be studied. Of particular interest is the solid solution with composition at the middle between $SrTiO_3$ and $PbZrO_3$, $(Pb_{0.5}Sr_{0.5})(Zr_{0.5}Ti_{0.5})O_3$ (PSZT), which exhibits typical relaxor ferroelectric properties. In the PSZT perovskite structure, both the Sr^{2+} and Pb^{2+} cations occupy the crystallographic equivalent A-sites, which leads to the compositional disorder in the system. As discussed before, chemical inhomogeneity can cause the local structure distortion, leading to the relaxor behaviour. Starting from this composition, the whole series of pseudo-binary solid solution, $(1\text{-}x)(Pb_{0.5}Sr_{0.5})(Zr_{0.5}Ti_{0.5})O_3\text{-}xPbTiO_3$ (PSZT-PT), presented as the blue line passing through the center of the diagram, will be synthesized and characterized. The pseudo binary system, PSZT-PT, has two end members, $(Pb_{1-y}Sr_y)(Zr_{1-y}Ti_y)O_3$ (PSZT) and $PbTiO_3$ (PT). PSZT exhibits relaxor behaviour [76] and PT is a typical ferroelectric material [77]. With the existence of both relaxor and normal ferroelectric phases in this system, the transformation from relaxor phase to normal ferroelectric phase can be studied and analyzed. Furthermore, the addition of strontium into lead-based system will reduce the content of lead, making the new pseudo-binary system more environmentally friendly than PZT. Also, by substituting Sr^{2+} for Pb^{2+} on the A-sites, the structural anisotropy can be reduced and it is possible to produce dense ceramics with high PT contents with better quality. In addition, it is interesting to study the effects of the substitution of strontium

titanate as a quantum paraelectric material on the structures and properties of the PZT binary system. In general, the implementation of this research will allow us to establish the $SrTiO_3$-$PbTiO_3$-$PbZrO_3$ phase diagram, uncover the crossover between relaxor and ferroelectric phases and related structures and properties, and explore a new lead-reduced relaxor ferroelectric system.

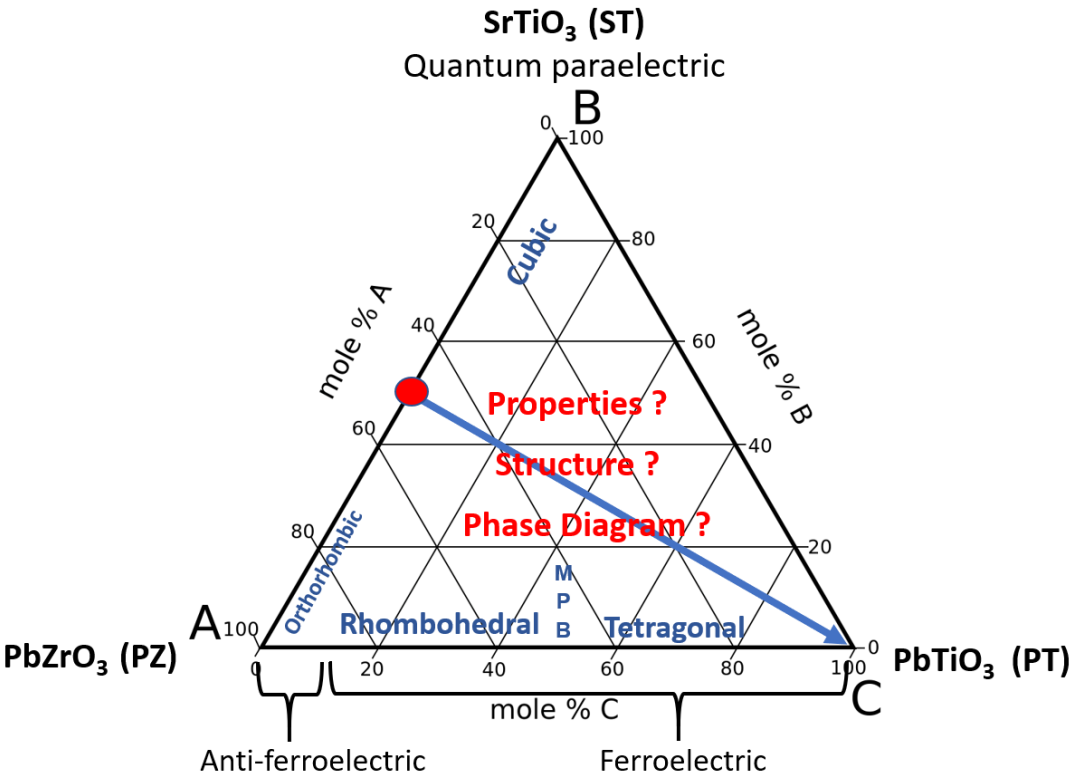

Figure 1.14 Ternary phase diagram of the ST-PZ-PT system, which defines the framework and objectives of the present research.

In this research, the ferroelectric properties and crystal structures of the (1-x)($Pb_{0.5}Sr_{0.5}$)($Zr_{0.5}Ti_{0.5}$)O_3-x$PbTiO_3$ (PSZT-PT) will be characterized, and the phase areas in the phase diagram will be delimited. To systematically study the crossover between the relaxor phase and ferroelectric phase, a series of structural refinements and characterizations will be carried out to analyze the crystal symmetry, dielectric and ferroelectric properties, phase transitions and local domain structures. These research concepts and approaches are illustrated in Figure 1.15.

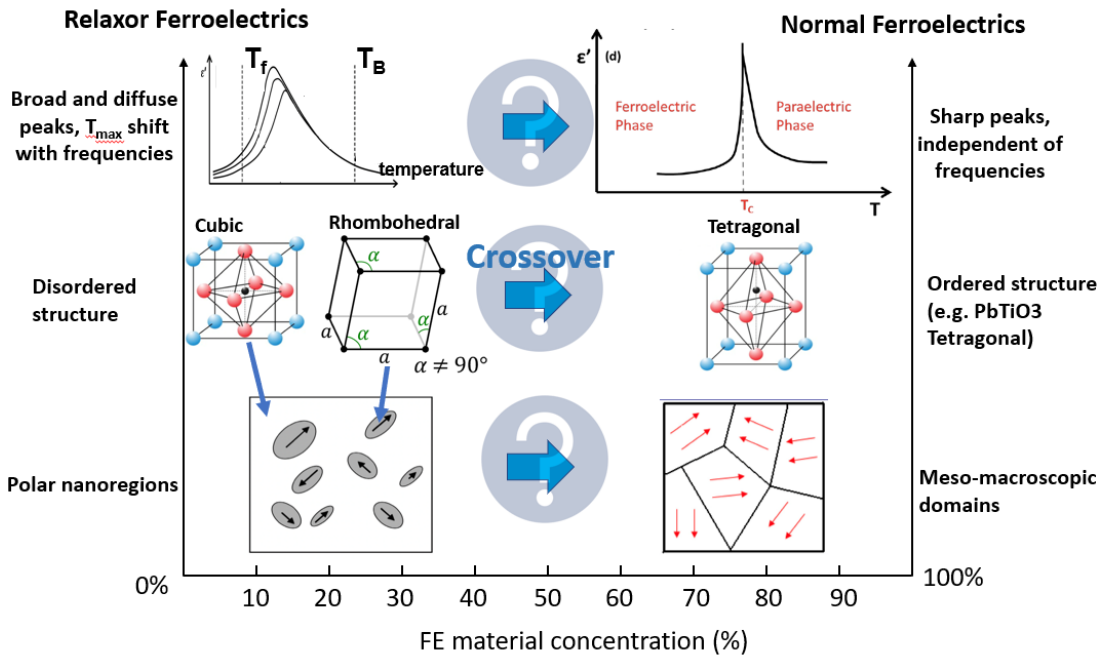

Figure 1.15 Proposed studies of the crossovers of electrical properties, crystal structures and microdomains in the (1-x)($Pb_{0.5}Sr_{0.5}$)($Zr_{0.5}Ti_{0.5}$)O_3-x$PbTiO_3$ (PSZT-PT) pseudo-binary solid solution.

Therefore, the objectives of this research are defined as follows: (1) Synthesis of the new (1-x)($Pb_{0.5}Sr_{0.5}$)($Zr_{0.5}Ti_{0.5}$)O_3-x$PbTiO_3$ solid solutions with various compositions in the form of ceramics by solid state reaction and sintering method; (2) Characterization of the structural symmetry, dielectric and ferroelectric properties and domain structure of PSZT-PT; (3) Investigation of the evolution of the structure, phase transition, relaxor to ferroelectric properties and domain structure of the PSZT-PT system; and (4) Establishment of the phase diagram of the PSZT-PT system in terms of phase symmetry and properties, and understanding of the structure-property relations and the effects of quantum paraelectric $SrTiO_3$ substitution for the PZT system.

This thesis is organized into the following chapters. Following the general introduction of this chapter, the principles of the main experimental techniques used in this work will be described in **Chapter 2**, such as, X-ray powder diffraction (XRD), dielectric spectroscopy, ferroelectric hysteresis loop measurement and transmission electron microscopy (TEM).

In **Chapter 3**, the synthesis of the (1-x)($Pb_{0.5}Sr_{0.5}$)($Zr_{0.5}Ti_{0.5}$)O_3-x$PbTiO_3$ (PSZT-PT)

solid solution with compositions of x from 0.05 to 0.95 will be presented in detail. Structural analysis of PSZT-PT is carried out based on X-ray diffraction data, which helps us to investigate the structural transformation as a function of different compositions. Detailed refinements are performed to determine the critical transition point between two end phases, the composition region of mixed phases and the fraction of phases.

Chapter 4 is focused on the investigation of the crossover of physical properties by characterizations of dielectric and ferroelectric properties of PSZT-PT. By measuring the dielectric properties of each composition using Novocontrol dielectric spectroscopy, the important characteristic temperatures and permittivity (T_{max}, ΔT_{max}, ε') will be obtained and the crossover of dielectric properties will be revealed. Fitting the dielectric data with theoretical models will help us to identify the presence of the relaxor phase and its composition range. The relationship between the structural phase transition and the dielectric properties will be discussed, which is key to the subsequent study of the ferroelectric properties in the solid solution. In the investigation of the ferroelectric properties, characterization of hysteresis loops with compositions shows the trend of transition between phases. The following section gives the results of the study of domain structures of PSZT-PT by means of transmission electron microscopy (TEM). In the study of domain morphology and sizes of the ion-milled samples, nano-meter domains are found in the relaxor compositions, which transform into macroscopic domains in the ferroelectric phase, revealing the crossover from the nano-sized domains to macro-domains as the concentration of PT increases across the critical region.

In **Chapter 5 [Phase Diagram, General Conclusions and Future Directions],** the study of the crossover will be summarized as conclusions and a reasonable phase diagram will be proposed. The proposed phase diagram will reveal the structural and phase transition, the trends of T_C and T_{max} variations and the regions contain mixture of different phases. The discussion of the proposed phase diagram is followed by the summary of this research work. Finally, future directions for this research project are suggested.

Chapter 2.

Materials Characterization: Principles and Techniques

2.1. Introduction

This chapter presents the basic principles and various experimental techniques, which are used to characterize the properties and crystal structure of piezo/ferroelectric materials prepared in this work. The chapter includes X-ray diffraction (XRD), dielectric spectroscopy, ferroelectric hysteresis measurement and transmission electron microscopy (TEM).

2.2. X-ray Diffraction

X-ray diffraction is a powerful technique that is widely used in the structural characterization of crystalline materials. This technique can provide information on crystal structure, phase symmetry and lattice parameters of materials. X-ray is generated in an X-ray tube, in which there is a heated filament (cathode) that can produce a source of free electrons [78]. These electrons are then accelerated by a high electric potential and subsequently strike the target material (anode). When the electrons on the K shell of the target atom are ejected by the electron beam, the electrons on the high energy level will drop to low energy level to occupy the vacancies (Figure. 2.1). The transition of electrons from higher to lower energy orbitals releases energy in form of X-ray radiation. Specifically, electrons descending from the L shell give K_α lines and electrons from M shell give the K_β lines. The wavelength of the X-ray radiation depends on the selected metal target, e.g. copper and molybdenum. In this work, the instruments we used are Rigaku MSC Diffractometer and Bruker D8 Advanced Diffractometer. In both cases, copper is used as the metal target and the corresponding wavelength of K_α radiation is 1.5418Å. In measurements of X-ray diffraction, the monochromatic radiation with single wavelength is normally required. Usually the K_α lines are selected and the K_β lines are filtered out by a thin nickel foil [78].

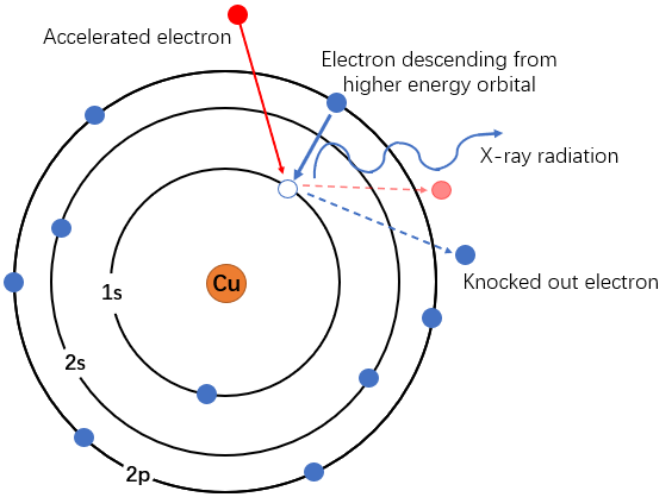

Figure 2.1 Illustration of the generation of Cu Kα X-rays

Figure 2.2 illustrates the Bragg's condition of interaction between crystal lattice and X-ray. The crystal planes are shown as horizontal black lines and the atoms are represented by black dots. The crystal planes have Miller indices of *hkl* and an inter-planar spacing of *d*. When a crystal is bombard by X-ray at certain angles, the incident ray 1 is scattered at atom A and the parallel incident ray 2 is scattered at atom B. If the traveling difference between the two beams equals to an integer number of wavelength, the reflected beams will interfere constructively. In this case, the relationship between the space of crystal planes d_{hkl}, the wavelength of incident beam λ and the angle of incidence θ can be expressed by the Bragg's law:

$$2\, d_{hkl}\, sin\theta = n\lambda\ , \qquad \text{(Eq. 2.1)}$$

where n is an integer representing the order of diffraction. The diffraction pattern is usually plotted as the intensity of the diffracted X-ray vs. the angle 2θ. A diffraction pattern contains many distinct peaks, each corresponding to a set of planes with the same inter-planar spacing *d* [79].

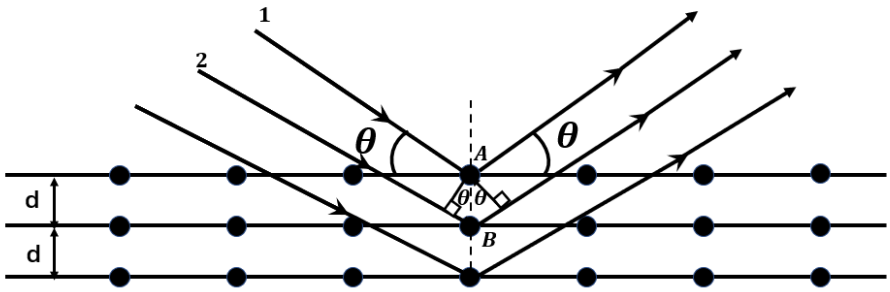

Figure 2.2 Illustration of diffraction of X-rays in a crystal (Bragg condition).

As shown in Figure 2.3, the unit cell of a crystalline material can be described in terms of lattice parameters *a*, *b* and *c* representing the lengths of edges, and α, β and γ representing angles between edges. There are in total seven types of crystal systems, and the restrictions of their lattice parameters are shown in Table 2.1. In different types of crystal systems, the relationship between lattice parameters and *d*-spacing varies. For example, the relationship in a material with orthorhombic symmetry can be expressed as follows:

$$\frac{1}{d_{hkl}^2} = \frac{h^2}{a^2} + \frac{k^2}{b^2} + \frac{l^2}{c^2} \quad , \qquad \text{(Eq. 2.2)}$$

where *a*, *b* and *c* are lattice parameters of the unit cell, *h*, *k* and *l* are the Miller indices of different sets of planes, and *d* is the spacing between two crystal planes. In order to make detailed analysis, the peaks in a diffraction pattern need to be indexed by assigning Miller indices *hkl* to each distinct peak. To obtain results with better accuracy, GSAS II [80] academic software is used to determine the crystal symmetry and refine the lattice parameters in this work.

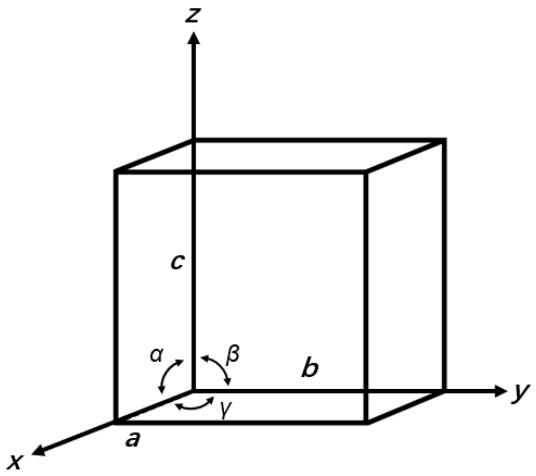

Figure 2.3 Space-lattice with lattice parameters labelled.

The ferroelectric materials studied in this work are of perovskite structure. The crystal symmetry of the materials varies with the temperature and the composition of the samples. For example, in a cubic unit cell ($a = b = c$), the calculated *d*-spacing of the $\{100\}_{cub}$ plane set using formula (Eq. 10) is a, and the calculated distances of $\{110\}_{cub}$ and $\{111\}_{cub}$ are $a/\sqrt{2}$ and $a/\sqrt{3}$, respectively, resulting in three distinct sets of peaks on the diffraction pattern. For the $\{100\}_{cub}$ plane set, $(100)_{cub}$, $(010)_{cub}$ and $(001)_{cub}$ have the same *d*-spacing of a, and cannot be distinguished from each other on the pattern, leading to an overlapping single peak.

Table 2.1 The seven crystal systems and specifications of their unit cells

Symmetry	Lattice Parameters	Angles
Cubic	a = b = c	α = β = γ = 90˚
Tetragonal	a = b ≠ c	α = β = γ = 90˚
Orthorhombic	a ≠ b ≠ c	α = β = γ = 90˚
Monoclinic	a ≠ b ≠ c	α = γ = 90˚; β ≠ 90˚
Triclinic	a ≠ b ≠ c	α ≠ β ≠ γ ≠ 90˚
Hexagonal	a = b ≠ c	α = β = 90˚ γ = 120˚
Rhombohedral	a = b = c	α = β = γ ≠ 90˚

When the cubic structure transforms into a lower symmetry, such as tetragonal

($a = b \neq c$), the three parameters are no longer identical, and the *d*-spacings of $(100)_{cub}$ and $(001)_{cub}$ are different. Therefore, for the $\{100\}_{cub}$ diffraction, two distinguishable peaks can be observed in the diffraction pattern. By judging the peak splitting and peak positions of key reflections in its X-ray pattern, it is feasible to determine the structural symmetry and phase of a material and investigate the transformation between different phases. Figure 2.4 shows the splitting of {100}, {110} and {111} reflection peaks in different crystal symmetries.

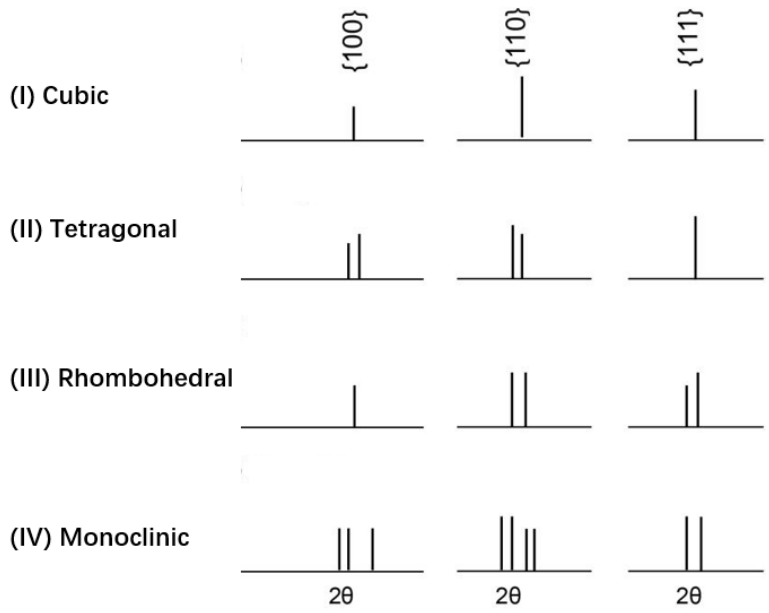

Figure 2.4 X-ray diffraction patterns for different symmetries with the corresponding splitting of the {100}, {110} and {111} reflections.

2.3. Dielectric Spectroscopy

Dielectric measurements provide us with the information on the dielectric permittivity, dielectric loss and phase transition temperature of a dielectric material. The dielectric properties are measured in terms of frequency and temperature using a Novocontrol Alpha high-resolution broad band dielectric spectroscopy. The sample is usually mounted in a sample cell and connected to two electrodes using gold wires, forming a sample parallel-plate capacitor.

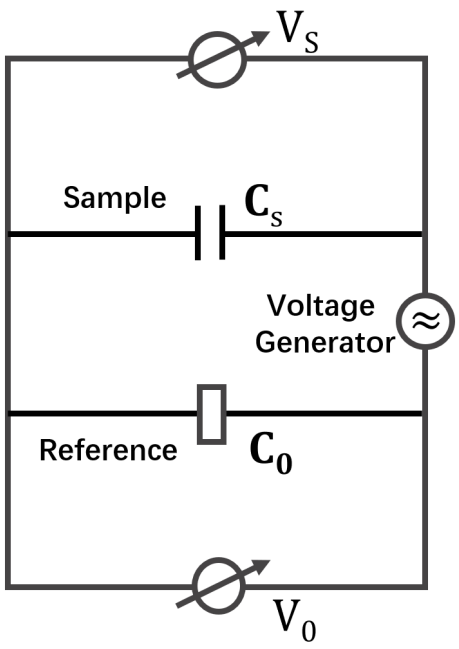

Figure 2.5 A schematic diagram of the frequency response analyzer circuit for dielectric spectroscopy.

A schematic diagram of the frequency response analyzer is shown in Figure 2.5. A single voltage generator applies voltage on a reference capacitor (C_0) and a sample capacitor (C_S). The applied voltage ranges from 1V ~ 3V with frequencies varying between 3 μHz and 20 MHz [48]. The voltage, the current flowing and the amplitude of capacitors are tested by two phase sensitive voltmeters, which give the voltages of reference capacitor (V_0) and sample capacitor (V_S). Since two capacitors are connected in series, the charge on the surface of each capacitor will be identical. The capacity of the sample can be calculated using following equations:

$$Q = C_0 * V_0 = C_S * V_S, \quad \text{(Eq. 2.3)}$$

$$C_S = \frac{C_0 * V_0}{V_S}. \quad \text{(Eq. 2.4)}$$

The relative dielectric permittivity (ε_r) of the sample can be then calculated by the formulae below:

$$C = \varepsilon_r \varepsilon_0 \left(\frac{A}{d}\right), \quad \text{(Eq. 2.5)}$$

$$\varepsilon_r = \frac{C_s * d}{A * \varepsilon_0}, \quad \text{(Eq. 2.6)}$$

where C_S is the sample capacitance, A is the area of the parallel electrode plates, d is the distance between the plates and ε_0 is the permittivity of the free space, which is 8.854×10^{-12} F/m [81], [82]. Dielectric loss exists and quantitatively describes dissipation of the electrical energy in materials [83], which should be considered in the expression of dielectric constant. Thus, the dielectric constant is in a complex form:

$$\varepsilon_r^* = \varepsilon' - i\varepsilon'' = \frac{C_s}{C_0}, \quad \text{(Eq. 2.7)}$$

where ε_r^* is the complex permittivity of the sample, ε' is the real part of permittivity and ε'' is the imaginary part of permittivity. The dielectric loss is defined as:

$$\tan(\delta) = \frac{\varepsilon''}{\varepsilon'}. \quad \text{(Eq. 2.8)}$$

As illustrated in Figure 2.6, δ is the angle between the real component and the imaginary component of the dielectric permittivity.

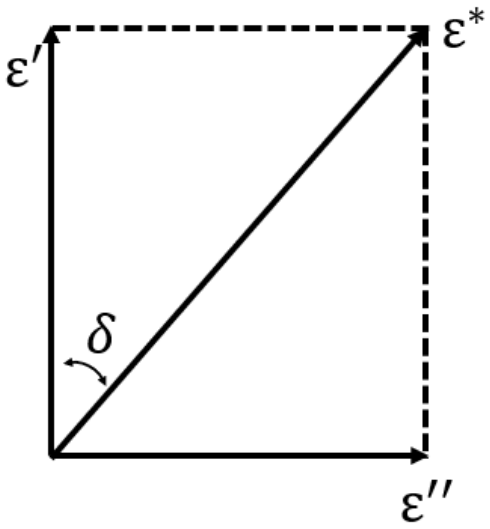

Figure 2.6 Illustration of the dielectric loss angle δ with the relation to the real and imaginary parts of permittivity.

2.4. Ferroelectric Hysteresis Measurements

In this research, the ferroelectric measurements are conducted by using an RT66A Standard Ferroelectric testing system (Radiant Technologies Inc.), which provides a ferroelectric hysteresis loop of the tested material. Ferroelectric properties of materials can be characterized by analysis of the hysteresis loop in terms of polarization (P) versus electric field (E) [84]. Figure 2.7 illustrates a schematic of circuit in a modified Sawyer-Tower instrument.

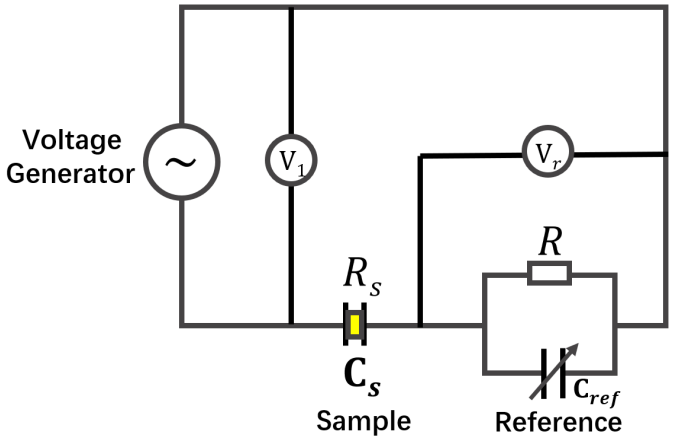

Figure 2.7 Illustration of the modified Sawyer-Tower circuit for the ferroelectric P-E loops measurements, where $C_{ref}, R_S\ R, V_1$ and V_r represent the reference capacitor, resistor of sample, the resistor, the step voltage and the voltage applied on the reference capacitor.

In this circuit, a sample capacitor (C_s) is connected in series with a RC circuit, which can compensate for the phase shift due to dielectric loss or conductivity in the sample [48]. An alternating voltage is applied across the parallel electrode plates of the sample capacitor. The charge on the surface of sample capacitor Q_s equals to the charge on the circuit of reference capacitor and resistor (R-C_{ref} circuit) since they are connected in series, which provides us the information of the charge on the sample. The polarization can be calculated by the following equation:

$$P = \frac{Q}{A}, \qquad \text{(Eq. 2.9)}$$

where P is the polarization of the sample, Q is the charge detected on the sample surface

and A is the area of the electrode plates. The applied electric field can be defined by:

$$E = \frac{V_s}{d}, \quad \text{(Eq. 2.10)}$$

where V_s is the voltage applied on the sample and d is the distance between electrode plates. Since the reference capacitor has a much larger capacitance compared to the sample's capacitance, the voltage applied on the sample can be approximately considered as the voltage applied to the circuit. With the information of measured polarization and applied electric field, a P-E hysteresis loop can be plotted, as shown in Figure 1.4. By analyzing the loop, one can obtain important characteristic physical quantities of the material, such as the coercive field and remanent polarization, which can then be used to characterize ferroelectric properties in samples. In relaxor materials, the shape of the P-E loops can be slim and narrow, or linear. Combined with the studies of the dielectric properties and structural phases, the ferroelectric measurements can be used to investigate the relaxor behaviour and the crossover from a relaxor state to a ferroelectric phase.

2.5. Transmission Electron Microscope

Transmission electron microscope (TEM) is a very useful tool to investigate the local and nano structures of materials. It is based on the fact that electrons accelerated by an electric field can penetrate distances of several micrometers into a solid, and they can be diffracted by planes of atoms in the crystalline materials, from which a transmission electron pattern can be obtained. In a TEM apparatus, high-energy electrons penetrate a thin specimen and are then focused by appropriate electromagnetic lens to produce images [85]. The magnified image of the specimen can be recorded and the obtained electron diffraction pattern is useful for analyzing the local structures of crystalline materials. The TEM apparatus can be divided into three sections: (1) illumination system, (2) specimen stage and (3) imaging system. A schematic diagram of the TEM instrument and principles of image formation are shown in Figure 2.8 [86].

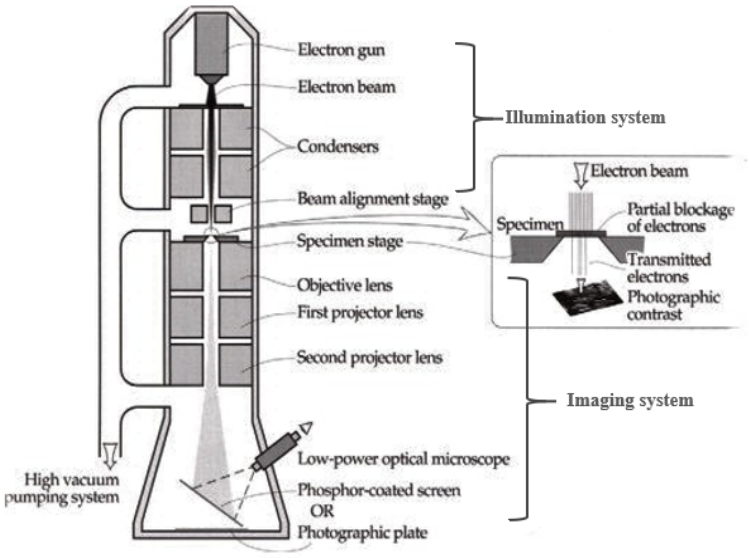

Figure 2.8 A schematic diagram of transmission electron microscope (TEM) (adapted from Ref. [87]).

The illumination system consists of an electron gun together with a condenser lens, which focuses electron beam onto the specimen. Operation of this system can determine the diameter of the electron beam and the intensity level in the final image. There are several kinds of electron sources used in TEM, such as thermionic emission, Schottky emission, field emission, etc. In particular, a thermionic electron gun contains an electron source, which is usually a V-shaped tungsten filament. When the filament is heated up to about 2700 K by a direct current, tungsten emits electrons into surrounding vacuum, and the process is known as the thermionic emission [85]. The emitted electrons are accelerated under an electric field that is applied parallel to the optic axis. A round metal plate with a central hole is placed vertically below the cathode where the electrons are emitted. The electron beam is emerged as it transmits through the hole. Most of the accelerated electrons are blocked and absorbed in anode plate and only 1% of them transmit through the hole as the beam. To produce magnified and clear images, a magnetic condenser lens is equipped in the instrument to adjust the magnification. Also, a condenser aperture is contained to control the convergence semi-angle of the illumination, which is the maximum angle that electrons can deviate from the optic axis. In the final part of the illumination system, there are two pairs of coils, which apply magnetic fields on the electron beam to ensure alignment to the beam and center the illumination on the screen.

The specimen measured in the TEM should be thin enough so that the electrons are allowed to transmit through the material instead of being absorbed. The standard shape of TEM specimen is usually circular with a diameter of 3 mm. The specimen stage is designed to be as stationary as possible because any shift and vibration of the stage will be magnified and lead to impairing of spatial resolution in the final image. The vacuum of the TEM column should not be broken when the specimen stage is inserted, so specimen can be inserted through an airlock, which is a small chamber that can be evacuated before the specimen enters the TEM column. The specimen stage is designed to be a side-entry stage, in which the sample is clamped close to the end of a rod-shaped holder and inserted into the airlock horizontally [85]. To activate the high vacuum valve and airlock evacuation valve, the specimen holder should be rotated and inserted into the column. This side-entry design of the specimen holder can provide precise motion and easily arranged heating of the specimen.

In the imaging system of TEM instruments, different imaging lenses are equipped to provide us an electron diffraction pattern or a magnified image on a camera or a phosphor coated viewing screen. The lens located closest to the specimen is called the objective lens. The objective lens is a strong lens with a small focal length, and it is capable of producing magnified images at a distance typically 10 cm below the center of the lens. An objective diaphragm is inserted at back-focal plane of the objective lens, where the diffraction pattern of the specimen will be obtained. The imaging system also contains a selected area aperture, which can be used to limit the region of the specimen where the electron-diffraction pattern is obtained. Only electrons falling in the diameter of the hole can transmit through the aperture. The intermediate lens is located between the objective lens and projector lens. The focal length of the intermediate lens can be adjusted in small steps to change the magnification of the image, which allows the overall magnification of the instrument to be varied from 10^3 to 10^6 typically. The projector lens can produce an image or electron-diffraction pattern with an overall diameter of several centimeters, and minimize the image distortion, which is caused by the long-distance travel of electrons. The electron image can be converted to a visible form on a phosphor screen, which consists of a metal plate. On the plate, there is a thin layer of fluoresces that emits visible light as it is bombarded by electrons.

In this work, TEM imaging was performed on a Hitachi 8100 transmission electron microscope operating at 200 keV with a thermal LaB_6 source. Point resolution of it is

0.24nm and the minimum spot size is 1 nm. Several imaging methods of the specimen are conducted and analyzed in this research, including standard bright field imaging, weak beam dark field imaging and electron diffraction pattern.

The bright field imaging is performed to analyze the morphology of the samples, such as micrometer and nanometer scale grains, grain boundaries and domains. Under this imaging mode, the morphology of the surface of the specimen can be displayed as the image with different contrast of areas. When interacted with various crystallite grains, electrons are scattered in different extents since each crystallite grain has different orientation of atoms alignment, which gives the contrast in the TEM bright field imaging and discrimination of crystallite grains. Figure 2.9 (a) shows an example of bright field TEM image [85].

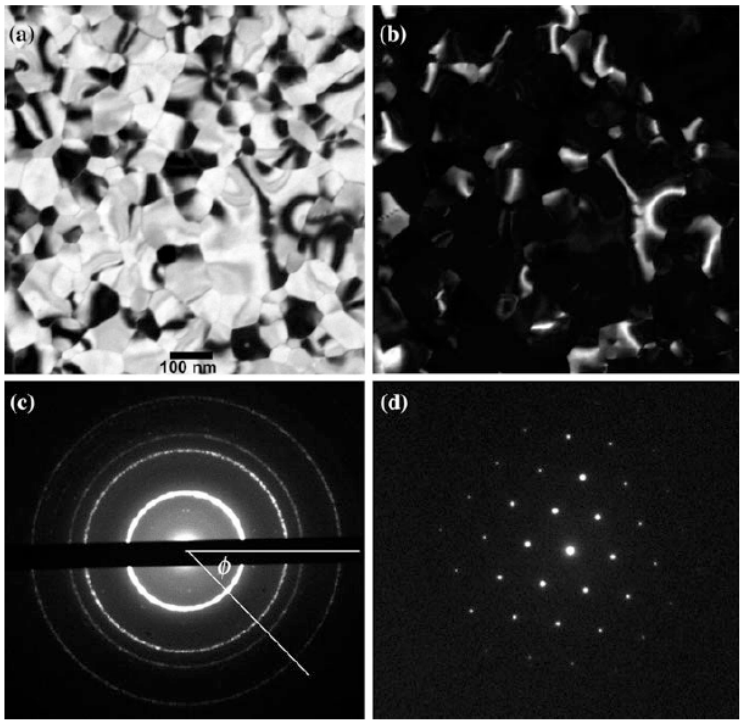

Figure 2.9 **(a) A bright-field TEM image of polycrystalline thin film of bismuth, (b) The dark field image of same region, (c) A ring diffraction pattern of crystallites, and (d) A spot diffraction pattern of Bi single crystallite (adapted from Ref. [86]).**

The standard dark field image is obtained from the two-beam diffraction condition by orienting the specimen. In this mode, the objective lens is horizontally displaced to block the transmitted electron beam. As a result, only the diffracted electron beam

contributes to the image. The strongly diffracted areas of specimen will show bright relative to their surroundings since the surrounding crystal does not produce diffracted intensity [66]. In the dark-field image, any part of the field of view that contains no specimen will show as dark fields. The dark field image is useful to study the characteristics of defects on the surface of the specimen. An example of dark field image is shown in Figure 2.9 (b)

Electron diffraction pattern can be used to identify the crystal symmetry, phase and chemical compositions of small crystallite regions within the specimen. By weakening the intermediate lens, the intermediate and projector lenses will magnify small diffraction pattern, which is formed at the back-focal plane of the objective lens [85]. In the diffraction pattern, zone axis is defined as the incident beam direction. By looking along the zone axis, sets of planes can be observed in the edge-on orientation. The zone axis can be expressed by a direction [*U V W*], which is perpendicular to the normal to the plane (*hkl*) if the plane is in the [*U V W*] zone. This result applies to all crystal systems and gives the Weiss zone law (Eq. 2.11) [87]:

$$hU + kV + lW = 0 \quad . \tag{Eq. 2.11}$$

The scattering of electrons is concentrated into the sharp peaks that satisfy the Bragg's law (Eq. 2.1). For example, if the specimen is a polycrystalline material, the diffraction pattern will show as several concentric rings centered on a bright central spot that represents the electrons travelling straight through the specimen (Figure 2.9 (c)). Each of the concentric ring corresponds to an orientation of atomic planes (*hkl*) and an inter-planar spacing *d*. Close examination of the rings reveals that they consist of a large number of spots, each arising from the Bragg reflection from an individual crystallite. A spot pattern will be observed if the specimen is a single crystal material, or the specimen has a large crystallite size that allows the focused electron beam to pass through only one single grain (Figure 2.9 (d)). In this case, the symmetry of the diffraction spots depends on the symmetry of the crystal structure and arrangement of atoms. For instance, a crystal with cubic symmetry gives a square array of diffracted spots. Each spot represents an orientation of the atomic plane.

Chapter 3.

Synthesis and Structure of A New Solid Solution $(1-x)(Pb_{0.5}Sr_{0.5})(Zr_{0.5}Ti_{0.5})O_3$-$xPbTiO_3$ of Complex Perovskite Structure

3.1. Abstract

To explore new lead-reduced materials in the $SrTiO_3$-$PbTiO_3$-$PbZrO_3$ ternary phase diagram system, and to understand the mechanisms behind the crossover between relaxor ferroelectric and normal ferroelectric materials, a novel solid solution between relaxor ferroelectric $(Pb_{0.5}Sr_{0.5})(Zr_{0.5}Ti_{0.5})O_3$, and ferroelectric $PbTiO_3$, namely $(1-x)(Pb_{0.5}Sr_{0.5})(Zr_{0.5}Ti_{0.5})O_3$-$xPbTiO_3$ (PSZT-PT), has been successfully synthesized by high-temperature solid state reaction method in the form of ceramics. The crystal structure and phase symmetry of the materials synthesized were analyzed and resolved based on X-ray powder diffraction (XRD) data, through both Pawley and Rietveld refinements using GSAS II academic software [80] . The results of the structural refinements indicate that at low PT concentration end of the phase diagram, e.g. x = 0.05, the PSZT-PT solid solution exhibits a cubic structural symmetry (with the space group Pm-3m). As the value of x increases, the structure of (1-x)PSZT-xPT gradually transforms from the cubic to a tetragonal (P4mm) phase. In the composition range of x = 0.10 to x = 0.25, a mixture of the cubic and tetragonal phases was identified. It is found that, as the concentration of PT increases, the proportion of the tetragonal phase increases at the expense of the cubic phase. When the x is greater than 0.175, the phase components are dominated by the tetragonal phase, and for the compositions of x > 0.25, a pure tetragonal phase is observed. Overall, a structural transformation (crossover) from a central-symmetric, non-polar cubic phase to a non-centrosymmetric, polar tetragonal phase is induced by the substitution of PT for PSZT in the pseudo-binary solid solution of (1-x)PSZT-xPT. These results will be helpful for the interpretation of the physical properties of this new system in the following Chapters.

3.2. Introduction

Since 1970s, PZT-based materials have become the most extensively used

electroceramic materials in a wide range of industrial and technological applications thanks to its outstanding performance around morphotropic phase boundary (MPB) region [60]. Additionally, as one of the representatives of relaxor-based materials, solid solution of $(1-x)Pb(Mg_{1/3}Nb_{2/3})O_3$-$xPbTiO_3$ (PMN-PT) also attracted great attention due to its excellent performance of piezoelectric properties [61], [62]. However, there are still no lead-free ferroelectric materials in production that have better versatility and performance than the lead-based materials [63], and the mechanism of relaxor behaviour is still poorly understood. Thus, the investigation of the transformation from relaxor to normal ferroelectrics can help us understand the differences between them, and provide us a path to study the mechanism behind relaxor ferroelectric behaviours. Meanwhile, useful systems of lead-reduced ferroelectric materials will be designed and synthesized, which will provide us with more options of relaxor-based functional materials. To obtain a PZT based material with relaxor behaviour, and reduce the concentration of Pb^{2+} cations, strontium titanate ($SrTiO_3$), an incipient ferroelectric material, is induced to PZT solid solution. In this case, both the Sr^{2+} and Pb^{2+} cations occupy the crystallographic equivalent A-sites, which leads to the compositional disorder in the system. Furthermore, by substituting Sr^{2+} for Pb^{2+} on the A-sites, the structural anisotropy can be reduced and it is possible to produce dense ceramics with high PT contents with good quality.

In order to investigate the interplays between various functional properties of oxide perovskite materials, including dielectric, piezoelectric, ferroelectric, antiferroelectric, relaxor ferroelectric, and quantum paraelectric, in this work, we intend to investigate a ternary materials system consisting of three end members: strontium titanate ($SrTiO_3$ or ST), lead titanate ($PbTiO_3$ or PT) and lead zirconate ($PbZrO_3$ or PZ), as shown in Figure 3.1. They form three binary systems as follows:

(i) lead zirconate titanate ($(1-x)PbZrO_3$-$xPbTiO_3$, Pb $(Zr_{1-x}Ti_x)O_3$, PZ-PT, or PZT),

(ii) strontium lead titanate ($(1-x)SrTiO_3$-$xPbTiO_3$, $(Pb_{1-x}Sr_x)TiO_3$, ST-PT, or SPT), and

(iii) lead strontium zirconate titanate ($(1-x)PbZrO_3$-$xSrTiO_3$, $(Pb_{1-x}Sr_x)(Zr_{1-x}Ti_x)O_3$ or PSZT).

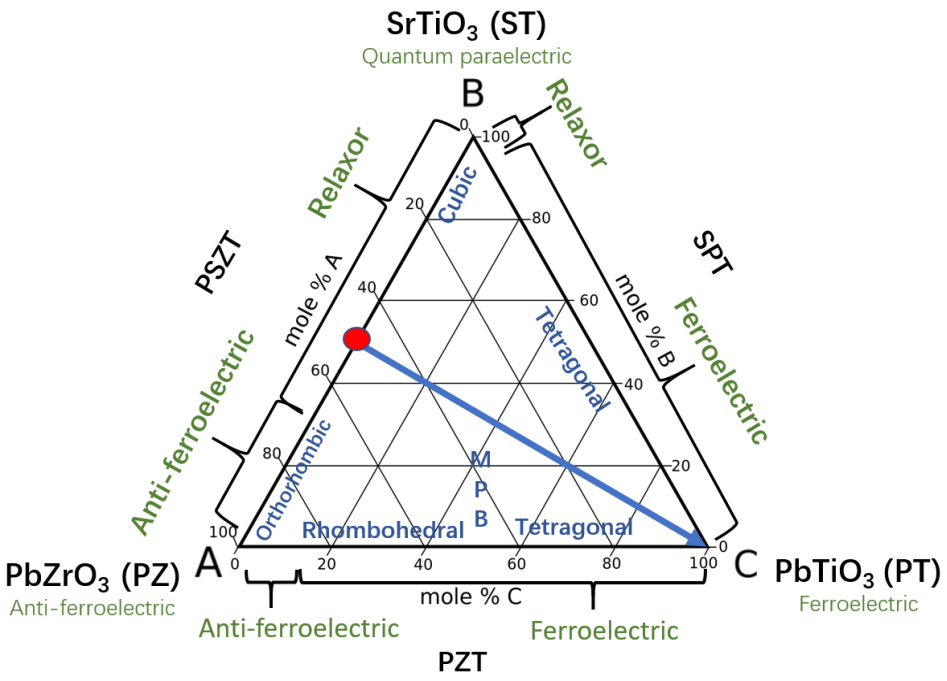

Figure 3.1 **A schematic ternary phase diagram consisting of strontium titanate (ST), lead titanate (PT) and lead zirconate (PZ), which form three binary systems, PS-ZT (PSZT), PZ-PT (PZT) and PT - ST (PST). Different phases and structural symmetries are illustrated in green and blue respectively. The new psuedo-binary solid solution of PSZT-PT, to be studied in this work, is represented by the blue line.**

The main features of each of the binary systems are described as follows in terms of their structures and properties.

Lead zirconate titanate ($(Pb(Zr_{1-x}Ti_x)O_3$ or PZT) is a binary solid solution between lead zirconate and lead titanate. The Curie temperature of PZT varies from 220 to 490 °C as a function of the composition [36]. PZT ceramics are the most widely used piezoelectric materials due to their outstanding electromechanical and piezoelectric properties for the compositions near the morphotropic phase boundary (MPB), as shown in Figure 1.11 [36]. Moreover, the PZT solid solution is important for the fundamental research, and many previous studies focused on the mechanisms behind the extraordinary piezoelectric properties near the MPB region. For compositions close to the MPB region, the useful properties such as electromechanical coupling factor (k_{33}), piezoelectric coefficient (d_{33}), remanent polarization (P_r) and dielectric permittivity (ε') all reach their maximum values, respectively [37], [88]. The highest piezoelectric response (~ 350 pC/N) was found for the MPB composition with x = 0.47 in this system [38].

On the other hand, lead strontium zirconate titanate ($(Pb_{1-x}Sr_x)(Zr_{1-x}Ti_x)O_3$ or PSZT), is formed by the continuous solid solution of strontium titanate (ST) and lead zirconate (PZ). The phase diagram of the PZ-ST system is illustrated in the Figure 3.2 (where x refers to the concentration of PZ, instead of ST).

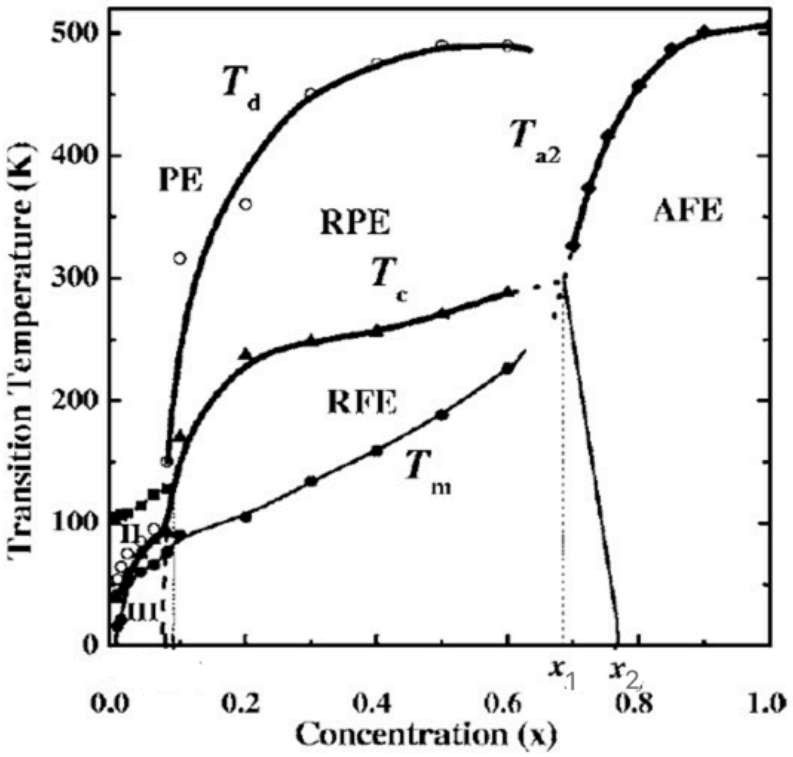

Figure 3.2 Illustration of phase diagram of the lead strontium zirconate titanate binary system, with x representing lead zirconate contents. The marked lines are the dielectric constant peak temperature (T_m), the Curie-Weiss temperature (T_C), the antiferrodistortive phase transition temperatures (T_{a2}), and the Burns temperature (T_d). The marked regions indicate the relaxor phases (RFE and RPE), the paraelectric phase (PE), and the antiferroelectric phase (AFE). The compositions x_1 and x_2 mark the phase boundary (region) between relaxor and antiferroelectric phase (adapted from Ref. [76]).

At room temperature, the PSZT is in the relaxor ferroelectric phase when the concentration of $PbZrO_3$ (x) is below 0.7. For x (PZ) > 0.7, PSZT is in the antiferroelectric phase. The boundary (region) between the antiferroelectric and relaxor phases is delimited from x = 0.69 to 0.78, which is shown as the area under the oblique line between x_1 and x_2 on the graph. At high temperatures, the PSZT ceramics exhibit a paraelectric

phase, and the phase transition temperature between the relaxor phase and the paraelectric phase is shown as T_d, which is considered as the Burns temperature [76]. The antiferrodistortive phase transition temperature (T_{a2}) is the boundary between antiferroelectric phase and paraelectric phase. In addition, the temperature of the maximum dielectric permittivity, T_{max}, increases with the increase of lead zirconate concentration. As a characteristic composition showing typical realxor behaviour, the composition of $(Pb_{0.5}Sr_{0.5})(Zr_{0.5}Ti_{0.5})O_3$ (x = 0.5) is chosen to be the starting compound to be studied in this work. In addition, the T_{max} of $(Pb_{0.5}Sr_{0.5})(Zr_{0.5}Ti_{0.5})O_3$ is around 190 K and its phase transition temperature T_C is around room temperature, making it convenient to characterize the materials prepared using our in-house equipment.

Another related binary system is the solid solution of lead strontium titanate (ST-PT or SPT). Its Curie temperature (T_C) as a function of different SPT compositions is shown in Figure 3.3.

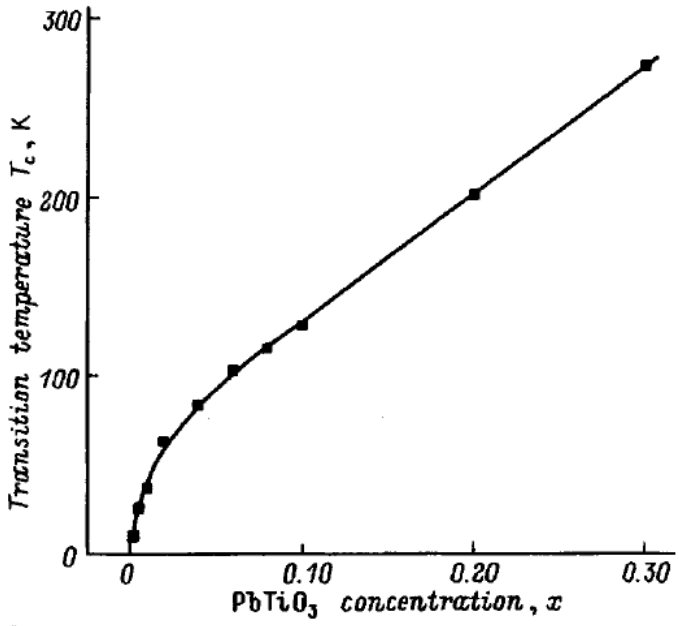

Figure 3.3 Variation of the Curie temperature (T_C) as a function of the strontium titanate concentration in the (1-x)$SrTiO_3$ - x$PbTiO_3$ (SPT) binary system (adapted from Ref. [89]).

In Lemanov and Smirnova's work [89], for a narrow composition range in which the PT concentration is below 0.05, the ferroelectric measurements showed slim and almost linear loops, and a frequency dispersion of dielectric constant was observed, which

was considered as relaxor behaviour [90]. The concentration of lead titanate (PT) at 0.05 was considered as the tricritical point where the first-order transition becomes a second-order transition [89]. As the concentration of PT increases, the ferroelectric phase starts to dominate at low temperature. Thus, at very low PT concentrations, the SPT samples show relaxor behaviour, and as the PT concentration becomes higher than 0.05, SPT exhibits a normal ferroelectric phase. In addition, upon heating, SPT transforms from the tetragonal (P*4mm*) to cubic (P*m-3m*) at Curie temperatures T_C, as shown in Figure 3.3 [91]

Although the respective binary systems have been studied, the ternary phase diagram shown in Figure 3.1, remains unknown, especially in terms of phases, crystal structures and physical properties of the ternary compounds. Therefore, in this work, a new solid solution between the binary relaxor ferroelectric $(Pb_{0.5}Sr_{0.5})(Zr_{0.5}Ti_{0.5})O_3$ and the ferroelectric $PbTiO_3$, namely $(1-x)(Pb_{0.5}Sr_{0.5})(Zr_{0.5}Ti_{0.5})O_3$-$xPbTiO_3$ (PSZT-PT), which is highlighted by the blue line in Figure 3.1, has been studied, as a representative pseudo-binary system, to explore the evolutions of the phase components, crystal structures, phase transitions, and physical properties of the ternary system. The synthesis and structural analysis of the PSZT-PT system are presented in this chapter.

3.3. Experimental

3.3.1. Synthesis

The solid solutions of $(1-x)(Pb_{0.5}Sr_{0.5})(Zr_{0.5}Ti_{0.5})O_3$-$xPbTiO_3$ with various compositions (x = 0.05, 0.10, 0.15, 0.175, 0.20, 0.225, 0.25, 0.275, 0.30, 0.35, 0.50, 0.65, 0.75, 0.85 and 0.95) were successfully synthesized in the form of ceramics by solid state reaction. The raw materials, strontium carbonate ($SrCO_3$, 99.9%, Aldrich), lead oxide (PbO, 99.9%, Alfa Aesar), zirconium oxide (ZrO_2, 99.0%, Aldrich), and titanium oxide (TiO_2, 99.5%, Alfa Aesar), were weighed according to the stoichiometric amounts and then mixed together homogeneously. The following equation (Eq. 3.1) shows the solid state reaction for the formation of the $(1-x)(Pb_{0.5}Sr_{0.5})(Zr_{0.5}Ti_{0.5})O_3$-$xPbTiO_3$ solid solution:

$$(0.5-0.5x)ZrO_2 + (0.5-0.5x)SrCO_3 + (0.5+0.5x)TiO_2 + (0.5+0.5x)PbO \rightarrow (0.5-0.5x)CO_2 + (Pb_{(0.5+0.5x)}Sr_{(0.5-0.5x)})(Zr_{(0.5-0.5x)}Ti_{(0.5+0.5x)})O_3 \ . \quad \text{(Eq. 3.1)}$$

As the first step, the powders of raw materials were mixed and hand ground for two hours in an agate mortar with constant addition of ethanol to facilitate homogenization. The resulting mixed powder from step one was then air-dried and pressed uniaxially into a disc-shaped pellet with a diameter of 10 mm, which was then placed on a platinum plate and calcined at 950°C for 6 hours. The calcined pellets were examined by X-ray powder diffraction to identify the main structural phase and check the phase purity. If the desired perovskite phase was obtained, the pellets were then pulverized and ball-milled with zirconate oxide (ZrO_2) balls using ethanol as ball-milling media. After 24-hour ball milling, the powder was air-dried again and ground with addition of 1 wt.% polyvinyl alcohol (PVA) as binder, which could ultimately help enhance the density of the final products to form ceramics. The mixture was then pressed into pellets with a diameter of 10 mm and thickness of 1.2 mm. The pellets were first heated at 550 °C for 1 hour to eliminate the PVA binder, then sintered at 1175 - 1275°C for 4 hours on a platinum plate in a sealed aluminum crucible. The optimized sintering temperatures used for the synthesis of different compositions are listed in the Table 3.1 below. The sintering temperature decreases as the lead titanate substituting amount increases in the system, which is due to the lower melting point (888 °C) of PbO compared to that of SrO (2531°C). In addition, the melting point of TiO_2 (1843°C) is also lower than that of ZrO_2 (2715°C).

Table 3.1 Different sintering temperatures used for the sintering of the (1-x)PSZT-xPT ceramics of different compositions

x	0.05	0.10	0.15	0.25	0.35	0.5	0.75	0.95
Sintering temperature (°C)	1275	1275	1250	1250	1200	1200	1175	1175

3.3.2. Structural Analysis

X-ray diffraction (XRD) technique was used to identify the phases formed, to check the phase purity and to determine the crystal structures and symmetries of the phases present for each composition. To determine the phases and crystal structures of the prepared ceramics, the pellets were ground to powder and examined by X-ray powder diffraction using XRD1: Rigaku Diffractometer, 46 mA, 42 kV, 2θ = 10 ° - 80 °, Ω = 200 °, Φ =270 °, χ = 45 °; and XRD2: Bruker D8 Advance Diffractometer, 40 mA, 40 kV, 0.01° steps, 2θ = 20°- 80°. The XRD data were analyzed by GSAS II software [80] using both

Pawley and Rietveld refinement methods to determine the phase symmetry, phase components and fractions and lattice parameters.

3.4. Results and Discussion

3.4.1. Phase Identification and Structural Evolution from XRD Patterns

Figure 3.4 shows the X-ray diffraction patterns of various compositions of the (1-x) $(Pb_{0.5}Sr_{0.5})(Zr_{0.5}Ti_{0.5})O_3$-$xPbTiO_3$ (x = 0.05, 0.15, 0.25, 0.35, 0.50, 0.65, 0.75, 0.85 and 0.95) solid solution measured at room temperature. The patterns show that a pure phase of perovskite structure is successfully synthesized for all the compositions, indicating that PSZT and PT form a continuous solid solution. Note that in some compositions, a very weak impurity peak can be observed at 2θ = 28.24 degree in the XRD patterns, as shown in Figure. 3.5. It is found to belong to the residual ZrO_2. Since its fraction is estimated to be about 1.6% (see Sec. 3.4.2) vs the perovskite phase, this trace amount of ZrO_2 is believed not to affect the structures and properties of the system.

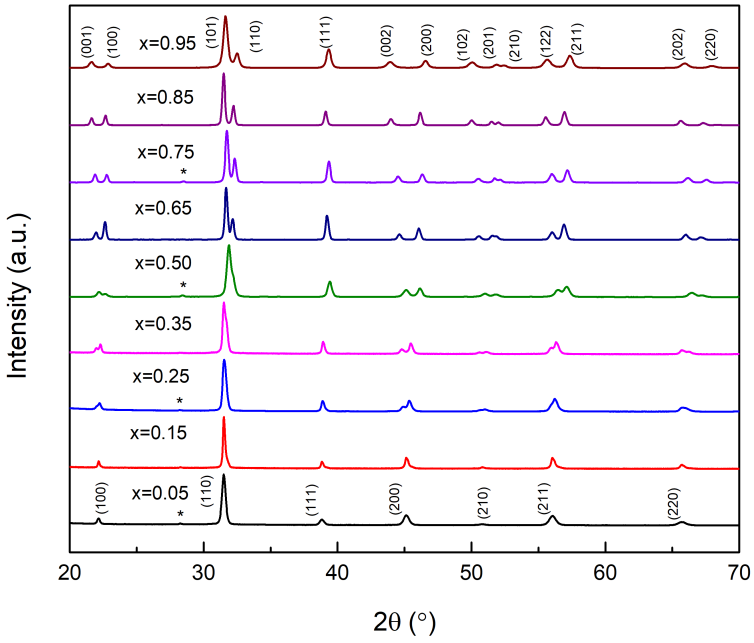

Figure 3.4 **X-ray diffraction patterns of the (1-x)$(Pb_{0.5}Sr_{0.5})(Zr_{0.5}Ti_{0.5})O_3$ – $xPbTiO_3$ (x = 0.05, 0.15, 0.25, 0.35, 0.50, 0.65, 0.75, 0.85 and 0.95) solid solution ceramics. The peaks are indexed into the perovskite structure of cubic or tetragonal symmetry. Stars indicate the peak of the residual ZrO_2.**

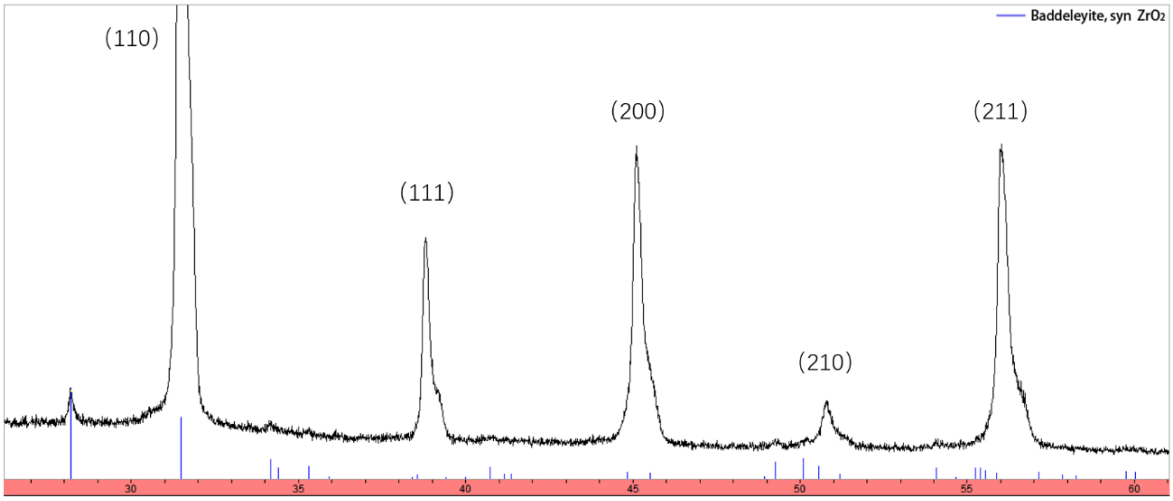

Figure 3.5 **X-ray diffraction pattern of the (1-x)($Pb_{0.5}Sr_{0.5}$)($Zr_{0.5}Ti_{0.5}$)O_3 – x$PbTiO_3$ (x = 0.20, black) and the peaks of ZrO_2 (blue lines) from Jade software. Reference of ZrO_2: PDF reference number 37-1484, monoclinic phase with space group P21/a.**

the XRD patterns of PSZT-PT with low $PbTiO_3$ concentrations (x < 0.25) show diffraction peaks of a typical perovskite structure without any peak splitting, indicating a cubic symmetry. At concentration of x = 0.25, the splitting of peaks can be observed for the sets of peaks {100}, {110}, {200}), {210} and {211}, which indicates a tetragonal symmetry. As the concentration of $PbTiO_3$ increases above 0.50, the peak splitting becomes more obvious. The set of {100} peaks splits into (101) and (110), and the set of {210} peaks splits into (210) and (201), confirming the establishment of the tetragonal unit cell with c > a = b, which is induced by the substitution of PT for PSZT. The evidence of splitting for the sets of peaks {100}, {110}, {200}, {210} and {211} is seen more clearly with further increase of PT concentration up to x = 0.95. Therefore, it is reasonable to assume that a pure tetragonal phase is formed in the PSZT-PT samples with high x concentration and this will be proved later by more detailed structural refinements using GSAS II. For now, it can be seen that, in general, with increasing concentration of $PbTiO_3$, the structural symmetry of PSZT-PT gradually transforms from cubic into tetragonal.

In addition, with the increase of PT concentration x, the average position (angle) of all the peaks shifts towards higher angle. The shift of the center of the set of {110} peaks can be clearly observed in Figure 3.6. According to the Bragg's law (Eq. 2.1), as an increase in the 2θ angle implies a decrease in the d spacing, which indicates that the volume of unit cell reduces as x increases.

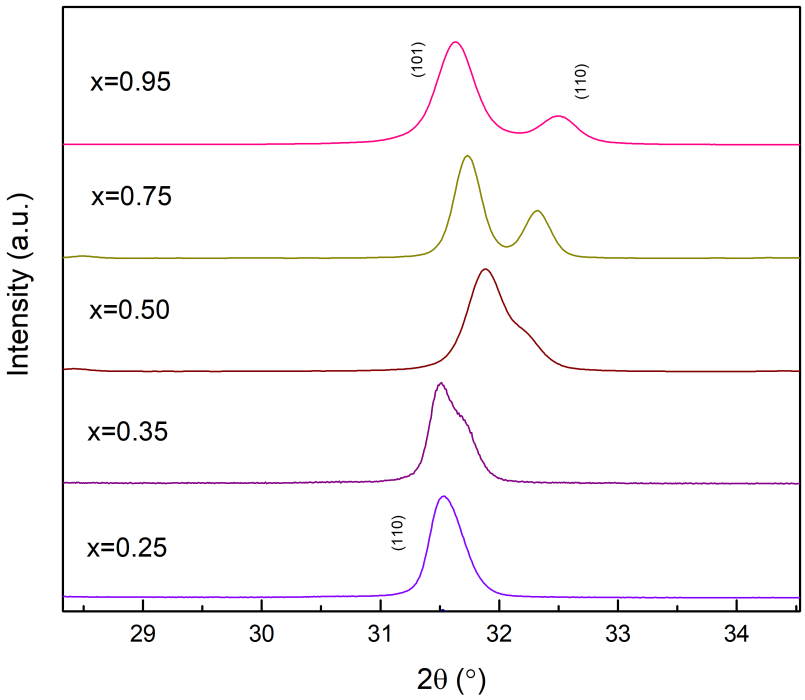

Figure 3.6 **Enlargement of the set of {110} peaks from the X-ray diffraction patterns of the (1-x)($Pb_{0.5}Sr_{0.5}$)($Zr_{0.5}Ti_{0.5}$)O_3 – x$PbTiO_3$ (x = 0.25, 0.35, 0.50, 0.75, 0.95) solid solution.**

In Figure 3.4, it should be noticed that the splitting of peaks occurs when x is at 0.25, where the tetragonal phase starts to emerge and it gradually becomes a major phase with further increase of x. For the compositions of x < 0.25, the splitting of peaks is not observed clearly, but some deformation of the peak profile (shape) can be suspected, hinting that an intermediate state with the mixture of the cubic and tetragonal phase may exist. In order to study the phase components and structural symmetries in this region in more detail, more compositions with finer internals, namely x = 0.10, 0.175, 0.20, and 0.225, have been synthesized and characterized by X-ray powder diffraction, and the XRD patterns are shown in Figure 3.7.

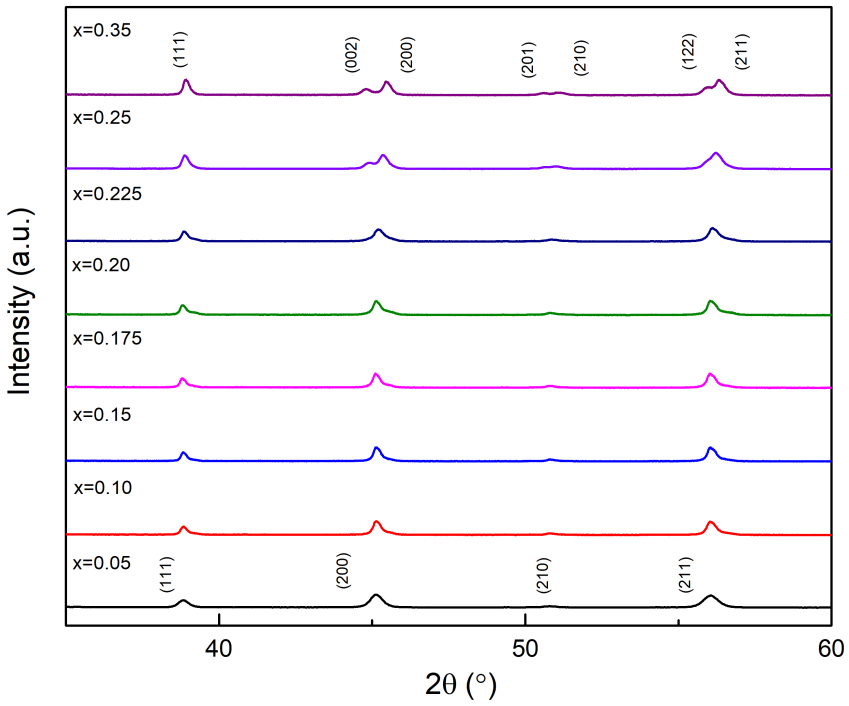

Figure 3.7 Enlargement of X-ray diffraction patterns of the (1-x)($Pb_{0.5}Sr_{0.5}$)($Zr_{0.5}Ti_{0.5}$)O_3 – x$PbTiO_3$ (x = 0.05, 0.10, 0.15, 0.175, 0.20, 0.225, 0.25 and 0.35) solid solution with finer intervals in the intermediate compositional region.

At x = 0.05, the shape of all the peaks is symmetric with no splitting, which indicates a pure cubic phase. As the concentration of $PbTiO_3$ increases, the shape of the sets of {200} and {211} peaks becomes asymmetric with the presence of a small shoulder, which suggest the onset of the mixed phases consisting of the tetragonal and cubic symmetries, respectively. With further increase of x, the asymmetric peak with shoulder gradually transforms into split peaks, with the primary and secondary peaks separating further apart from each other. At x = 0.35, the original {200} peak has clearly split into two individual peaks and the splitting of the peak {211} can also be observed clearly, indicating the establishment of a pure tetragonal symmetry. Thus, between the cubic symmetry of low PT concentration and the tetragonal symmetry of high PT contents, an intermediate state with a mixture of the cubic and tetragonal phases possibly exists within the composition range of x = 0.10 to 0.25. To confirm the exact range of the phase coexistence and the fractions of the coexisting phases, more detailed structural refinements need to be conducted, as shown in the following section.

3.4.2. Structural Refinements by GSAS II

In order to better study the gradual structural transformation as a function of composition in PSZT-PT, the XRD results of all compositions are refined and analyzed using GSAS II software. Both the Pawley and Rietveld refinements are carried out to determine the phase components, phase fraction, and lattice parameters of all the compositions studied in this work. The Pawley refinement method provides the basic fitting for crystal structure of the samples by refining the peak position, peak intensity and peak width of each reflection individually [92]. The structural information of the unit cell, such as lattice parameters and structural symmetry, can be determined by the Pawley refinement. When fitting with multiple phases is required, the Rietveld refinement is used to obtain the phase information and phase fraction by calculating the intensities of the peaks from imported structural phase [93].

Initially, the Pawley refinement method is applied on the composition of x = 0.05. As shown in Figure 3.8, the refinement results for the composition of x = 0.05 indicate that the crystal symmetry of this composition is of cubic phase (P*m-3m*). The experimental data (obs on the graph), the calculated pattern (calc) and the difference (diff) between them are presented in Figure 3.8 below. The agreement weighted profile R-factor (R_{wp}) is defined as the criterion for judging the quality of refinements; of greater importance is the "chemical reasonableness" of the fitting model [94]. A good fitting of model usually gives a low R_{wp} value. For this refinement, R_{wp} is 1.9%, which indicates a good quality of the refinements. The obtained lattice parameters (a = b = c) is 4.0153 Å with an uncertainty of 0.0001Å, and the refined volume of the unit cell is 64.74 $Å^3$ for the x = 0.05 sample.

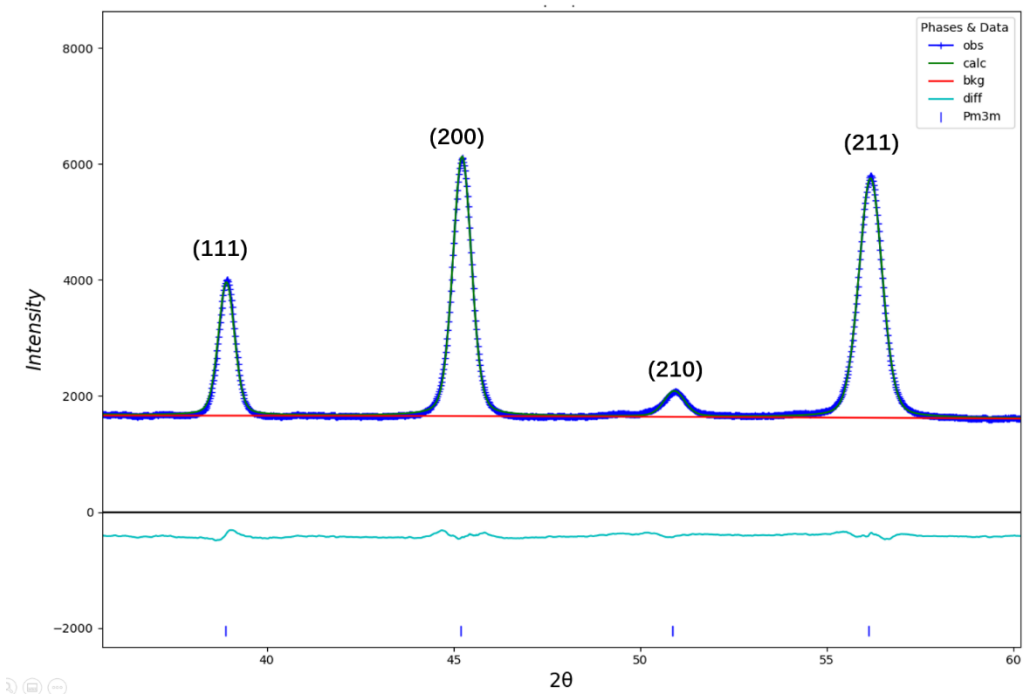

Figure 3.8 **The structural refinement results for the (1-x)($Pb_{0.5}Sr_{0.5}$)($Zr_{0.5}Ti_{0.5}$)O_3 – x$PbTiO_3$ solid solution with x = 0.05. The legends are: curve of experimental data (obs, blue line and dots), calculated curve (calc, green line), background curve (bkg, red) and difference between the experimental data and calculated curve (diff, light blue). The vertical blue lines represent the positions of peaks in the corresponding phase.**

As shown in Figure 3.9, the major peak of the impurity phase is also refined by the Pawley refinement method. The peak at 2 θ= 28.24 ° of the XRD pattern matches well the strongest reflection of ZrO_2, which has a crystal symmetry of monoclinic with the space group of P21/a. However, because the concentration of the ZrO_2 phase in the sample is extremely low and the resolution of the lab X-ray data is not so good, our attempt to determine the phase fraction of ZrO_2 by the Rietveld refinement was not sufficient. To estimate the percentage of the ZrO_2 impurity, the peak areas of the strongest reflections from the perovskite phase and the ZrO_2 phase are calculated from Jade software, from which the phase fraction of the residual ZrO_2 phase is estimated to be 1.6%.

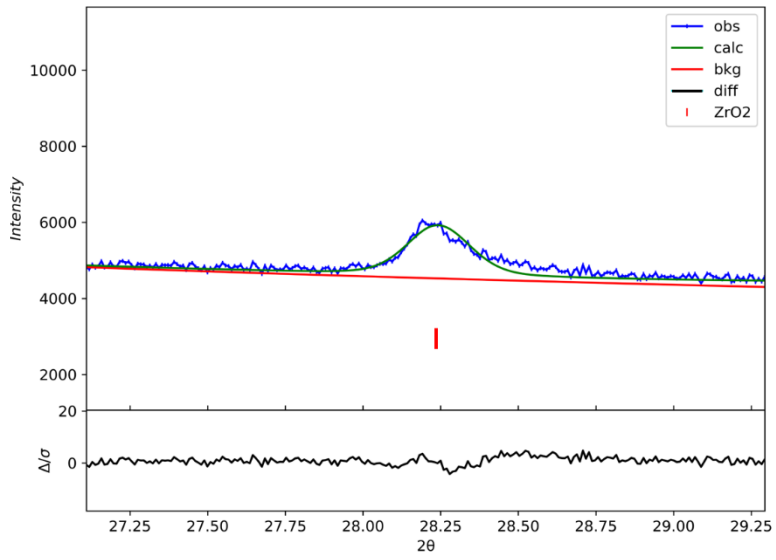

Figure 3.9 **The refinement result of the residual ZrO_2 phase in the XRD pattern of $(1-x)(Pb_{0.5}Sr_{0.5})(Zr_{0.5}Ti_{0.5})O_3 - xPbTiO_3$ (x = 0.05). The legends are: curve of experimental data (obs, blue line and dots), calculated curve (calc, green line), background curve (bkg, red) and difference between the experimental data and calculated curve (diff, light blue). The vertical blue lines represent the positions of peaks in the corresponding phase.**

For the composition of x = 0.10, the XRD data are first analyzed using a cubic (Pm-3m) model. However, as shown in Figure 3.10 (a), there is a big difference between the calculated curve and the experimental data in terms of peak intensity and position. Accordingly, the R_{wp} value reaches 14.2%, which indicates a poor fit with the single cubic phase model. To resolve the true phase components, a tetragonal (P*4mm*) phase is then added in, and the Rietveld refinement is carried out using a mixture of the cubic and tetragonal phases. It is found that with the addition of the tetragonal phase, the quality of refinement is significantly improved, and the R_{wp} value decreases from 14.2% to 5.4%. As shown in Figure 3.10 (b), the calculated curve matches the experimental data much better than before, and the difference is significantly reduced. Therefore, it is reasonable to conclude that the composition of x = 0.10 contains a mixture of the cubic (P*m-3m*) and tetragonal (*P4mm*) phases. Furthermore, the fractions of the cubic and tetragonal phases are calculated to be 88.7% and 11.3%, respectively, indicating that the tetragonal phase starts to form, while the cubic phase remains the majority phase, in the solid solution of 0.90PSZT-0.10PT.

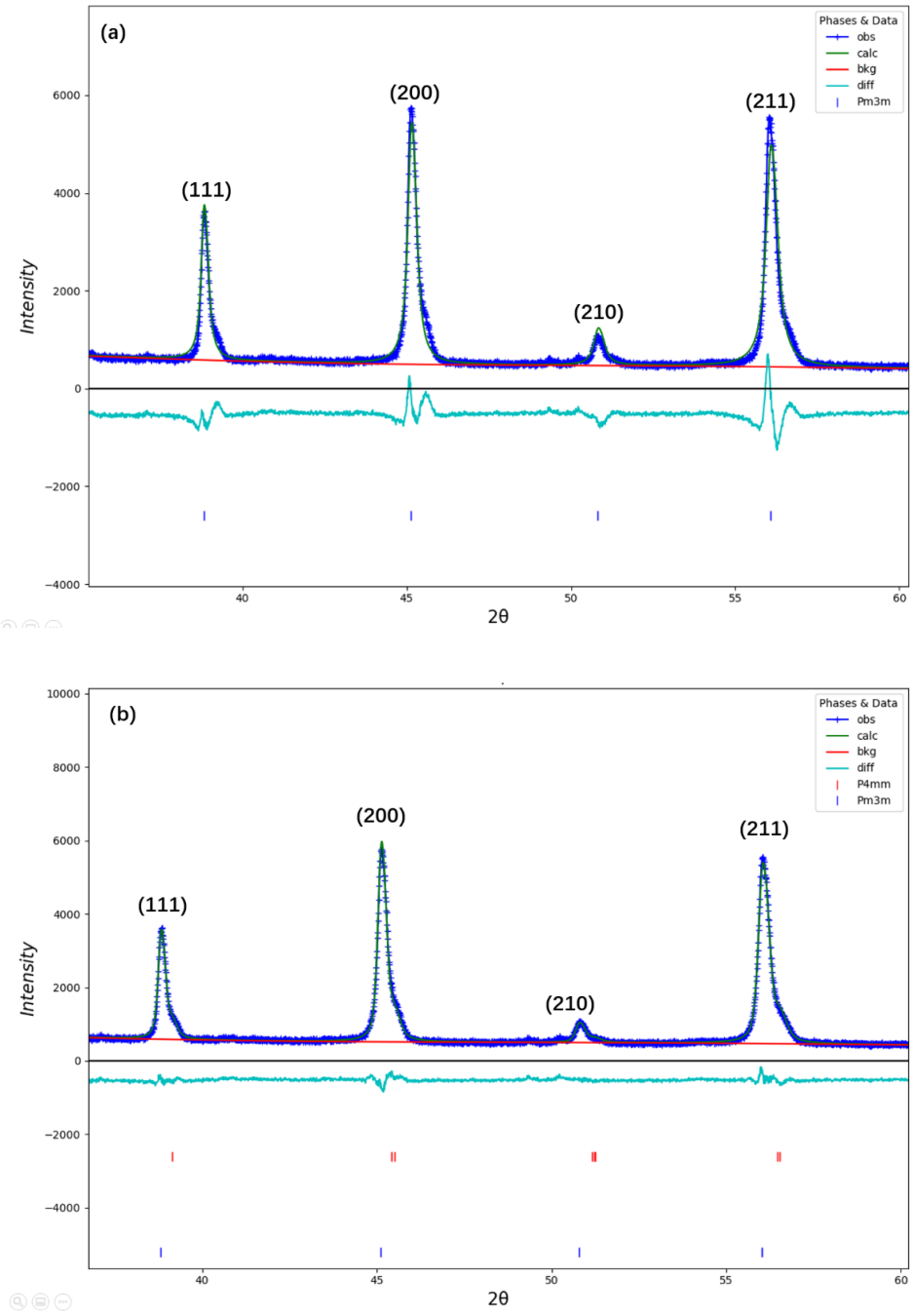

Figure 3.10 **The refinement results from the fittings with (a) only cubic (*Pm-3m*) phase, and (b) both cubic and tetragonal (*P4mm*) phases, of the XRD pattern of the (1-x)($Pb_{0.5}Sr_{0.5}$)($Zr_{0.5}Ti_{0.5}$)O_3 – x$PbTiO_3$ solid solution with x = 0.10. The legends are: curve of experimental data (obs, blue line and dots), calculated curve (calc, green line), background curve (bkg, red) and difference between the experimental data and calculated curve (diff, light blue). The vertical blue lines represent the positions of peaks in the corresponding phase.**

Similar approach is then applied to the structural refinements of the XRD patterns of the compositions x > 0.10, using a model of combined cubic and tetragonal phases. It is found that all the compositions within 0.10 < x < 0.25 can be well fitted with a mixture of the cubic and tetragonal phases. However, when x reaches 0.275, the experiment data are best fitted with a single tetragonal phase, rather than a mixture of the tetragonal and cubic phases, indicating the upper limit of the composition region for the mixed phases and the end of the phase transformation from the cubic to tetragonal phase (Figure 3.11).

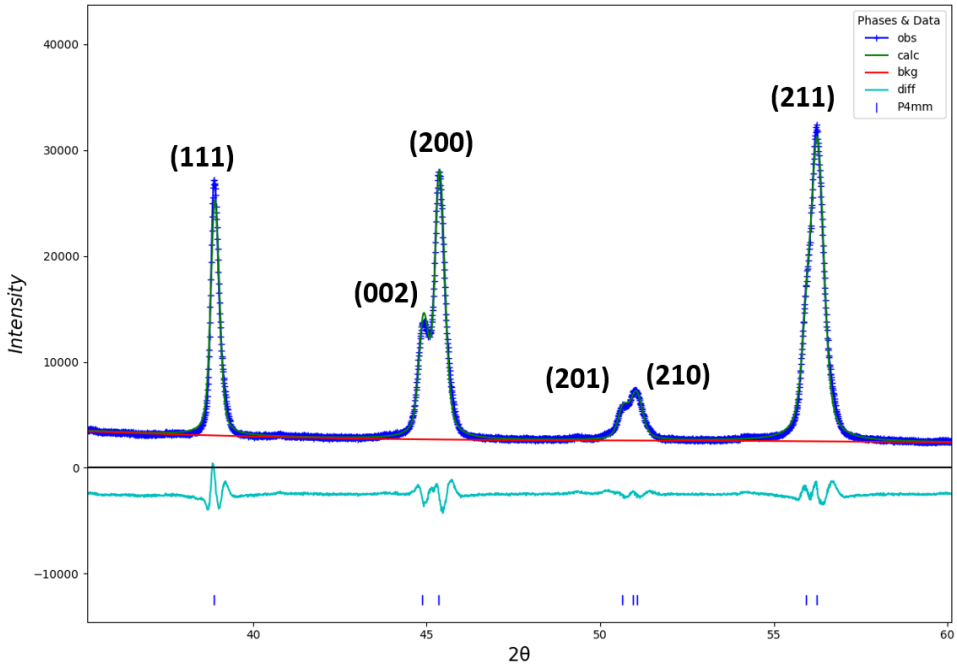

Figure 3.11 **The refinement result of (1-x)($Pb_{0.5}Sr_{0.5}$)($Zr_{0.5}Ti_{0.5}$)O_3 – x$PbTiO_3$ (x = 0.275) using a single tetragonal phase (*P4mm*) model. The legends are: curve of experimental data (obs, blue line and dots), calculated curve (calc, green line), background curve (bkg, red) and difference between the experimental data and calculated curve (diff, light blue). The vertical blue lines represent the positions of peaks in the corresponding phase.**

Based on the refinement results of the intermediate compositions with mixed phases, the fractions of the cubic (*Pm-3m*) and tetragonal (*P4mm*) phases with x from 0.05 to 0.275 are calculated and the results are presented in Figure 3.12. It can be seen that with the substitution of PT for PSZT, the tetragonal phase first appears in a small amount in x = 0.10, and its fraction continues to increase, at the expense of the cubic phase fraction, with further increase of PT concentration, more sharply from x = 0.15 to

0.20. When x is larger than 0.175, the tetragonal phase becomes the majority phase, taking over the cubic phase. At x = 0.275, the cubic phase disappears, leaving only the tetragonal phase. Therefore, the trends of the phase fractions indicate clearly that the structural symmetry of the PSZT-PT solid solution transforms from the cubic phase to the tetragonal, passing through an intermediate composition region where the crossover from the cubic to tetragonal phase takes place with the increase of PT concentration.

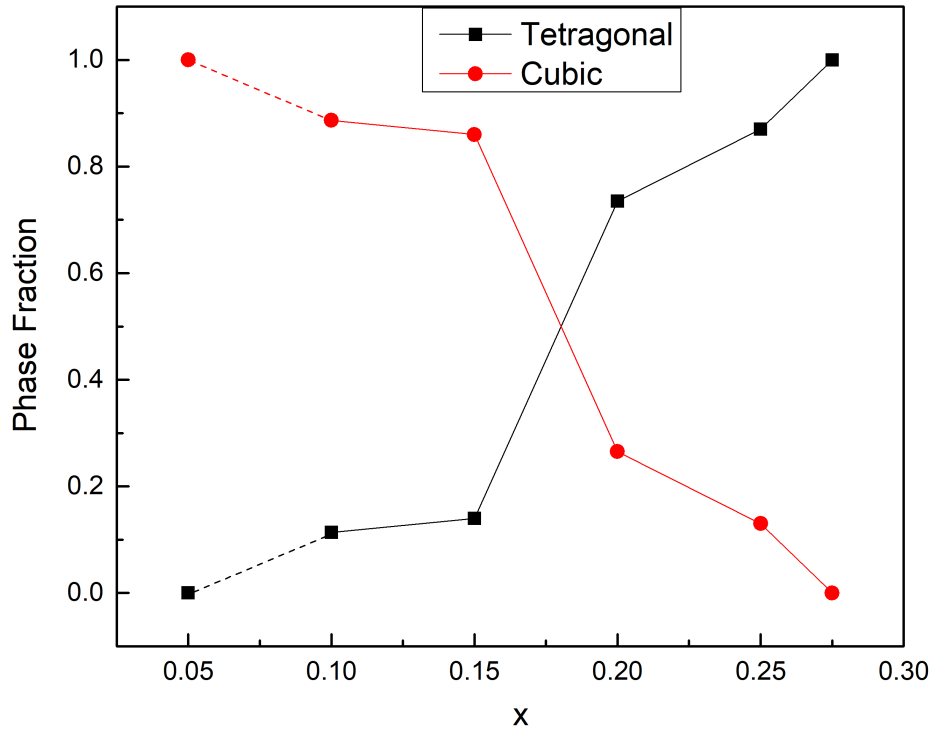

Figure 3.12 Fractions of the cubic and tetragonal phases as a function of composition x in the (1-x)($Pb_{0.5}Sr_{0.5}$)($Zr_{0.5}Ti_{0.5}$)O_3 – x$PbTiO_3$ (x = 0.05, 0.10, 0.15, 0.20, 0.25, 0.275) solid solution, as refined from the XRD data using GSAS II.

It should be noted that the coexisting cubic and tetragonal phases exist in the forms of solid solutions in the intermediate region, namely the PSZT-PT solid solution of cubic (*Pm-3m*) structure and the PSZT-PT solid solution of tetragonal (*P4mm*) structure. As shown in the following paragraphs, the lattice parameters and volumes of these two phases vary across the intermediate region and beyond, suggesting that the compositions of the two existing phases continue to change accordingly, consistent with the characteristics of solid solutions.

Figure 3.13 shows the variation of the lattice parameters of the PSZT-PT solid solution as a function of composition obtained from the Pawley refinements. As x increases, the lattice parameter *c* of the tetragonal phase shows a general increasing trend, while the lattice parameter *a* exhibits a clear descending trend, for compositions of x > 0.20. In the intermediate composition region where both the cubic and tetragonal phase coexist, a crossover of the lattice parameter *a* between the cubic and tetragonal phases occurs around x = 0.175, where the tetragonal phase begins to take dominance and the fraction of the cubic phase in mixed phases gradually fades out. As a result, the lattice parameter *a* of the cubic phase decreases abruptly, while the lattice parameter *a* of the tetragonal phase increases sharply in the mixed phase region. Outside the intermediate composition region, the lattice parameter *a* of the cubic phase (x < 0.20) and the tetragonal phase (x ≥ 0.20) can be considered to link together, giving rise to an overall decreasing trend with the increase of the PT concentration.

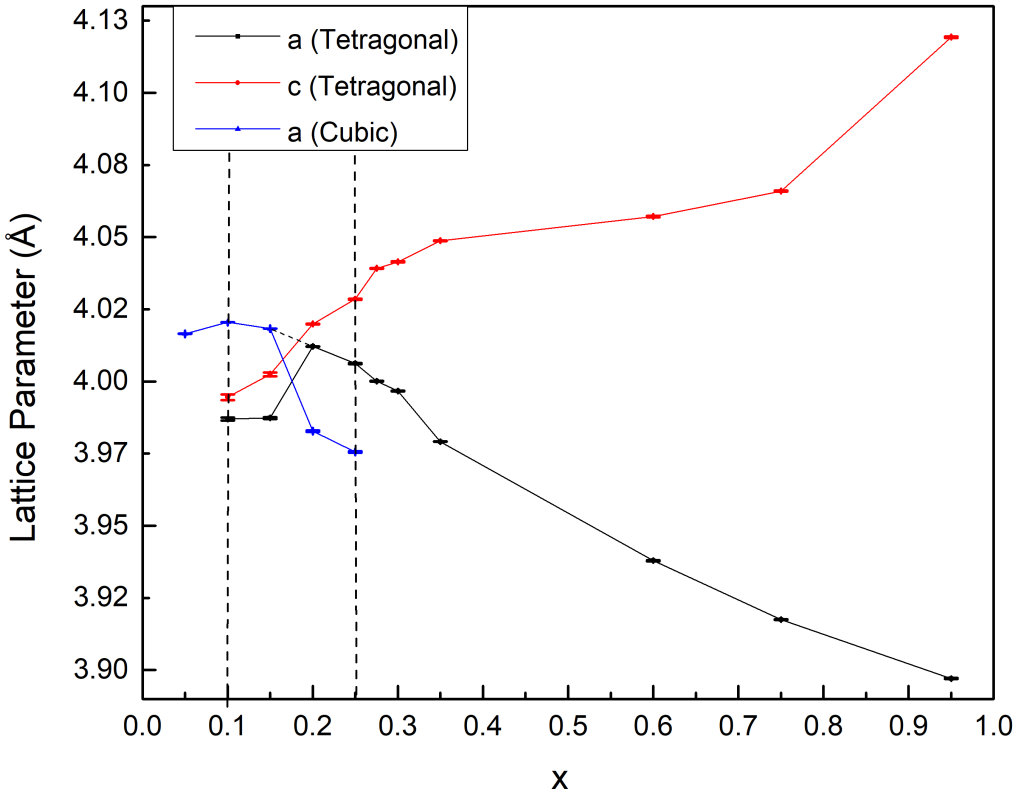

Figure 3.13 Variations of the lattice parameter *a* and *c* for both the cubic and tetragonal phases as a function of composition in the (1-x)($Pb_{0.5}Sr_{0.5}$)($Zr_{0.5}Ti_{0.5}$)O_3 – x$PbTiO_3$ (x = 0.05, 0.10, 0.15, 0.20, 0.25, 0.275, 0.35, 0.30, 0.60, 0.75 and 0.95) solid solution. The vertical dashed lines indicate the intermediate region (x = 0.10 ~ 0.25).

The calculated volume and tetragonality (*c*/*a*) of the unit cell as a function of composition x are shown in Figure 3.14. Similar to the variations of lattice parameters, the lattice volumes of the cubic ($x < 0.20$) and tetragonal ($x \geq 0.20$) phases show continuous trends. In the former case, the volume of the unit cell increases first as x increases up to 0.10, and then decreases with further increase of x, which can be explained by the ionic radius of A-site and B-site cations. In the PSZT-PT perovskite solid solution system, Pb^{2+} ion has a slightly larger ionic radius (1.49 Å) than Sr^{2+} ion (1.44 Å), which should give rise to an enlarged unit cell. However, Ti^{4+} ion has a smaller ionic radius (0.61 Å) than Zr^{4+} ion (0.72 Å), which should lead to a decrease in the volume of unit cell. The overall variation of the lattice volume is the competing result of these two effects. At low PT concentrations, the effects of Pb^{2+} substitution seems to be dominant, leading to an increase in the volume for x up to 0.10, but at higher PT contents, the effects of the smaller Ti^{4+} ion prevail, giving rise to a continued decrease of the volume with further increase of $PbTiO_3$, which is consistent with the observed peak shifting in the XRD patterns (Fig. 3.6).

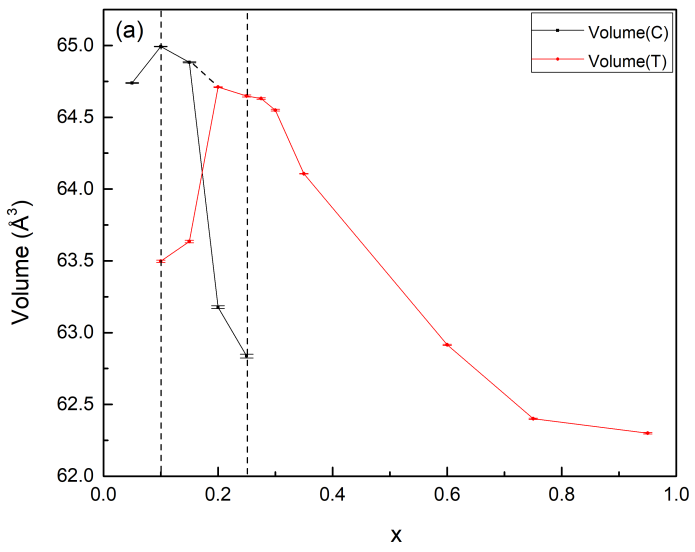

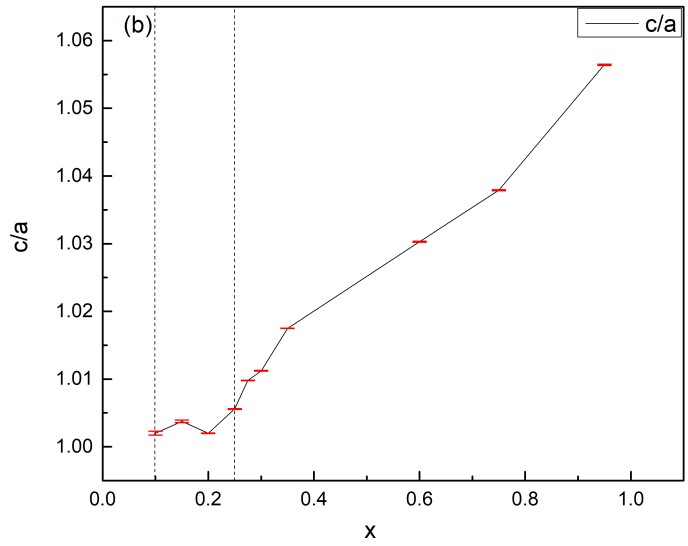

Figure 3.14 (a) The calculated volume and (b) tetragonality (*c*/*a*) of the unit cell as a function of composition x in the (1-x)($Pb_{0.5}Sr_{0.5}$)($Zr_{0.5}Ti_{0.5}$)O_3 – x$PbTiO_3$ (x = 0.05, 0.10, 0.15, 0.20, 0.25, 0.275, 0.30, 0.35, 0.60, 0.75 and 0.95) solid solution. The vertical dashed lines indicate the intermediate region (x = 0.10 ~ 0.25).

In Figure 3.14 (b), an increasing trend for the tetragonality (*c*/*a*) can be observed for $x \geq 0.20$, which indicates that the symmetry of the solid solution is gradually distorted to be more tetragonal with the increase of $PbTiO_3$ concentration. The *c*/*a* ratio and associated structural distortion are usually related to the appearance of spontaneous polarization and ferroelectricity. In the intermediate composition region of x from 0.10 to 0.20, the tetragonality is only slightly above 1.0, indicating the onset of the tetragonal phase.

3.5. Conclusions

A novel pseudo-binary solid solution of (1-x)($Pb_{0.5}Sr_{0.5}$)($Zr_{0.5}Ti_{0.5}$)O_3-x$PbTiO_3$ (PSZT-PT) of complex perovskite structure has been successfully synthesized by the solid state reaction method. The solid solution system shows a continued solubility. All the compositions are synthesized in form of ceramics by calcination at the temperature of 950°C, followed by sintering in the temperature range from 1175 to 1275 °C, depending on composition: as the concentration of $PbTiO_3$ increases, the sintering temperature of

the ceramics decreases because the melting points of PbO and TiO_2 are lower than those of SrO and ZrO_2.

The phase components and crystal structure of the new solid solution has been investigated by X-ray diffraction. The refinement results of the experimental data by GSAS II academic software reveal that the structure of the $(1-x)(Pb_{0.5}Sr_{0.5})(Zr_{0.5}Ti_{0.5})O_3$-$xPbTiO_3$ system gradually transforms from a centrosymmetric, nonpolar, cubic phase (*Pm-3m*) into a non-centrosymmetric, polar, tetragonal phase (*P4mm*) with the increase of PT content. The phase transformation occurs within the intermediate composition region of x = 0.10 – 0.25, where the tetragonal phase forms alongside the initial cubic phase in x = 0.10, and becomes dominant in the mixed phases when $x \geq 0.175$. The tetragonal phase eventually takes over the cubic phase completely when $x \geq 0.275$. As x increases, the lattice parameter *a* shows a general increasing trend and the lattice parameter *c* exhibits a general decreasing trend. A crossover of the lattice parameter *a* between the cubic and tetragonal phases occurs at x = 0.175, consistent with the crossover of the fractions of the respective phases. With the increase of the PT concentration, the tetragonality is found to increase, which indicates an enhancement of lattice distortion towards the tetragonal structure. The volume of unit cell has a general descending trend with increasing x.

The successful synthesis of the $(1-x)(Pb_{0.5}Sr_{0.5})(Zr_{0.5}Ti_{0.5})O_3$-$xPbTiO_3$ system has brought about a new pseudo-binary solid solution from the $SrTiO_3$-$PbTiO_3$-$PbZrO_3$ ternary system. The structural crossover from the cubic to tetragonal phase found in this solid solution system suggests possible crossovers of physical properties, in particular, the crossover from relaxor ferroelectric behaviour to normal ferroelectric phase, which will be investigated in terms of dielectric and ferroelectric properties and domain structures of nano- to microscale. These studies will be described in **Chapter 4**.

Chapter 4.

Characterization of the Electrical Properties and Domain Structures of the $(1-x)(Pb_{0.5}Sr_{0.5})(Zr_{0.5}Ti_{0.5})O_3$-$xPbTiO_3$ Solid Solution: Crossover from Relaxor to Ferroelectric

4.1. Abstract

The dielectric properties of the novel $(1-x)(Pb_{0.5}Sr_{0.5})(Zr_{0.5}Ti_{0.5})O_3$-$xPbTiO_3$ (PSZT-PT) solid solution were studied by measuring the dielectric permittivity as a function of temperature at various frequencies. For the composition of x = 0.05, the temperature dependence of dielectric constant shows a relaxor behaviour with a broad and frequency dependent dielectric anomaly. For the compositions of x = 0.10 ~ 0.25, a crossover from the relaxor behaviour to normal ferroelectricity was observed, accompanied by double peaks on the dielectric permittivity. For $x \geqslant 0.275$, the dielectric peaks become sharper and show no frequency dispersion, indicating a normal ferroelectric phase. In addition, the Curie temperature (T_C) of the PSZT-PT samples shifts towards higher temperatures as x increases. Interestingly, the room-temperature dielectric constant of PSZT is greatly increased by the substitution of PT, reaching 3,032 for x = 0.20 (at 1 kHz), making this material a new candidate for multilayered ceramic capacitors. The dielectric data of the PSZT-PT solid solution samples were fitted with various formalisms and equations to obtain critical parameters, such as the freezing temperature, the Burns temperature, etc., to characterize the relaxor behaviour. Moreover, domains of nanometer size were revealed by transmission electron microscopy (TEM) in the relaxor phase, which are assigned as the polar nanoregions. These domains grow into macroscopic domains in the ferroelectric domain. Finally, the polarization - electric field relation transforms from a narrow nonlinear shape to a wide-open hysteresis loop with increasing remanent polarization and coercive field, confirming the crossover from the relaxor state to ferroelectric phase with increasing PT concentration in the PSZT-PT binary system. The mechanisms of the crossover is explained in terms of chemical and polar order/disorder, crystal structure and domain size based on crystal chemistry considerations.

4.2. Introduction

As one of the well-known functional materials families, ferroelectric materials are used in various technological fields such energy storage devices and memory devices, thanks to their peculiar dielectric and ferroelectric properties [3]. As the first discovered ferroelectric material, Barium Titanate $BaTiO_3$, has been investigated for decades and used in a wide range of fields such as piezoelectric actuators transducers [95], [96] and high-dielectric-constant multilayer ceramic capacitors (MLCC) [96]. Since 1954, $Pb(Ti_{1-x}Zr_x)O_3$ (PZT) ceramics have been widely used in devices such as sensor and actuator owning to its outstanding dielectric and piezoelectric properties [97]. In addition, the dielectric and ferroelectric performance of PZT was further modified and improved by doping a small concentration of other ion(s) into PZT. Until now, a variety of PZT based materials still play a significant role in the applications of ferroelectric materials. However, PZT suffers from such inherent drawbacks as lead toxicity and brittleness [98]. Recently, $SrTiO_3$ attracts a great deal of interests as a lead-free material, due to its high dielectric constant at low temperatures [54], [99]. By induction of $SrTiO_3$ into the well-known PZT system, a ternary system consisting of $SrTiO_3$-$PbTiO_3$-$PbZrO_3$ (ST-PT-PZ) can be formed. However, little is known so far as to the structures and the electric properties of this ST-PT-PZ ternary system. The investigation of the properties of materials in this ternary system can provide us with more options of relaxor-based functional materials.

Relaxor materials are a class of disordered crystals possessing peculiar structures and properties [4]. Because of their outstanding performance in dielectric properties, these materials are considered as good candidates for applications such as multi-layer energy storage capacitors and high-performance piezoelectric devices [100]. For the canonical relaxor materials, e.g. $Pb(Mg_{1/3}Nb_{2/3})O_3$, a broad and frequency-dependent diffuse peak can be observed in the dependence of dielectric constant (ε) versus temperature (T), with the temperature of dielectric maximum, which is defined as T_{max}, shifting towards higher temperatures with the increase of frequency. The random arrangement of various ions among the crystallographically equivalent lattice sites in relaxors leads to the compositional disorder, which is the common feature of relaxor materials [12]. Due to the chemical and polar disorders, the polar domains in relaxors have a much smaller size compared to the macro-domains in normal ferroelectric, and they are known as the polar nanoregions (PNRs) [25]. Upon cooling, the relaxor materials transform from the

paraelectric into an ergodic relaxor phase. This transition temperature is defined as the Burns temperature (T_B), at which the temperature-dependent dielectric permittivity starts to deviate from the Curie-Weiss law. Upon further cooling in the ergodic relaxor state, the size of PNRs gradually increases, and the dynamics of dipole fluctuations decreases. Below the temperature T_f, which is defined as the freezing temperature [12], the relaxor is in a non-ergodic phase, where the PNRs become static and completely frozen with an infinite relaxation time [12]. In the canonical relaxors, a slim hysteresis loop with non-zero remanent polarization $P_r \neq 0$ at $T > T_{max}$ can usually be observed, which is a typical behaviour of ferroelectric relaxor and clearly signifies the existence of PNRs [30], [101]. Since the size of the PNRs is much smaller than the domains in normal ferroelectrics, the PNRs response to the external field much faster and more frequently than the domains in a normal ferroelectric do, leading to a slim and nonlinear hysteresis loop [84].

By substituting Sr^{2+} for Pb^{2+} on the A-sites of PZT, solid solution of strontium lead zirconate titanate (PSZT) can be obtained, which exhibits the relaxor behaviour originating from the chemical disorder of the A site cations Sr^{2+} and Pb^{2+}. The previous works on PSZT binary system has found some interesting properties such as good dielectric performance at low temperature as shown in the Figure 4.1 [76]. However, the T_{max} of PSZT samples with good dielectric permittivity are too low to allow the applications of materials in various devices. By substituting lead titanate $PbTiO_3$ (PT) into PSZT, it is possible to obtain relaxor ferroelectrics with higher T_{max} because of the high T_C of PT ($T_C \approx 490°C$). Based on this consideration, we have prepared the novel solid solution of PSZT-PT, and determined the crystal structures of the PSZT-PT system in Chapter 3. The refinement results of the experimental data by GSAS II academic software reveal that the structure of PSZT-PT system transforms from a centrosymmetric, nonpolar, cubic phase (*Pm-3m*) into a non-centrosymmetric, polar, tetragonal phase (*P4mm*) with the increase of PT content. The phase transformation occurs within the intermediate composition region of $x = 0.10 – 0.25$, where the tetragonal phase forms alongside the initial cubic phase in $x = 0.10$, and becomes dominant in the mixed phases when $x \geq 0.175$. The tetragonal phase eventually takes over the cubic phase completely when $x \geq 0.275$.

To better understand the mechanism behind the crossover between relaxor and ferroelectric in this system, electrical properties and domain structures of the PSZT-PT system need to be further studied. In this chapter, we investigate the dielectric and ferroelectric properties and domain states of the pseudo-binary solid solution of (1-

x)($Pb_{0.5}Sr_{0.5}$)($Zr_{0.5}Ti_{0.5}$)O_3-x$PbTiO_3$ (PSZT-PT) so as to characterize the physical properties as a function of composition . The results demonstrate the crossover from the relaxor state to the normal ferroelectric phase in terms of dielectric relaxation behaviour, polarization - electric field relation and polar domain structures.

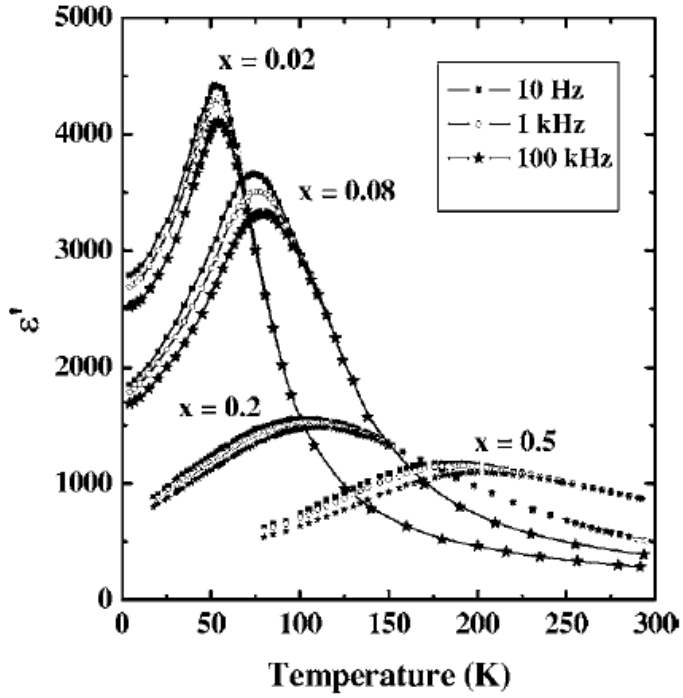

Figure 4.1 Temperature dependence of the real part of the dielectric permittivity (ε') in the (1−x)$SrTiO_3$-x$PbZrO_3$ solid solution measured at different frequencies. (adapted from Ref. [76])

4.3. Experimental

The ceramic pellets of the (1-x)($Pb_{0.5}Sr_{0.5}$)($Zr_{0.5}Ti_{0.5}$)O_3-x$PbTiO_3$ (PSZT-PT) solid solution (x = 0.05, 0.10, 0.15, 0.175, 0.20, 0.225, 0.25, 0.275, 0.30, 0.35, 0.50, 0.65, 0.75, 0.85 and 0.95) were synthesized and sintered according to the process described in Chapter 3, Sec. 3.3.1. The ceramics were polished to obtain flat and parallel surfaces by using silicon carbide sand papers with 400, 600 and 800 grits. The polished pellets were painted with silver paste on the circular surface and connected to gold wires as electrodes for electric measurements. The dielectric properties of prepared PSZT-PT samples were measured by means of a Novocontrol Alpha high resolution broadband dielectric spectrometer as a function of temperature at different frequencies. The dielectric constant

and loss tangent data were measured with a temperature interval of 1 degree after stabilization. The results of the measurements were used for the analysis of dielectric properties and phase transition behaviours in the PSZT-PT solid solution.

After the dielectric measurements, the samples with gold wires attached were connected to a ferroelectric test system (RT66A Standard Ferroelectric testing system, Radiant Technologies Inc.) to measure the polarization as a function of applied bipolar electric field.

Transmission electron microscopy (TEM) was used to study the surface morphology and domain structure and size of the PSZT-PT ceramic samples. The procedure of TEM specimen preparation is illustrated in Figure 4.2 below. The ceramic pellet was firstly hand polished using various silicon carbide sand papers to reduce the thickness down to approximately 100 μm. Then the thinned sample was cut into small circular discs with a diameter of 3 mm by an ultrasonic disk cutter (Model 330, E.A. Fischione Instrument Inc.). After the circular disc was obtained, dimple grinding was performed on the sample disc and the central part of the pellet was ground to a thickness of about 20 μm using a dimpler (Model 150 Specimen Prep System, E.A. Fischione Instrument Inc.). Lastly, the disc specimen was placed in an ion milling machine (Model 1010, Low Angle Ion Milling & Polishing System, E.A. Fischione Instrument Inc.) and ion-milled for 10 hours to obtain a thickness of ~ 50 nm at the central part of the specimen. The processed specimen was characterized by transmission electron microscopy (TEM, Hitachi 8100) to study the microstructure.

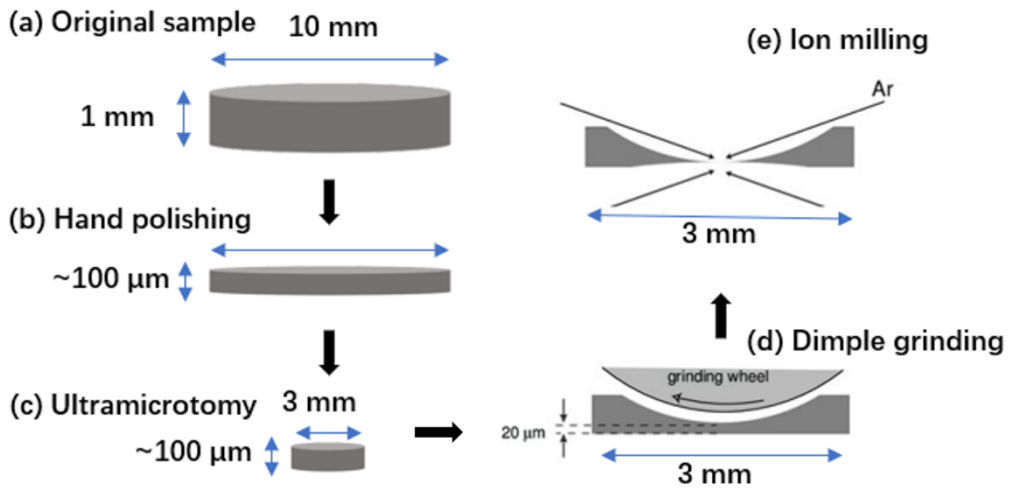

Figure 4.2 Illustration of sample preparation process for the TEM characterization.

4.4. Results and Discussion

4.4.1. Dielectric Properties

The variations of the real part of dielectric permittivity (ε') and dielectric loss (tan δ), of the (1-x)($Pb_{0.5}Sr_{0.5}$)($Zr_{0.5}Ti_{0.5}$)O_3-x$PbTiO_3$ solid solution with compositions x = 0.05 and 0.10, as a function of temperature measured at various frequencies from 10 Hz to 1 MHz, are shown in Figure 4.3. The dielectric permittivity data shows a broad and diffuse peak with significant frequency dispersion (Figure 4.3 (a, c)). The frequency dispersion is characterized by the temperature of dielectric maximum (T_{max}), which increases with increasing frequency, indicating a typical relaxor behaviour [12] for these two compositions. The difference between the T_{max} values at two different frequencies (ΔT_{max}) is typically used to measure the degree of relaxor behaviour, e.g. ΔT_{max} (1 kHz and 100 kHz) = T_{max} (100 kHz) - T_{max} (1 kHz) = 11 °C for x = 0.05, which decreases to 9 °C for x = 0.10. The dielectric loss (tan δ) also exhibits frequency dispersion (Figure 4.3(b, d)), characteristic of relaxor behaviour [12] (the increased loss at high temperatures and low frequencies is due to mobile charges). More detailed analyses of the relaxor behaviour and related parameters are presented in Sections 4.4.2 & 4.4.3 in terms of Vogel-Fulcher law and Curie-Weiss law, respectively.

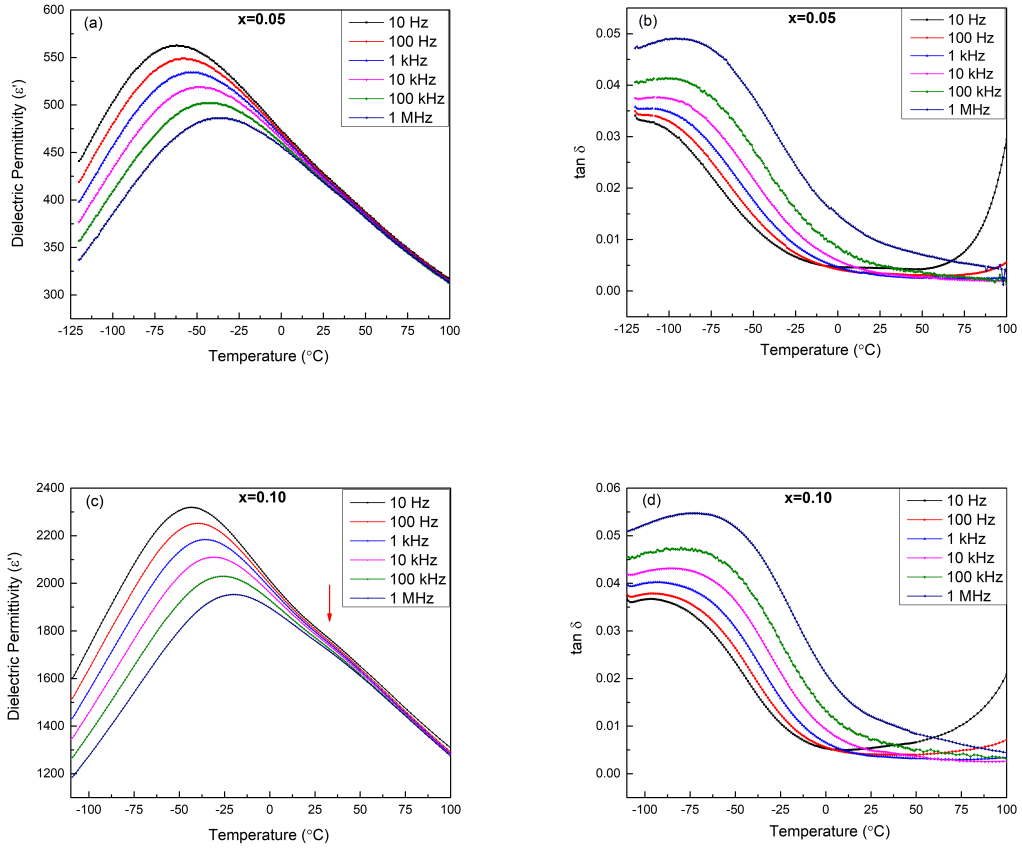

Figure 4.3 Variations of the dielectric permittivity (ε', (a, c)) and dielectric loss (tan δ, (b, d)) measured as a function of temperature at various frequencies from 10 Hz to 1 MHz for the (1-x)$Pb_{0.5}Sr_{0.5}Zr_{0.5}Ti_{0.5}O_3$-x$PbTiO_3$ solid solutions with compositions of x = 0.05 (a,b) and 0.10 (c, d), showing typical relaxor behaviour.

It is worth noting that for the composition of x = 0.10, in addition to the broad, diffuse and dispersive dielectric peak characteristic of relaxor behaviour, a small shoulder appears around 20 °C, marked by red arrow on the graph in Figure 4.3 (c), which is approximately 55 degrees above the T_{max}. As discussed below, this peak becomes more significant with increase PT concentration.

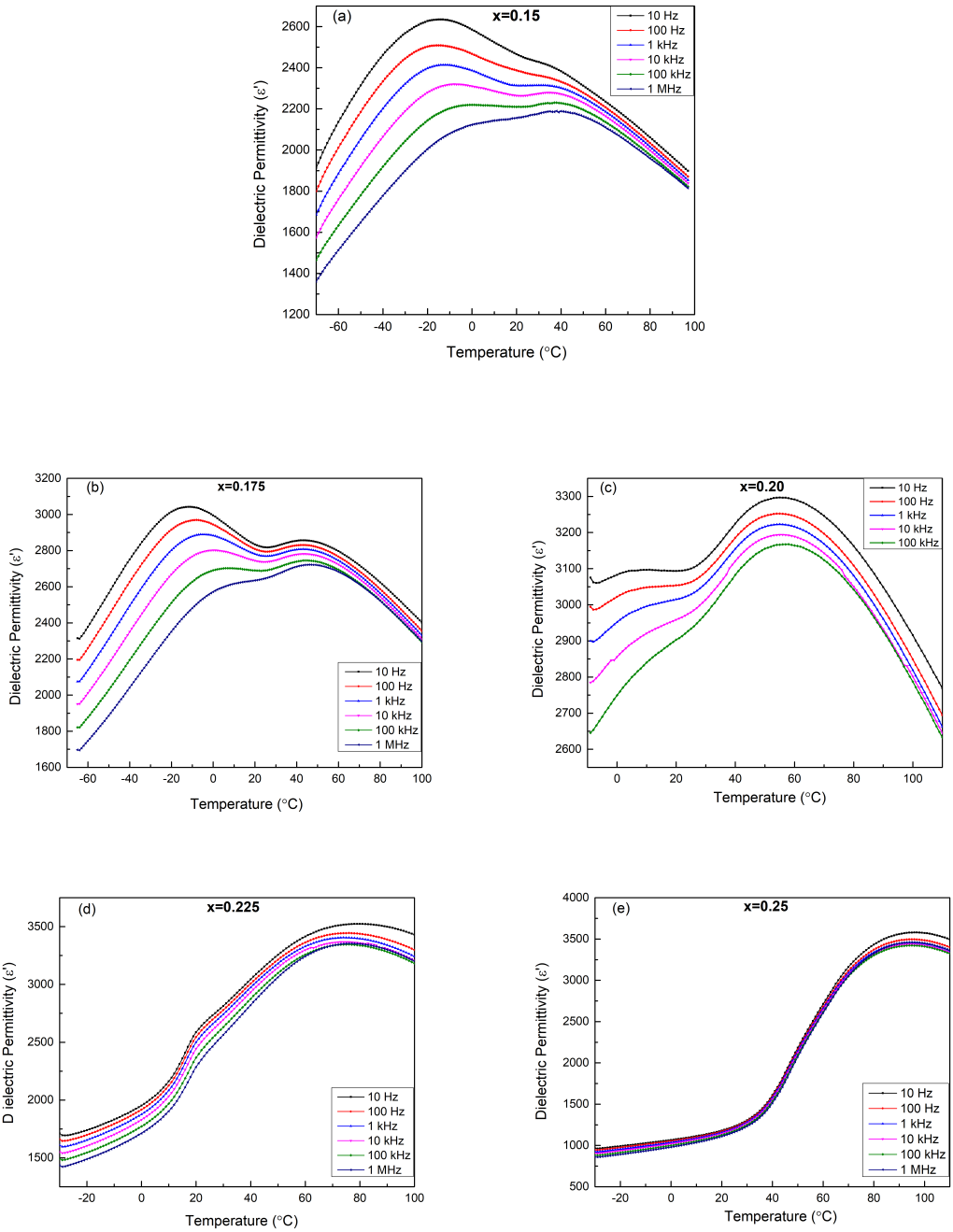

Figure 4.4 Variations of the dielectric permittivity (ε') as a function of temperature measured at various frequencies for (1-x) $(Pb_{0.5}Sr_{0.5})(Zr_{0.5}Ti_{0.5})O_3$-x$PbTiO_3$ (x = 0.15 (a), 0.175 (b), 0.20 (c), 0.225 (d), and 0.25 (e)).

Figure 4.4 shows the variation of the dielectric permittivity (ε') as a function of temperature of the (1-x)$(Pb_{0.5}Sr_{0.5})(Zr_{0.5}Ti_{0.5})O_3$-x$PbTiO_3$ solid solution ceramics with the

compositions of x = 0.15, 0.175, 0.20, 0.225, and 0.25, measured at various frequencies. First, let us examine the evolution of the relaxor peak with composition. It can be seen that as the concentration of PT (x) increases from 0.05 to 0.10 (Figure 4.3), and then to 0.25 (Figure 4.4), the ΔT_{max} between the frequencies of 1 kHz and 100 kHz deceases from 11 °C to 9 °C, and then to 0 °C, while the T_{max} values at all the frequencies shift towards higher temperatures. This decrease in the ΔT_{max} value indicates the relaxor behaviour is weakened with the increasing substitution of PT for PSZT.

At the same time, the initial dielectric shoulder above T_{max} in x = 0.10 (Figure 4.3 (c)) gradually grows into a more and more clear peak in the samples with x = 0.15 and 0.175 (Figure 4.4 (a) and (b)). The temperature at which this secondary peak appears does not show frequency dispersion, as opposed to the dispersive peak at T_{max}, suggesting that this peak possible arises from a structural phase transition rather than a dielectric relaxation like the one at T_{max}. The relative magnitude and sharpness of this peak, as compared with the dispersive peak at T_{max}, continue to increase with further increase of x, and at x = 0.20 (Figure 4.4 (c)), it has developed into the major peak, whereas the initial peak at T_{max} becomes weaker and weaker, and has turned into a secondary anomaly (shoulder) in x = 0.225 (Figure 4.4 (d)) with a significant attenuation in its frequency dispersion. For the composition of x = 0.25, the secondary anomaly has almost disappeared and only one frequency-independent dielectric peak appears at 95 °C, and the dielectric dispersion has been further attenuated, as shown in Figure 4.4 (e).

Figure 4.5 illustrates the variation of ΔT_{max} (1 kHz and 100 kHz) and T_{max} (1 kHz) as a function of composition (x) for the $(1-x)(Pb_{0.5}Sr_{0.5})(Zr_{0.5}Ti_{0.5})O_3$-$xPbTiO_3$ samples. With the increasing x, ΔT_{max} decreases and T_{max} increases, indicating the relaxor behaviour in PSZT-PT samples is weakened and gradually disappears. As a result, the dispersive dielectric peak at T_{max} becomes narrower and less frequency dependent as x increases, and eventually disappears in x = 0.25.

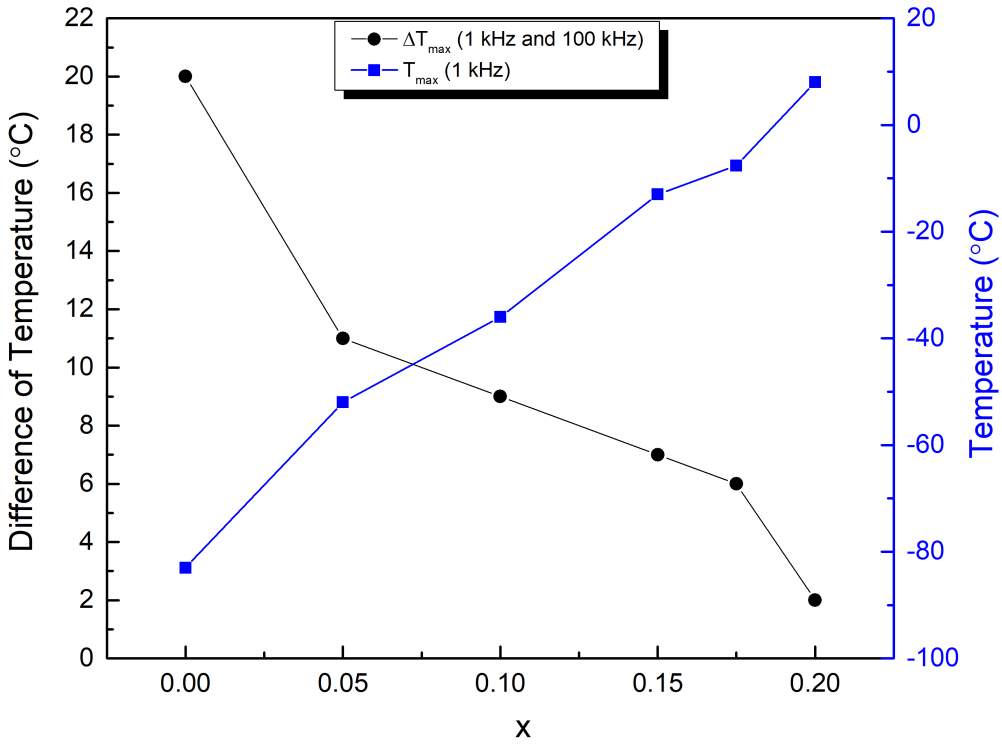

Figure 4.5 **Variations of the temperature of dielectric maxima, T_{max} (1 kHz) and the frequency dispersion ΔT_{max} (1 kHz and 100 kHz) as a function of composition for the (1-x)($Pb_{0.5}Sr_{0.5}$)($Zr_{0.5}Ti_{0.5}$)O_3-x$PbTiO_3$ solid solutions (x = 0, 0.05, 0.10, 0.15, 0.175 and 0.20). The data for the composition x = 0 is adapted from Ref. [76].**

Thus, the phenomenon of double peaks in the temperature dependence of dielectric constant is observed in the composition region from x = 0.10 to 0.25. In this composition range, the frequency dependent relaxation peak, which is characteristic of relaxor behaviour, becomes attenuated and eventually disappears, indicating weakening of the relaxor behaviour with the increase of PT concentration. Simultaneously, an additional anomaly develops into a major peak whose temperature is independent of frequency, suggesting a structural phase transition from a ferroelectric phase to a paraelectric phase. The weakening and disappearance of the relaxor state and the appearance of the ferroelectric phase can be attributed to the effect of the substitution of $PbTiO_3$ (PT), which favours the establishment of long-range ferroelectric phase with tetragonal symmetry. With the increasing substitution of PT for PSZT, the normal ferroelectric phase and tetragonal symmetry are introduced and enhanced in the solid solution system at the expenses of the initial relaxor phase. Therefore, the dielectric properties reveal a crossover from typical relaxor behaviour in x =0.05 to a ferroelectric

state in x = 0.25, with the transformation taking place in the intermediate region of x = 0.10 to 0.225 (more evidence of ferroelectricity will be presented in Sec. 4.4.5).

The dielectric properties of the compositions with higher PT concentrations are also characterized. Figure 4.6 shows the temperature dependent dielectric permittivity (ε') measured at different frequencies for the compositions of x = 0.275 (a) and 0.65 (b). It can be seen that a frequency-independent dielectric peak appears in x = 0.275, indicating a normal ferroelectric behaviour. With further increase of PT contents, the dielectric peak becomes sharper, and the dielectric maximal value increases, indicating an enhancement of the ferroelectric behaviour in the samples. The temperature of the dielectric maxima is considered as the Curie temperature (T_C) at which the phase transition from ferroelectric to paraelectric phase takes place upon heating.

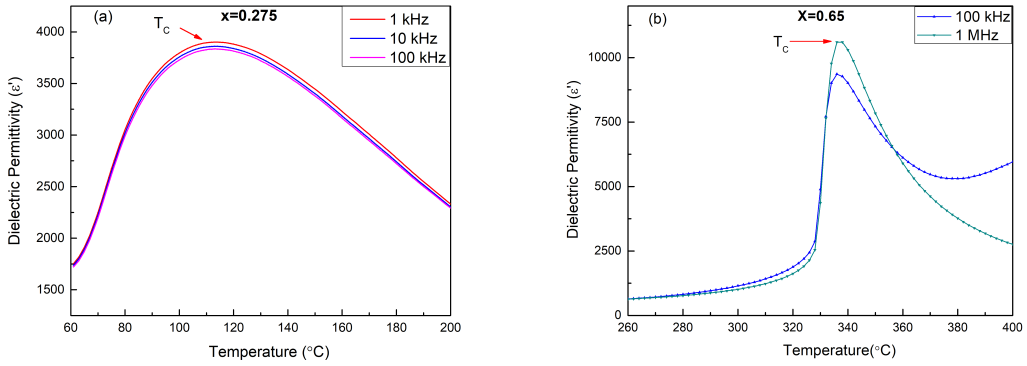

Figure 4.6 Variation of the dielectric permittivity (ε') as a function of temperature measured at various frequencies for the (1-x)($Pb_{0.5}Sr_{0.5}$)($Zr_{0.5}Ti_{0.5}$)O_3-x$PbTiO_3$ solid solutions with x = 0.275 (a) and 0.65 (b)).

The Curie temperatures T_C of the solid solution with different compositions of x varying from 0.275 to 1.0 are shown in Table 4.1. As x increases, the T_C of the PSZT-PT samples increases, confirming the enhanced ferroelectric state induced by the PT substitution.

Table 4.1 The ferroelectric Curie temperatures T_C of the different compositions of the (1-x)($Pb_{0.5}Sr_{0.5}$)($Zr_{0.5}Ti_{0.5}$)O_3-x$PbTiO_3$ solid solution.

x	0.275	0.3	0.35	0.5	0.65	0.75	0.85	0.95	1.0
T_C (°C)	113	132	172	262	340	384	420	470	490

Overall, for the composition of x = 0.05, the dielectric properties indicate typical relaxor behaviour. For the compositions of x from 0.10 to 0.25, a crossover from relaxor to normal ferroelectric can be observed in this transition range. For x larger than 0.275, the solid solutions of PSZT-PT exhibit the normal ferroelectric phase. The relaxor behaviour, the ferroelectric properties, and the micro-structure of the PSZT-PT system are further characterized in the following sections.

Another important parameter is the value of the real part of dielectric permittivity, i.e. dielectric constant (ε'), at room temperature, which determines the potential of the material for applications as high capacitance capacitors. Figure 4.7 shows the variation of the room-temperature (25 °C) dielectric constant measured at 1 kHz for the solid solutions of $(Pb_{0.5}Sr_{0.5})(Zr_{0.5}Ti_{0.5})O_3$-$xPbTiO_3$ with compositions of x = 0, 0.05, 0.10, 0.15, 0.175, 0.20, 0.225, and 0.25. It can be seen that the dielectric constant value increases with increasing concentration of PT and reaches a maximum value of 3,032 with the composition of x = 0.20. This value is more than 3 times that of PSZT [76], making the 0.80PSZT-0.20PT solid solution an excellent material for the fabrication of multilayered ceramic capacitors.

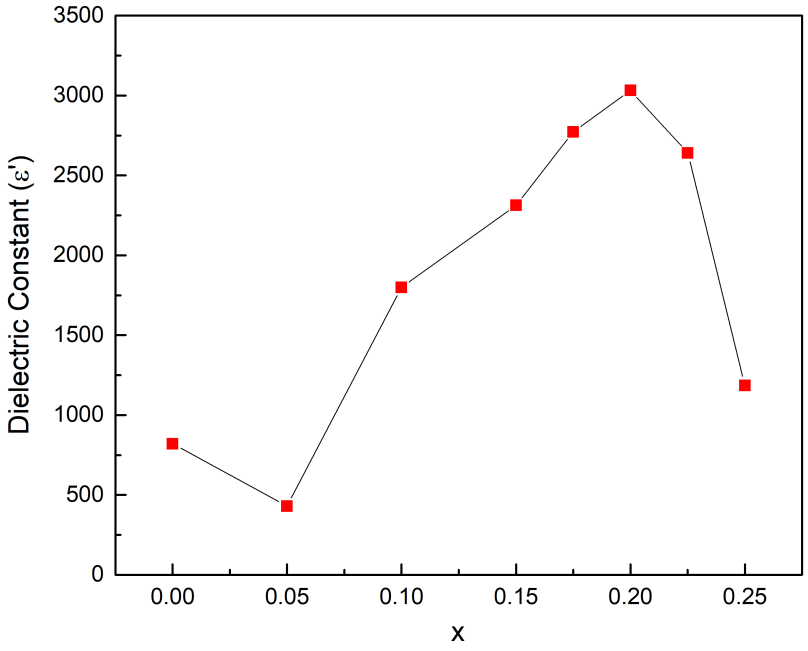

Figure 4.7 **The variation of the room-temperature (25 °C) dielectric constant measured at 1 kHz for the solid solutions of $(Pb_{0.5}Sr_{0.5})(Zr_{0.5}Ti_{0.5})O_3$-$xPbTiO_3$ with compositions of x = 0, 0.05, 0.10, 0.15, 0.175, 0.20, 0.225, and 0.25.**

4.4.2. Vogel-Fulcher Law Analysis

For compositions with relaxor behaviour, the frequency dependence of the dielectric maximum temperature T_{max} can be expressed by the Vogel-Fulcher (VF) law, which is a remarkable feature for relaxor materials [12]:

$$f = f_0 \exp[-\frac{E_a}{k_B(T_{max} - T_f)}] \ , \qquad \text{(Eq. 4.1)}$$

where f_0 is the Debye frequency, E_a is the activation energy, k_B is the Boltzmann constant, T_{max} indicates the temperature of the permittivity maximum, and T_f is the static freezing temperature where the relaxation time becomes infinite and polar nanoregions (PNRs) become frozen [26]–[28]. The fitting results of the sample with the composition of x = 0.05 are shown in Figure 4.8 in terms of the reciprocal of the difference between $\ln f_0$ and $\ln f$ versus temperature. It can be seen that the experimental data T_{max} at various frequencies fit the model of the VF law well with a linearity close to 1, indicating typical relaxor ferroelectric behaviour. An activation energy (E_a) of 0.0605 eV is obtained, which is the energy required to overcome the energy barrier for the reorientation of the polarization

between the adjacent orientation states during the relaxation [22]. Furthermore, the value of f_0 is found to be as 5.87 × 10^{11} Hz, which is the reciprocal of the relaxation time, indicating the frequency of thermal activated reorientation of dipoles [12]. The freezing temperature (T_f) of the sample is -91.3 °C, below which the PNRs become frozen and the relaxation time becomes infinite [12].

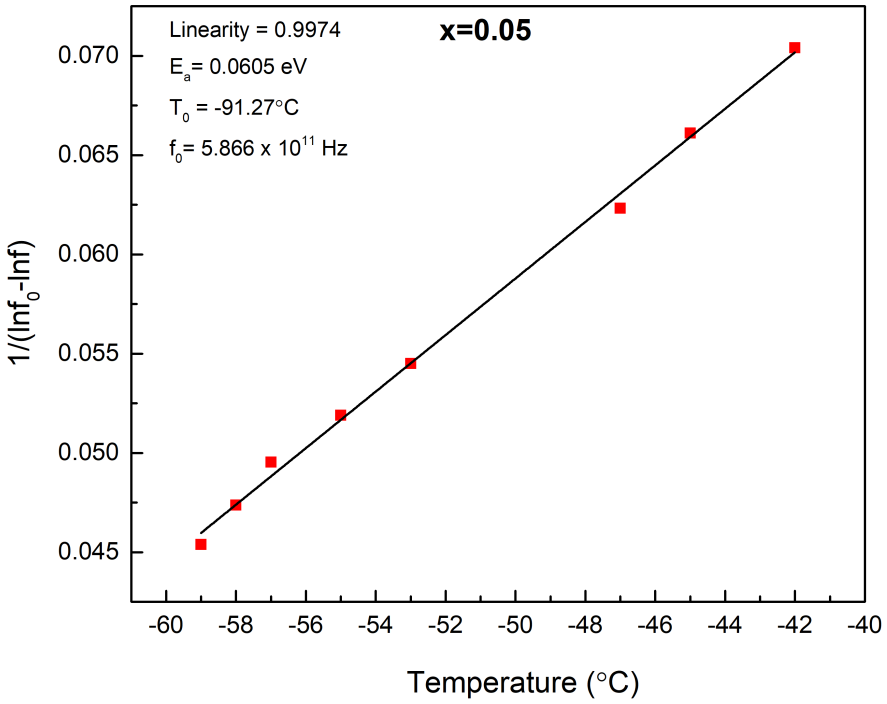

Figure 4.8 Correlation between 1/(lnf_0-ln$f$) and temperature for the (1-x) $Pb_{0.5}Sr_{0.5}Zr_{0.5}Ti_{0.5}O_3$-x$PbTiO_3$ ceramic sample with x = 0.05. The black line represents the linear fitting of experimental data to the Vogel-Fulcher (VF) law, indicating typical relaxor behaviour.

For the other compositions of x = 0.10, 0.15 and 0.175, similar fitting process is performed and the experimental data of the relaxor peaks fit well the VF law. On the other hand, for the compositions of x = 0.20, 0.225 and 0.25, the VF fitting cannot be conducted properly since the ΔT_{max} values in these compositions are too small to carry out an accurate and meaningful fitting. The parameters of VF fitting performed in different relaxor samples are shown in Table 4.2. As the concentration of PT (x) becomes larger, the freezing temperature T_f of the corresponding compositions increases, which shows a similar trend with T_{max} (see Figure 4.5).

Table 4.2 **The freezing temperature (T_f), Debye frequency (f_0) and the activation energy (E_a) of VF fitting for the different compositions of the (1-x)($Pb_{0.5}Sr_{0.5}$)($Zr_{0.5}Ti_{0.5}$)O_3-x$PbTiO_3$ solid solution.**

x	0.05	0.10	0.15	0.175
T_f (°C)	-91.27	-67.91	-45.35	-36.64
f_0 (Hz)	5.87×10^{11}	7.32×10^{11}	5.62×10^{10}	1.28×10^{11}
E_a (eV)	0.0605	0.0777	0.0805	0.1016

The relationship between the activation energy (E_a) and composition x is shown in Figure 4.9. With increasing $PbTiO_3$ concentration x, the activation energy of the samples gradually increases. Since the activation energy needed for the reorientation of dipoles in adjacent domains is roughly proportional to the size of domains [30], [102], the increasing trend of the E_a parameter suggest that the size of the PNRs may become larger as the concentration of $PbTiO_3$ increases. The local domain structures investigated by transmission electron microscopy (TEM) support this deduction (see Sec. 4.4.5).

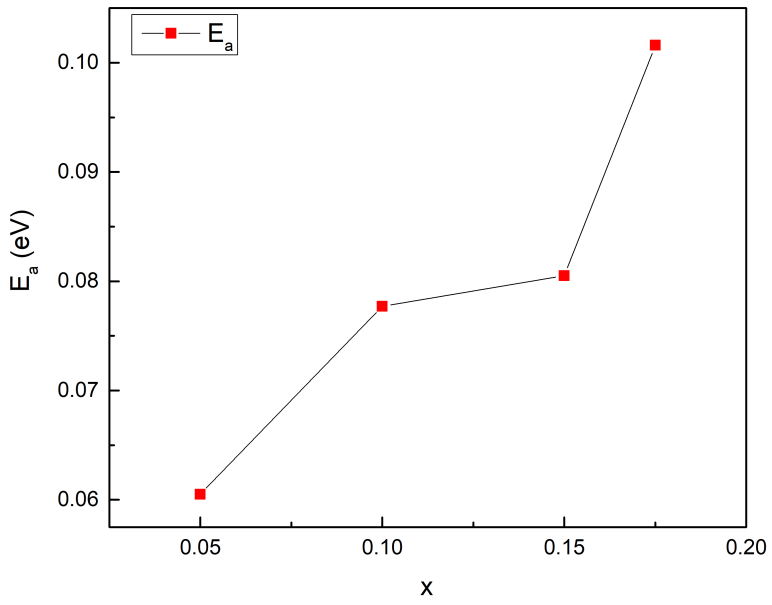

Figure 4.9 **Variation of the activation energy E_a from the VF fitting as a function of composition for the (1-x)($Pb_{0.5}Sr_{0.5}$)($Zr_{0.5}Ti_{0.5}$)O_3-x$PbTiO_3$ solid solution samples (x = 0.05, 0.10, 0.15, 0.175).**

4.4.3. Curie-Weiss Law Analysis

For normal ferroelectric, dielectric constant obeys the Curie-Weiss (CW) law (Eq. 4.2) in the paraelectric phase at high temperatures [102]:

$$\varepsilon' = \frac{C}{T - T_{cw}}, \qquad \text{(Eq. 4.2)}$$

where C is the Curie constant, T is the absolute temperature in Kelvin, T_{CW} is the Curie-Weiss temperature and ε' is the dielectric permittivity. The CW law can also be observed in relaxor ferroelectric when $T \geqslant T_B$ (the Burns temperature), which is usually higher than T_{max} [102]. The CW fitting results of the dielectric permittivity for the composition of x = 0.10 is shown in Figure 4.10 in terms of the reciprocal of dielectric permittivity (1/ ε', at 398 kHz) as a function of temperature. The fitting results indicates a Burns temperature (T_B) = 274.8 °C, below which the dielectric constant starts to deviate from the CW law [25], and a Curie -Weiss temperature (T_{cw}) = 67.9 °C, where the transition from the paraelectric to ferroelectric phase is supposed to occur upon cooling, but it is interrupted by the effects of polar nanoregions [103], [104], leading to the relaxor state instead.

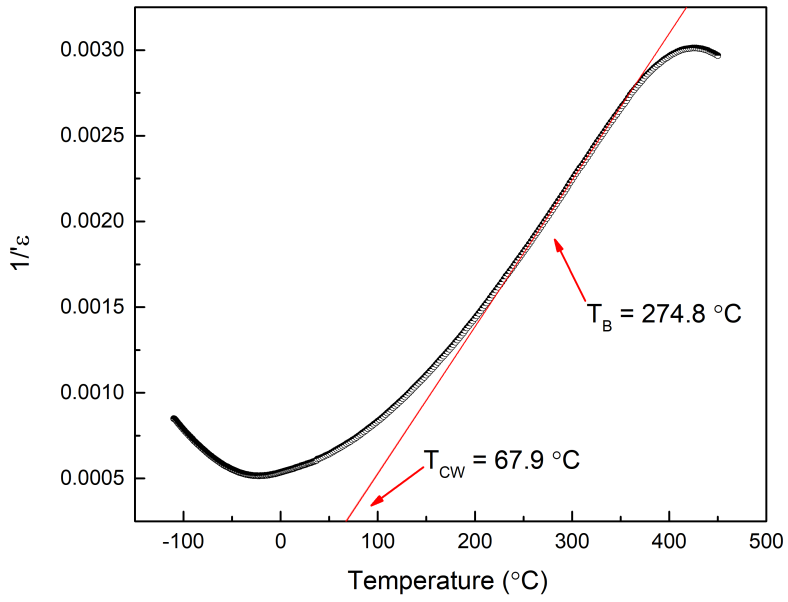

Figure 4.10 The reciprocal of dielectric constant (1/ε', at 398 kHz) as a function of temperature for the (1-x)($Pb_{0.5}Sr_{0.5}$)($Zr_{0.5}Ti_{0.5}$)O_3-x$PbTiO_3$ ceramic sample with x = 0.10. The red line represents the fitting to the Curie-Weiss (CW) law.

The corresponding residuals of the CW fitting as a function of temperature are shown in Figure 4.11. The Burns temperature was confirmed at the point where the residual of fitting becomes zero, indicating the onset point at which the dielectric behaviour of the sample begins to follow the CW law upon heating.

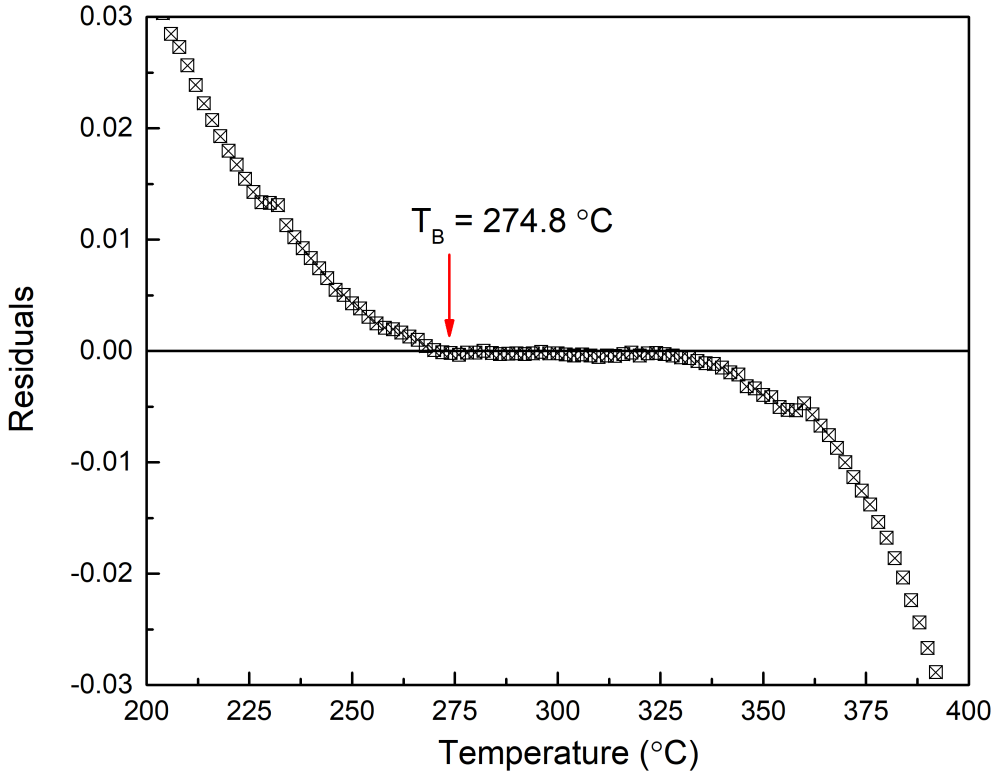

Figure 4.11 The residuals of the the CW fitting as a function of temperature for the ceramic sample of (1-x)($Pb_{0.5}Sr_{0.5}$)($Zr_{0.5}Ti_{0.5}$)O_3-x$PbTiO_3$ (x = 0.10).

Similar fitting is carried out on the samples with composition of x = 0.05, which also exhibits the relaxor behaviour. For compositions of higher lead titanate concentration (x = 0.15, 0.175, 0.20, 0.225 and 0.25), the fitting of CW law becomes less meaningful due to the influence of the increasing ferroelectric phase component, which leads to the overlapping of frequency dependent peak and frequency independent peak. The Burns temperature (T_B), the Curie Weiss temperature (T_{cw}) and temperature at dielectric maxima (T_{max}) of compositions of x = 0.05 and 0.10 are listed in Table 4.3 below. As x increases, T_B, T_{cw} and T_{max} all become higher.

Table 4.3 The Burns temperature (T_B), the Curie Weiss temperature (T_{cw}) and temperature at dielectric maxima (T_{max}) of Curie-Weiss (CW) fitting for x = 0.05 and 0.10 of the (1-x)($Pb_{0.5}Sr_{0.5}$)($Zr_{0.5}Ti_{0.5}$)O_3-x$PbTiO_3$ solid solution.

x	0.05	0.10
T_B (°C)	226.9	274.8
T_{CW} (°C)	-49.3	67.9
T_{max} (°C) (1 kHz)	-53.36	-35.25

4.4.4. Polarization - Electric Field Measurements

The polarization - electric field hysteresis (P-E) loops of the (1-x)($Pb_{0.5}Sr_{0.5}$)($Zr_{0.5}Ti_{0.5}$)O_3-x$PbTiO_3$ (PSZT-PT) solid solutions with x = 0.15 and 0.25 are measured at room temperature and the results are shown in Figure 4.13. For x = 0.15 (Figure 4.13(a)), the polarization (P) versus applied electric field (E) shows an almost linear correlation, which is considered as typical relaxor behaviour [18], [65], consistent with the dielectric properties of relaxor behaviour (Sec. 4.4.1) (only a very weak remanent polarization of 0.447 μC/cm^{-2} and a small coercive field of 1.14 kV/cm can be read). As x increases, the P-E loop opens up and displays hysteresis behaviour, typical of ferroelectricity. For instance, a broader and opened-up hysteresis loop is observed in the sample with composition of x = 0.25, as shown in Figure 4.13 (b). The remanent polarization of the sample is found to be 2.95 μC/cm^{-2} with a coercive field of 7.09 kV/cm, which indicate normal ferroelectric behaviour.

Therefore, the crossover from relaxor to normal ferroelectric phase in the PSZT-PT solid solution is clearly demonstrated by the polarization - electric field relations, with the remanent polarization and the coercive field increasing with the increase of the PT concentration, while the P-E relation transforming from a linear and slim loop of relaxor nature to a wide-open hysteresis loop characteristic of normal ferroelectricity.

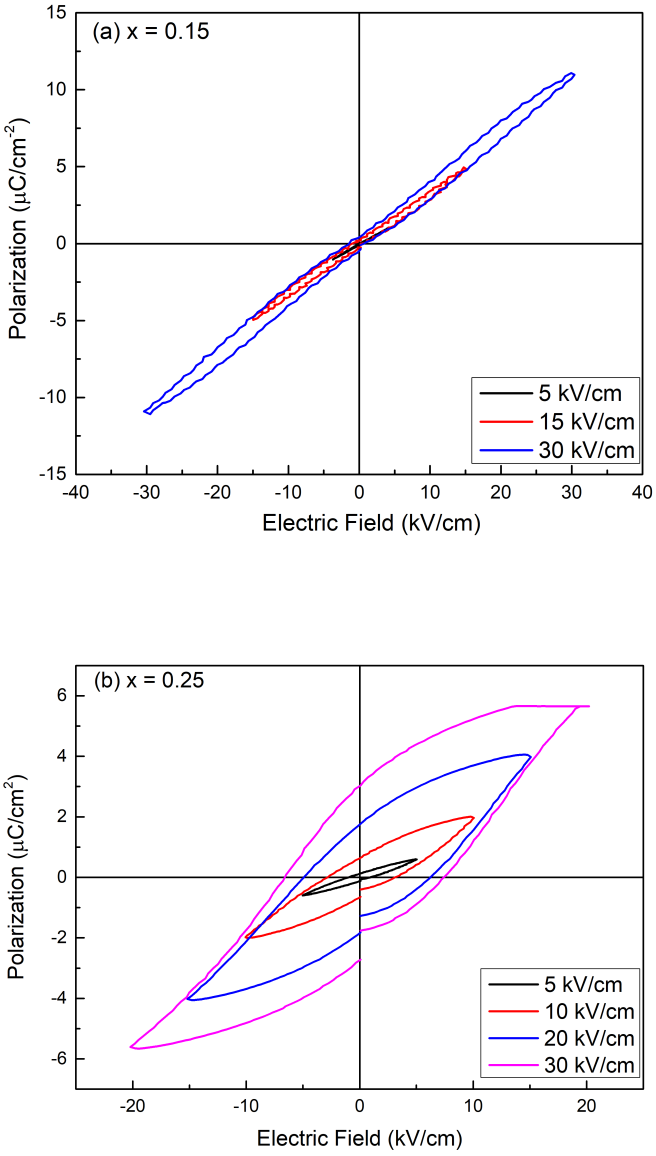

Figure 4.12 **The polarization - electric field (P-E) relations displayed for the (1-x)($Pb_{0.5}Sr_{0.5}$)($Zr_{0.5}Ti_{0.5}$)O_3-x$PbTiO_3$ (with x = 0.15 (a) and 0.25 (b)) ceramic samples measured at room temperature, showing an almost linear relation for x = 0.15, and a clear ferroelectric hysteresis loop for x = 0.25.**

4.4.5. Micro-structural Analysis

Transmission electron microscopy (TEM) is utilized to analyze the surface morphology and nano- to micro-domains in the (1-x) $(Pb_{0.5}Sr_{0.5})(Zr_{0.5}Ti_{0.5})O_3$-$xPbTiO_3$ (PSZT-PT) ceramics at room temperature. The bright field images of selected areas in the PSZT-PT ceramics with the compositions of x = 0.15 and 0.50 are shown in Figure 4.12(a) and (b), respectively, and the selected area electron diffraction (SAED) patterns are embedded in the corresponding bright field image as insets. For x = 0.15 (Figure 4.12(a)), a wavy-shaped fringe pattern is observed with an estimated size of 10 nm or smaller, which seems to correspond to the domains of polar nanoregions (PNRs) which are inherently present in a relaxor material [21]. The corresponding SAED pattern displays a zone axis of [111]. This nanodomain structure is consistent with the relaxor behaviour observed in this composition. For x = 0.50, the bright field image of selected area exhibits patterns of uniform wedge-shape domains oriented in mutually perpendicular directions (Figure 4.11(b)). The size of these domain is in the range of 0.1 to 0.2 μm, which is much larger than the ones in the sample with the composition of x = 0.15. This kind of domain structure is characteristic of a normal ferroelectric phase, consistent with the ferroelectric behaviour of the compound with x = 0.50 measured by dielectric properties (Sec. 4.4.1) and ferroelectric hysteresis loop (Sec. 4.4.4). The SAED pattern with a zone axis of [110] exhibits a complex diffraction patterns due to the different orientations of domains observed.

Thus, the imaging and analysis of the local structures by TEM reveal that the nano-domains in PSZT-PT samples with low PT contents become larger as the concentration of lead titanate increases. The bright field images directly display the morphologies of the PNRs and ferroelectric domains, which provides the crucial information on domain transformation from nano-scale to meso-to-macro-scale, accompanying the crossover from relaxor to normal ferroelectric properties.

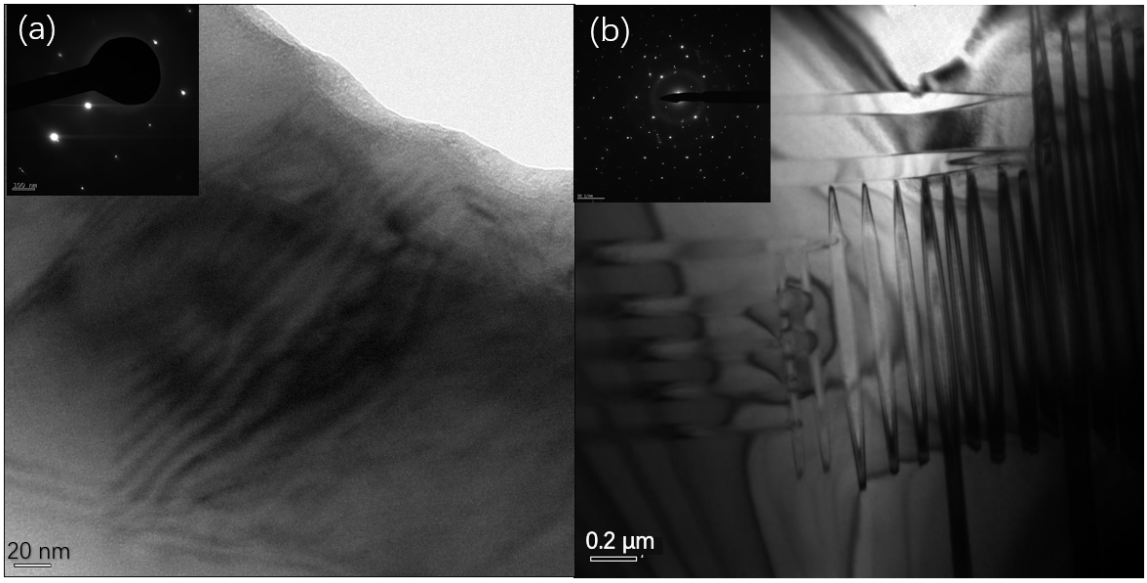

Figure 4.13 Nano-to-macro domain morphologies and micro-structures of (1-x)($Pb_{0.5}Sr_{0.5}$)($Zr_{0.5}Ti_{0.5}$)O_3-x$PbTiO_3$ (x = 0.15 (a) and 0.50 (b)) observed by TEM. Insets show the bright field images of selected area electron diffraction (SAED) patterns.

4.4.6. Crossover from Relaxor to Ferroelectric and Its Mechanisms

The systematic characterizations of the dielectric and ferroelectric properties presented in the previous sections have clearly demonstrated a crossover from the relaxor behaviour to a normal ferroelectric phase in the (1-x)($Pb_{0.5}Sr_{0.5}$)($Zr_{0.5}Ti_{0.5}$)O_3-x$PbTiO_3$ solid solution with the substituting concentration of lead titanate increasing from x = 0.05 to 0.25 and beyond. This crossover of the macroscopic properties is accompanied by evolution of domain structures from nanoscopic polar domains to meso- to macroscopic ferroelectric domains, as revealed by TEM.

This evolution of the dielectric properties and domain transformation, in particular, in the composition range of x = 0.10 to 0.25, can be explained from the crystal structural point of view by the results of the structural analysis presented in **Chapter 3**. It is found that the compositions of x = 0.10 to 0.25 contain a mixture of cubic and tetragonal phases, and phase fraction of the tetragonal phase increases, while the phase fraction of the cubic phase decreases, with the increase of PT contents (see Figure 3.12). The relaxor behaviour is typically associated with a (pseudo-)cubic phase [12], and the tetragonal phase is known to be of ferroelectric nature of lead titanate. Thus, the decreasing relaxor

behaviour observed from the dielectric properties is directly caused by the diminishing cubic phase component, while the emergence and growth of the second, frequency-independent dielectric peak results from the increasing tetragonal phase component. The disappearance of the relaxor behaviour corresponds to the vanishing of cubic phase and the full establishment of the tetragonal phase, which gives rise to the single dielectric without dispersion, corresponds to the phase transition from the induced tetragonal phase to the high-temperature paraelectric phase. Therefore, the structural crossover from cubic to tetragonal symmetry is well correlated with the dielectric property crossover from relaxor behaviour to normal ferroelectric state.

The crossover from relaxor to normal ferroelectric phase in the (1-x)$(Pb_{0.5}Sr_{0.5})(Zr_{0.5}Ti_{0.5})O_3$-x$PbTiO_3$ (PSZT-PT) solid solution indicates that the short-range disordered polar state is weakened and the long-range ferroelectricity is enhanced, while the structure transforms from the non-polar (pseudo-)cubic to the polar tetragonal symmetry. From the crystal chemistry point of view, such a crossover and the associated transformations can be attributed to the effects of the substitution of lead titanate for lead-strontium zirconate-titanate. $PbTiO_3$ is a well-known prototypical ferroelectric material. It possesses two ferroelectrically active cations, Pb^{2+} and Ti^{4+}, occupying the A-site and B-site of perovskite structure, respectively. Since Pb belongs to Group XIV in the Periodic Table and has an electronic configuration of $[Xe]4f^{14}5d^{10}6s^26p^2$, Pb^{2+} ion possesses lone-pair electrons on the $6s^2$ orbital [105], [106]. These lone-pair electrons are stereochemically active and favour the formation of dipole. Therefore, the ionic distortion of the perovskite structure and the induced dipole are enhanced as the concentration of lead ions increases on the A-site with the substitution of PT, which leads to the formation of long-range polar ordered state and thereby the ferroelectricity [107]. The tetravalent titanium ion Ti^{4+} is more susceptible of off-center displacement within the octahedral site than Zr^{4+} ion which tends to be disordered and central to the octahedral site. Thus, the substitution of Ti^{4+} for Zr^{4+} in PSZT also favours the establishment of the long-range ferroelectric order.

In the relaxor ferroelectric $(Pb_{0.5}Sr_{0.5})(Zr_{0.5}Ti_{0.5})O_3$ (PSZT) and the (1-x)PSZT-xPT solid solutions with small amounts of PT (i.e. x = 0.05, 0.10), the A-site is occupied by both Pb^{2+} and Sr^{2+} ions, and the B-site is occupied by both Zr^{4+} and Ti^{4+} ions, in a disordered way. The presence of non-ferroelectrically active ions Sr^{2+} on the A-site and Zr^{4+} on the B-site interrupt the interactions among the ionic dipoles arising from Pb^{2+} and Ti^{4+}, breaking

down the potential long-range polar order. As a result, only short-range polar order and polar nanoregions are formed, and the crystal structure remains cubic, leading to the observed relaxor ferroelectric behaviour. This scenario is illustrated in Figure 4.14(a).

The substitution of PT for PSZT introduces more ferroelectrically active Pb^{2+} and Ti^{4+} ions onto the A-site and B-site, replacing the non-ferroelectrically active Sr^{2+} and Zr^{4+}, respectively, which allows the polar regions to grow and their interactions to be enhanced. When the substitution rate is larger than 10% ($x = 0.10 \sim 0.25$), the increasing polar order induced by PT gradually takes over the chemical and polar disorders so that a long-range polar order starts to emerge, leading to the formation of the polar tetragonal symmetry, the growth of nano-domains into macro-domains and the establishment of ferroelectricity. This scenario is illustrated in Figure 4.14 (b). For $x \geqslant 0.275$, the material shows a well-established ferroelectric phase with long-range polar order and tetragonal structure. Overall, the chemical substitution of PT for PSZT has resulted in the macroscopic crossover from realxor ferroelectric behaviour to normal ferroelectric properties, which arises from a series of intriguing transformations on multiple scales, from nano-domains to macro-domains, from non-polar cubic structure to polar tetragonal structure, due to the increasing effects of ferroelectrically active Pb^{2+} and Ti^{4+} ions in the PSZT-PT solid solution system.

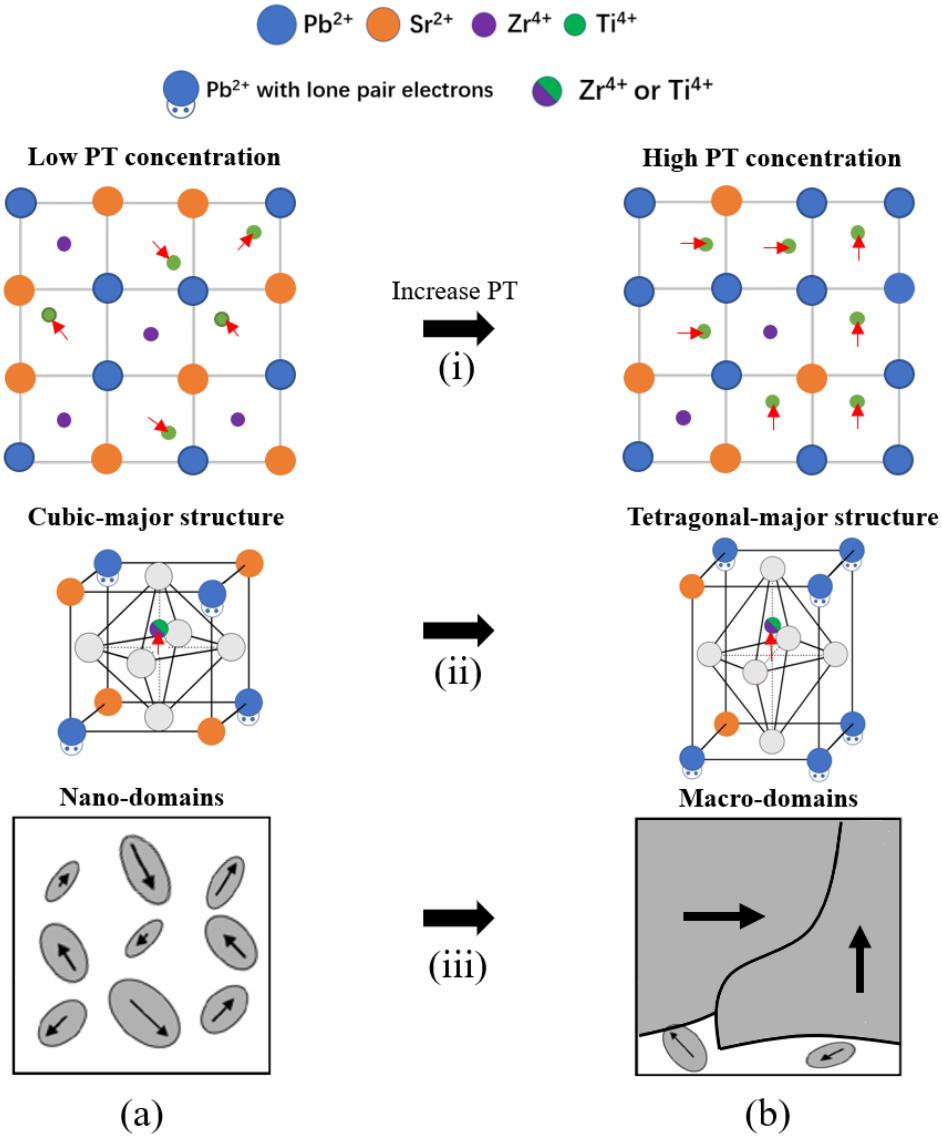

Figure 4.14 **Effects of increasing concentration of lead titanate in the (1-x)($Pb_{0.5}Sr_{0.5}$)($Zr_{0.5}Ti_{0.5}$)O_3-x$PbTiO_3$ solid solution system on (i) chemical and polar order/disorder, (ii) crystal structures and (iii) domain structures (where arrows indicate dipole moments in the corresponding domains). Column (a) illustrate the scenarios with the relaxor compositions (PSZT, or (1-x)PSZT-xPT with x = 0.05). Column (b) represents the scenario with (1-x)PSZT-xPT with higher PT concentrations (0.10 < x < 0.275).**

4.5. Conclusions

In this chapter, the crossover from relaxor state to normal ferroelectric phase in the (1-x)$Pb_{0.5}Sr_{0.5}Zr_{0.5}Ti_{0.5}O_3$-x$PbTiO_3$ (PSZT-PT) solid solution is systematically studied by

means of dielectric and ferroelectric measurements, Vogel-Fulcher law and Curie-Weiss law analyses, and transmission electron microscopy (TEM). The dielectric properties of the PSZT-PT samples reveal that the compositions with low PT concentrations, x = 0.05 ~ 0.10, exhibit a broad and diffuse peak on the variation of dielectric constant versus temperature, whose temperature (T_{max}) increases with increasing frequency, indicating typical relaxor behaviour. As x increases, the dielectric anomaly associated with relaxor behaviour gradually weakens, transforms into a shoulder, and eventually disappears for x = 0.25. Interestingly, with the increase of PT concentration $x \geq 0.10$, the dielectric permittivity shows a second anomaly above T_{max}. This phenomenon of double peaks can be observed in the intermediate composition range of x = 0.10 ~ 0.25, in which the transition from relaxor behaviour to normal ferroelectric state takes place. Whereas the dielectric maxima of frequency dependent peak (peak at T_{max}) gradually decreases and disappears, the magnitude of the second peak which is frequency independent, increases as x increases. These two peaks arise from the mixed cubic and tetragonal phases, respectively, coexisting in the intermediate composition range, as determined by the structural analysis presented in Chapter 3. The appearance, disappearance and coexistence of the two peaks match the variations of the phase fractions of the cubic versus tetragonal phase. For $x \geqslant 0.275$, a single frequency-independent peak appears, and the peak of dielectric constant becomes sharper as x further increases. With increasing x, the Curie Weiss temperature (T_C) of samples becomes higher, and ΔT_{max} decreases, indicating enhancement of ferroelectricity and weakening of relaxor properties.

The dielectric data of the PSZT-PT samples is fitted with the Vogel-Fulcher (VF) law and the Curie Weiss (CW) law and relevant parameters such as freezing temperature (T_f) and the Burns temperature (T_B) are obtained for the relaxor compositions. It is found that as x increases, both the T_B and the T_f of the PSZT-PT samples exhibit an increasing trend. The parameters of various phase transition temperatures obtained from these analyses will be utilized to establish the phase diagram of the PSZT-PT solid solution system, which will be further discussed in the following chapter.

The difference between relaxor and ferroelectric properties is analyzed in terms of polarization - electric field relation and ferroelectric hysteresis loops. As x increases, the shape of the hysteresis loop transforms from an almost linear and narrow loop to a wide and broad loop with increasing remanent polarization and coercive field, confirming the transformation from relaxor behaviour to typical ferroelectric properties.

Furthermore, the bright field images obtained from TEM allow us to study the transformation of domain associated with the crossover from relaxor to normal ferroelectric phase. The morphology of domains in the relaxor composition (x = 0.15) exhibits a wavy-shaped pattern of about 10 nanometers wide, characteristic of polar nanoregions in relaxors. As the concentration of x increases, the wavy-shaped nano-domains transform into much larger domains with a meso- to macroscopic size of about 0.2 μm (x=0.50).

The mechanisms of the crossover in the PSZT-PT system are discussed and explained based on the results of crystal structural analysis presented in Chapter 4 and the crystal chemistry consideration. In general, the macroscopic crossover from realxor ferroelectric bahaviour to normal ferroelectric properties can be attributed to the effects of the substitution of the ferroelectrically active Pb^{2+} and Ti^{4+} ions for the non-ferroelectrically active Sr^{2+} and Zr^{4+} ions, which cause a series of intriguing transformations on multiple scales, from nano-domains to macro-domains, from non-polar cubic structure to polar tetragonal structure, leading to the composition-induced crossover in the PSZT-PT solid solution. Thus, the analysis of the dielectric, ferroelectric and domain properties provides a general picture of the transformations from various perspectives, and allows us to construct overall phase diagrams of the PSZT-PT solid solution system in terms of structures and properties, which will be described in **Chapter. 5**.

Chapter 5.

Phase Diagrams, General Conclusions and Future Directions

The successful synthesis of the novel solid solution of $(1-x)(Pb_{0.5}Sr_{0.5})(Zr_{0.5}Ti_{0.5})O_3$-$xPbTiO_3$ (PSZT-PT) and the systematic characterizations of its structures and physical properties, presented in Chapters 3 & 4, allow us to draw some general conclusions in the forms of structure and property phase diagrams of this pseudo-binary system to better highlight the composition-induced crossover from relaxor behaviour to ferroelectric state. The results will also be presented in the framework of the $PbZrO_3$-$PbTiO_3$-$SrTiO_3$ (PZ-PT-PS) ternary phase diagram. Finally, the future directions of research are suggested.

5.1. Structural Phase Diagram

The structural phase diagram of the $(1-x)(Pb_{0.5}Sr_{0.5})(Zr_{0.5}Ti_{0.5})O_3$-$xPbTiO_3$ (PSZT-PT) solid solution system is constructed based on the results of the structural analysis presented in Chapter 3, as shown in Figure 5.1. It correlates the crystal symmetries, lattice parameters and phase fractions with the composition x. It is found that with the increase of PT content, the structure of the PSZT-PT system gradually transforms from a centrosymmetric, nonpolar, cubic phase (Pm-3m) into a non-centrosymmetric, polar, tetragonal phase (P4mm). The cubic to tetragonal phase transformation occurs within the intermediate composition region of $x = 0.10 – 0.25$, where the tetragonal phase forms alongside the initial cubic phase in $x = 0.10$, and becomes dominant in the mixed phases when $x \geq 0.175$, at the expenses of the cubic phase. It eventually takes over the cubic phase completely when $x \geq 0.275$.

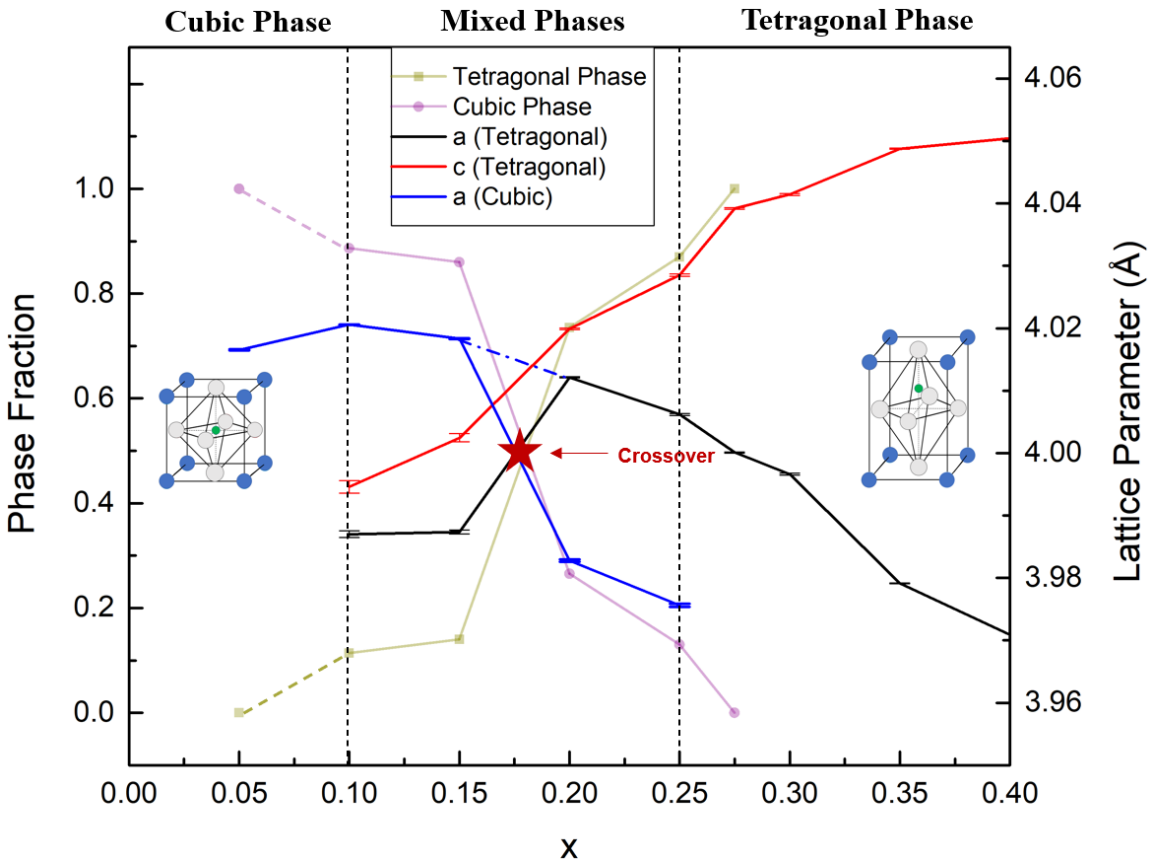

Figure 5.1 **The structural phase diagram established for the (1-x)$(Pb_{0.5}Sr_{0.5})(Zr_{0.5}Ti_{0.5})O_3$-x$PbTiO_3$ (x = 0.05~ 0.40) solid solution, based on the variation of crystal symmetry and lattice parameters as a function of composition refined from XRD data.**

As x increases, the lattice parameter *a* of the cubic phase remains almost constant before dropping suddenly at x = 0.15 where the tetragonal phase becomes significant. The lattice parameter *c* of the tetragonal phase shows a general increasing trend, while the lattice parameter *a* exhibits a clear descending trend, for compositions of x > 0.20. In the intermediate composition region where both the cubic and tetragonal phase coexist, a crossover of the lattice parameter *a* between the cubic and tetragonal phases occurs around x = 0.175, where the tetragonal phase begins to take dominance and the fraction of the cubic phase in mixed phases gradually fades out. As a result, the lattice parameter *a* of the cubic phase decreases abruptly, while the lattice parameter *a* of the tetragonal phase increases sharply in the mixed phase region. Across the intermediate composition region, the lattice parameter *a* of the cubic phase (x < 0.20) and the tetragonal phase (x

$\geqslant$ 0.20) can be considered to link to each other (through the dashed blue line), giving rise to an overall decreasing trend with the increase of the PT concentration.

Interestingly, the crossover of the lattice parameter *a* between the cubic and tetragonal phases occurs at x = 0.175 (shown as the star mark in Figure 5.1), consistent with the crossover of the fractions of the respective phases. The trends of the phase fractions indicate clearly that the structural symmetry of the PSZT-PT solid solution transforms from the cubic phase to the tetragonal, passing through an intermediate composition region where the crossover from the cubic to tetragonal phase takes place with the increase of PT concentration. In addition, with the increase of the PT concentration, the tetragonality is found to increase, which indicates an enhancement of lattice distortion towards the tetragonal structure (see Figure. 3. 14).

5.2. Dielectric Phase Diagram

The evolution of the dielectric and ferroelectric properties in the of (1-x) $(Pb_{0.5}Sr_{0.5})(Zr_{0.5}Ti_{0.5})O_3$-x$PbTiO_3$ (PSZT-PT) solid solution system can be represented by a dielectric phase diagram, as shown in Figure. 5.2. It is established based on the measured relaxor behaviour, ferroelectricity, temperature of the maximum dielectric permittivity (T_{max}) and temperature of ferroelectric phase transition (T_C), and the relevant parameters obtained by fitting to the Curie-Weiss (CW) law and Vogel-Fulcher (VF) law, namely, the Burns temperature (T_B) that indicates the paraelectric to ergodic relaxor phase transition and the ergodic to non-ergodic relaxor phase transition temperature (T_f).

The dielectric properties of the PSZT-PT solid solution reveal that the compositions with low PT concentrations, x = 0 ~ 0.10, exhibit a broad and diffuse peak on the variation of dielectric constant versus temperature, whose temperature (T_{max}) increases with increasing frequency, indicating typical relaxor behaviour. Upon cooling, the relaxor compositions transform from the paraelectric into an ergodic relaxor phase (shown as grey region in Figure 5.2) at the Burns temperature (T_B), at which the polar nanoregions (PNRs) start to grow, giving rise to the characteristic dielectric relaxation. Upon further cooling within the ergodic relaxor state, the size of PNRs gradually increases, and the dynamics of dipole fluctuations decreases. Below the temperature T_f, which is defined as the freezing temperature [12], the relaxor is in a non-ergodic phase, where the PNRs become

static and completely frozen with an infinite relaxation time [12] (shown as orange region in Figure 5.2).

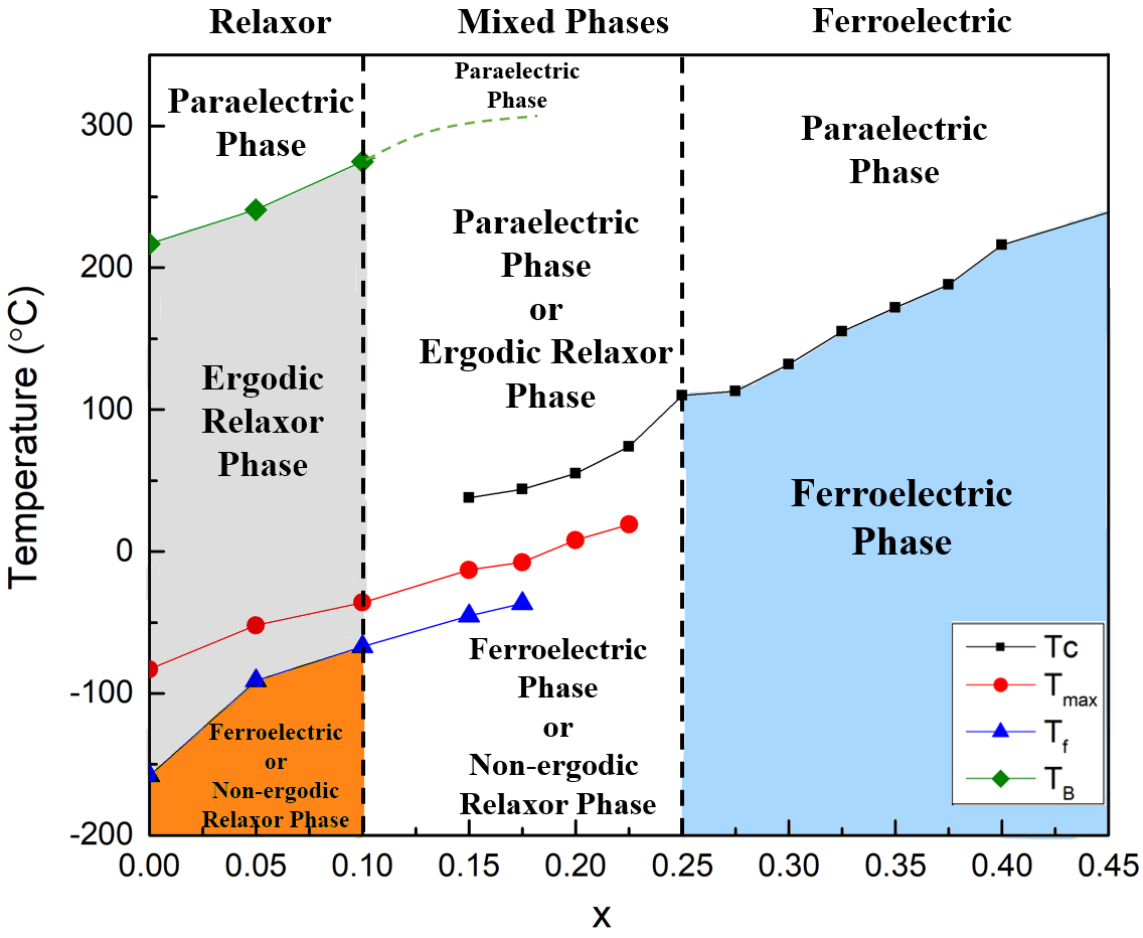

Figure 5.2 **The dielectric phase diagram of the (1-x) $(Pb_{0.5}Sr_{0.5})(Zr_{0.5}Ti_{0.5})O_3$-$xPbTiO_3$ (x = 0 ~ 0.45) solid solution established based on the variations of the physical properties and characteristic temperatures as a function of composition. The data for x= 0.0 sample is adapted from the Ref. [76].**

In the intermediate composition range ($0.10 \leq x \leq 0.25$), the crossover from relaxor behaviour to normal ferroelectric state takes place while the phase component gradually changes from cubic to tetragonal with mixed phases. In this region, the Burns temperature T_B cannot be accurately determined due to the influence of the increasing ferroelectric phase component. Thus, it is only estimated by extrapolation (dashed green line).

For temperatures below T_B, the red curve and black curve represent the temperatures of the dielectric maximum of the frequency dependent peaks (T_{max}) and that

of the frequency independent peaks (T_C), respectively. These two peaks arise from the mixed cubic and tetragonal phases, respectively, coexisting in the intermediate composition range, as determined by the structural analysis presented in **Chapter 3**. The appearance, disappearance and coexistence of the two peaks match the variations of the phase fractions of the cubic versus tetragonal phase, which is consistent with the structural phase diagram in Figure 5.1. The freezing temperatures (T_f) of the relaxor and intermediate compositions are shown as blue curve.

For $x \geqslant 0.275$, the PSZT-PT samples exhibit a normal ferroelectric phase at low temperature (shown as blue region in Figure 5.2). Upon heating, the materials transform from normal ferroelectric phase into paraelectric phase at the Curie temperature (T_C). As x increases, the Curie Weiss temperature (T_C) becomes higher, and ΔT_{max} decreases, indicating enhancement of ferroelectricity and weakening of relaxor properties. With increasing x, the T_C, T_{max}, and T_f of all the compositions show a general increasing trend.

The structural and dielectric phase diagrams illustrate the evolutions of the crystal structures and physical properties of the PSZT - PT solid solution, and provide us a clear picture of the crossover from relaxor to ferroelectric state in this pseudo-binary system.

5.3. Ternary Phase diagram

The results obtained in this work and the structural and dielectric phase diagrams established for the $Pb_{0.5}Sr_{0.5})(Zr_{0.5}Ti_{0.5})O_3$-$xPbTiO_3$ (PSZT-PT) pseudo-binary solid solution system can be placed in the framework of the ternary phase diagram of $SrTiO_3$-$PbTiO_3$-$PbZrO_3$, proving new data inside the diagram, as displayed in Figure 5.3. The composition series of PSZT-PT is indicated by the blue line. It is expected that at least in a narrow composition range along this line (as marked by the yellow dashed oval), the ternary compounds would exhibit the similar transform from the relaxor phase with cubic symmetry to the normal ferroelectric phase with tetragonal symmetry with increasing concentration of PT, i.e. along the direction of the blue arrow, although the composition ranges delimiting the relaxor state, the ferroelectric phase, and the mixed phases may be slightly different. More discussion on this ternary phase diagram will be provided in Sec. 5.5. Future Directions.

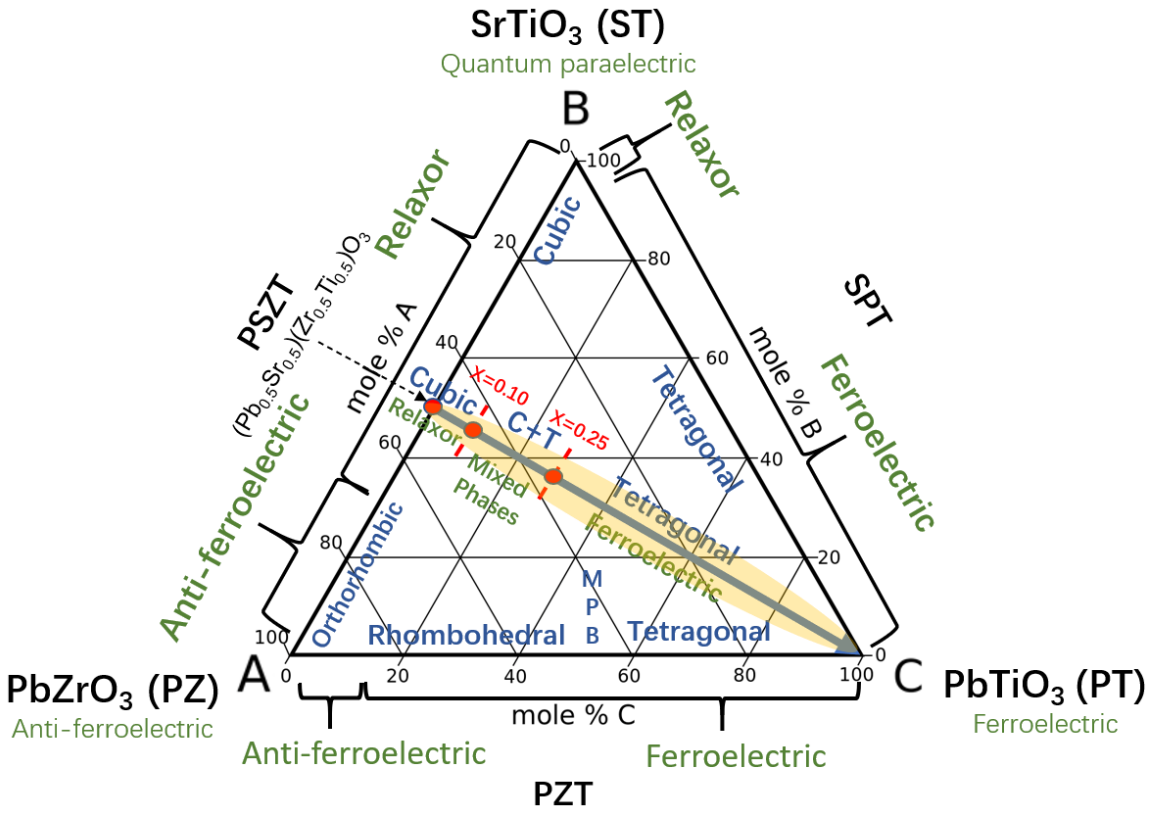

Figure 5.3 **The ternary phase diagram of the $SrTiO_3$-$PbTiO_3$-$PbZrO_3$ system with the composition series of $(1-x)(Pb_{0.5}Sr_{0.5})(Zr_{0.5}Ti_{0.5})O_3$-$xPbTiO_3$ shown as the blue line. Different phases and structural symmetries and various properties are illustrated in blue and green characters, respectively.**

5.4. General Conclusions

The investigation of the chemical and physical properties of function materials constitutes an essential part of material science. Synthesis of novel materials allows us to explore new and interesting materials with improved properties, and helps us to notice and address the drawbacks in the existing systems. In this work, the investigation of the PSZT-PT solid solution system provides us a novel lead-reduced relaxor-based functional material system with a wide range of transition temperature and good dielectric performance. In addition, the investigation of the transformation from relaxor to normal ferroelectrics can help us understand the differences between them, and provide us a path to study the mechanism behind relaxor ferroelectric behaviours.

In summary, a novel relaxor ferroelectric material system, (1-x)($Pb_{0.5}Sr_{0.5}$)($Zr_{0.5}Ti_{0.5}$)O_3-x$PbTiO_3$ (PSZT-PT) (x = 0.05, 0.10, 0.15, 0.175, 0.20, 0.225, 0.25, 0.275, 0.30, 0.35, 0.50, 0.65, 0.75, 0.85 and 0.95), has been synthesized and its physical and chemical properties have been characterized by X-ray diffraction (XRD), dielectric spectroscopy, ferroelectric testing and transmission electron microscopy. The overall evolutions of the structures and physical properties as a function of composition in the PSZT-PT system have been uncovered, which can be summarized and presented in Figure 5.4 in terms of phase symmetry, dielectric properties, ferroelectric properties and domain structure.

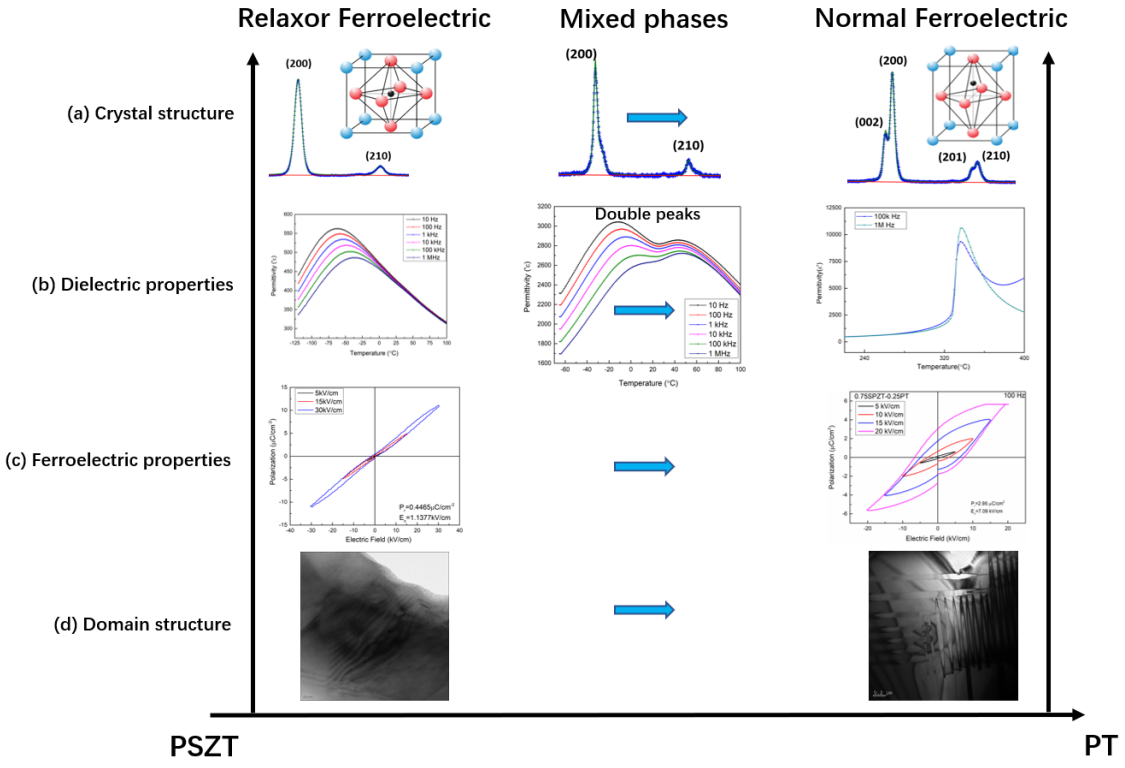

Figure 5.4 Illustration of the overall evolutions of the structures and physical properties as a function of composition in the PSZT-PT system in terms of phase symmetry, dielectric properties, ferroelectric properties and domain structure.

From the crystal chemistry aspects, the ceramics of the PSZT-PT solid solution system have been successfully synthesized by the solid-state reaction method and sintering process. The phase components and crystal structure of the new solid solution

have been investigated by X-ray diffraction. The refinement results of the experimental data by GSAS II academic software reveal that the structure of the (1-x)($Pb_{0.5}Sr_{0.5}$)($Zr_{0.5}Ti_{0.5}$)O_3-x$PbTiO_3$ system gradually transforms from a centrosymmetric, nonpolar, cubic phase (Pm-3m) into a non-centrosymmetric, polar, tetragonal phase (P4mm) with the increase of PT content, as shown in Figure 5.4(a). The phase transformation occurs within the intermediate composition region of x = 0.10 – 0.25, where the tetragonal phase forms alongside the initial cubic phase in x = 0.10, and becomes dominant in the mixed phases when $x \geq 0.175$. The tetragonal phase eventually takes over the cubic phase completely when $x \geq 0.275$. As x increases, the lattice parameter *a* shows a general increasing trend and the lattice parameter *c* exhibits a general decreasing trend. A crossover of the lattice parameter *a* between the cubic and tetragonal phases occurs at x = 0.175, consistent with the crossover of the fractions of the respective phases. With the increase of the PT concentration, the tetragonality is found to increase, which indicates an enhancement of lattice distortion towards the tetragonal structure. The volume of unit cell shows a general descending trend with increasing x.

The dielectric properties of PSZT-PT samples have been investigated by dielectric spectroscopy at frequencies from 10 Hz to 1 MHz (as shown in Figure 5.4 (b)). For compositions with low PT concentrations, x = 0.05 ~ 0.10, a broad and diffuse peak on the variation of dielectric constant versus temperature is observed. The temperature at dielectric maxima (T_{max}) increases with increasing frequency, indicating typical relaxor behaviour. As x increases, the dielectric anomaly associated with relaxor behaviour gradually weakens, transforms into a shoulder, and eventually disappears for x = 0.25. Interestingly, with the increase of PT concentration $x \geq 0.10$, the dielectric permittivity shows a second anomaly above T_{max}. This phenomenon of double peaks can be observed in the intermediate composition range of x = 0.10 ~ 0.25, in which the transition from relaxor behaviour to normal ferroelectric state takes place. Whereas the dielectric maxima of frequency dependent peak (at T_{max}) gradually decreases and disappears, the magnitude of the second peak which is frequency independent, increases as x increases. These two peaks arise from the mixed cubic and tetragonal phases, respectively, coexisting in the intermediate composition range, as determined by the structural analysis presented in Figure 5.4(a). The appearance, disappearance and coexistence of the two dielectric peaks match the variations of the phase fractions of the cubic versus tetragonal phase. For $x \geq 0.275$, a single frequency- independent peak appears, and the peak of

dielectric constant becomes sharper as x further increases. With increasing x, the Curie temperature (T_C) increases, and ΔT_{max} decreases, indicating enhancement of ferroelectricity and weakening of relaxor properties. The dielectric data of the PSZT-PT samples is fitted with the Vogel-Fulcher (VF) law and the Curie-Weiss (CW) law and relevant parameters such as freezing temperature (T_f) and the Burns temperature (T_B) are obtained for the relaxor compositions. It is found that as x increases, the T_f of the PSZT-PT samples exhibits an increasing trend, and the T_B increases slightly. The parameters of various phase transition temperatures obtained from these analyses are utilized to establish the dielectric phase diagram of the PSZT-PT solid solution system, as shown in Figure 5.2.

Interestingly, the room-temperature dielectric constant of PSZT is increased by 300% thanks to the substitution of PT, reaching almost 3,032 for x = 0.20 (at 1 Hz), making this material a new candidate for multilayered ceramic capacitors.

The difference between relaxor and ferroelectric properties is analyzed in terms of polarization - electric field relation and ferroelectric hysteresis loops (as shown in Figure 5.4 (c)). As x increases, the shape of the hysteresis loop transforms from an almost linear and narrow loop to a wide and broad loop with increasing remanent polarization and coercive field, confirming the transformation from relaxor behaviour to typical ferroelectric properties.

The bright field images obtained from TEM allow us to study the transformation of domain associated with the crossover from relaxor to normal ferroelectric phase (as shown in the Figure 5.4 (d)). The morphology of domains in the relaxor composition (x = 0.15) exhibits a wavy-shaped pattern of about 10 nanometres wide, characteristic of polar nanoregions in relaxors. As the concentration of x increases, the wavy-shaped nano-domains transform into much larger domains with a meso- to macroscopic size of about 0.2 μm. These results indicate that the crossover from relaxor behaviour to normal ferroelectric state is accompanied by the transformation of polar domains from nano- to meso-/macro-scopic scales.

In general, the macroscopic crossover from realxor ferroelectric behaviour to normal ferroelectric properties can be attributed to the effects of the substitution of the ferroelectrically active Pb^{2+} and Ti^{4+} ions for the non-ferroelectrically active Sr^{2+} and Zr^{4+}

ions, which causes a series of intriguing transformations on multiple scales, from nano-domains to macro-domains, from non-polar cubic structure to polar tetragonal structure, leading to the composition-induced crossover in the PSZT-PT solid solution.

In conclusion, this research provides a general picture of the phase transformations from various perspectives, which are induced by chemical substitution, and allows us to construct the phase diagrams of the PSZT-PT solid solution system in terms of structures and properties, uncovering and the mechanism behind the crossover between relaxor and ferroelectric phases, and exploring a new lead-reduced relaxor ferroelectric system.

5.5. Future Directions

Looking forward, for the PSZT-PT pseudo-binary system, further studies such as structural analysis at high temperatures need to be performed to fully determine the phase transformations, especially within the intermediate composition range. In addition, the effects of quantum paraelectric nature of $SrTiO_3$ on the phase behaviour and relaxor to ferroelectric crossover need to be clarified. From practical point of view, it is worthwhile exploring the applications of the optimum composition (0.80PSZT-0.20PT) in the fabrication of high energy density multilayered ceramic capacitors. Potential patent protection may be filed.

Expanding this work into the ternary phase diagram of $SrTiO_3$-$PbTiO_3$-$PbZrO_3$ (Figure 5.3), there are several interesting projects that are worth studying. For instance, to complete the ternary diagram, more series of compositions need to be selected and investigated. In particular, it will be interesting to study the transition from anti-ferroelectric to ferroelectric with starting point at 80% of $PbZrO_3$ and 20% of $SrTiO_3$, i.e. $(Pb_{0.8}Sr_{0.2})(Zr_{0.8}Ti_{0.2})O_3$. It is anticipated that in this series of compositions, a ternary morphotropic phase boundary (MPB) region may exist, which is extended from the MPB region of the PZT binary system. By exploring the relevant compositions in this ternary phase diagram, it would be possible to develop the best multifunctional materials exhibiting relaxor behaviour, antiferroelectricity and ferroelectricity for various applications, to better understand the mechanism of crossover between various phases and different properties and to establish the structure - property relations on multiple scales.

References

[1] B. Wang, “Growth and characterization of lead zirconate-titanate ($PbZr_{1-x}Ti_xO_3$)-based novel piezo-/ferroelectric single crystals,” PhD Thesis, Science: Department of Chemistry, 2016.

[2] A. S. Bhalla, R. Guo, and R. Roy, “The perovskite structure—a review of its role in ceramic science and technology,” Mater. Res. Innov., vol. 4, no. 1, pp. 3–26, 2000.

[3] M. S. Vijaya, Piezoelectric materials and devices: applications in engineering and medical sciences. CRC press, 2012.

[4] D. Damjanovic, “Ferroelectric, dielectric and piezoelectric properties of ferroelectric thin films and ceramics,” Rep. Prog. Phys., vol. 61, no. 9, p. 1267, 1998.

[5] J. F. Nye, Physical properties of crystals: their representation by tensors and matrices. Oxford university press, 1985.

[6] Y. Fan, Z. Zhou, R. Liang, and X. Dong, “Designing novel lead-free $NaNbO_3$-based ceramic with superior comprehensive energy storage and discharge properties for dielectric capacitor applications via relaxor strategy,” J. Eur. Ceram. Soc., vol. 39, no. 15, pp. 4770–4777, 2019.

[7] G. A. Smolensky, “Proc. Int. Meeting on Ferroelectricity, Kyoto, 1969,” J Phys Soc Jpn, vol. 28, p. 26, 1970.

[8] Z.-G. Ye and H. Schmid, “Optical, dielectric and polarization studies of the electric field-induced phase transition in $Pb(Mg_{1/3}Nb_{2/3})O_3$ [PMN],” Ferroelectrics, vol. 145, no. 1, pp. 83–108, 1993.

[9] X. Dai, Z. Xu, and D. Viehland, “The spontaneous relaxor to normal ferroelectric transformation in La-modified lead zirconate titanate,” Philos. Mag. B, vol. 70, no. 1, pp. 33–48, 1994.

[10] N. Nanakorn, P. Jalupoom, N. Vaneesorn, and A. Thanaboonsombut, “Dielectric and ferroelectric properties of $Ba(Zr_xTi_{1-x})O_3$ ceramics,” Ceram. Int., vol. 34, no. 4, pp. 779–782, 2008.

[11] T. R. Shrout, Z. P. Chang, N. Kim, and S. Markgraf, “Dielectric behavior of single crystals near the (1-x)$Pb(Mg_{1/3}Nb_{2/3})O_3$-(x)$PbTiO_3$ morphotropic phase boundary,” Ferroelectr. Lett. Sect., vol. 12, no. 3, pp. 63–69, 1990.

[12] A. A. Bokov and Z.-G. Ye, “Recent progress in relaxor ferroelectrics with perovskite structure,” J. Mater. Sci., vol. 41, no. 1, pp. 31–52, 2006.

[13] A. A. Bokov and Z.-G. Ye, “Reentrant phenomena in relaxors,” Nanoscale Ferroelectr. Multiferroics Key Process. Charact. Issues Nanoscale Eff., vol. 1, pp. 729–64, 2016.

[14] A. A. Bokov et al., “Compositional disorder, polar nanoregions and dipole dynamics in $Pb(Mg_{1/3}Nb_{2/3})O_3$-based relaxor ferroelectrics,” Z. Für Krist.-Cryst. Mater., vol. 226, no. 2, pp. 99–107, 2011.

[15] M. D. Glinchuk and R. Farhi, “A random field theory based model for ferroelectric relaxors,” J. Phys. Condens. Matter, vol. 8, no. 37, p. 6985, 1996.

[16] A. A. Bokov, “Kinetics of a broad phase transition in crystals with frozen-in disorder,” Phys Solid State, vol. 36, pp. 36–45, 1994.

[17] V. Westphal, W. Kleemann, and M. D. Glinchuk, “Diffuse phase transitions and random-field-induced domain states of the ‘“relaxor”’ferroelectric $Pb(Mg_{1/3}Nb_{2/3})O_3$,” Phys. Rev. Lett., vol. 68, no. 6, p. 847, 1992.

[18] V. M. Ishchuk, “Was it necessary to introduce the notion ‘relaxor ferroelectrics’?-the problem of phase transitions in $(Pb,Li_{1/2}\text{-}La_{1/2})(Zr,Ti)O_3$,$(Pb,La)(Zr,Ti)O_3$,

$Pb(Mg_{1/3}Nb_{2/3})O_3$, $Pb(In_{1/2}Nb_{1/2})O_3$. and related materials. 1. model conceptions," Ferroelectrics, vol. 255, no. 1, pp. 73–109, 2001.
[19] V. V. Kirillov and V. A. Isupov, "Relaxation polarization of $Pb(Mg_{1/3}Nb_{2/3})O_3$ (PMN)-A ferroelectric with a diffused phase transition," Ferroelectrics, vol. 5, no. 1, pp. 3–9, 1973.
[20] V. A. Isupov, "Ferroelectric and antiferroelectric perovskites $PbB'_{0.5}B''_{0.5}O_3$," Ferroelectrics, vol. 289, no. 1, pp. 131–195, 2003.
[21] Z.-G. Ye, "Relaxor ferroelectric complex perovskites: structure, properties and phase transitions," in Key Engineering Materials, vol. 155, pp. 81–122, 1998.
[22] D. Viehland, S. J. Jang, L. E. Cross, and M. Wuttig, "Freezing of the polarization fluctuations in lead magnesium niobate relaxors," J. Appl. Phys., vol. 68, no. 6, pp. 2916–2921, 1990.
[23] H. Vogel, "The law of the relation between the viscosity of liquids and the temperature," Phys Z, vol. 22, pp. 645–646, 1921.
[24] G. S. Fulcher, "Analysis of recent measurements of the viscosity of glasses," J. Am. Ceram. Soc., vol. 8, no. 6, pp. 339–355, 1925.
[25] A. A. Bokov and Z.-G. Ye, "Dielectric relaxation in relaxor ferroelectrics," J. Adv. Dielectr., vol. 2, no. 02, p. 1241010, 2012.
[26] Z.-G. Ye and A. A. BOKOV, "Dielectric and structural properties of relaxor ferroelectrics," Ferroelectrics, vol. 302, no. 1, pp. 227–231, 2004.
[27] A. A. Bokov and Z. G. Ye, "Freezing of dipole dynamics in relaxor ferroelectric $Pb(Mg_{1/3}Nb_{2/3})O_3$-$PbTiO_3$ as evidenced by dielectric spectroscopy," J. Phys. Condens. Matter, vol. 12, no. 34, p. L541, 2000.
[28] A. A. Bokov and Z.-G. Ye, "Low-frequency dielectric spectroscopy of the relaxor ferroelectric $Pb(Mg_{1/3}Nb_{2/3})O_3$-$PbTiO_3$," Phys. Rev. B, vol. 65, no. 14, p. 144112, 2002.
[29] L. Néel, "Influence des fluctuations thermiques sur l'aimantation de grains ferromagnétiques très fins," Comptes Rendus Hebd. Seances Acad. Sci., vol. 228, no. 8, pp. 664–666, 1949.
[30] L. E. Cross, "Relaxor ferroelectrics," Ferroelectrics, vol. 76, no. 1, pp. 241–267, 1987.
[31] W. Kleemann, "Random-field induced antiferromagnetic, ferroelectric and structural domain states," Int. J. Mod. Phys. B, vol. 7, no. 13, pp. 2469–2507, 1993.
[32] E. Husson, M. Chubb, and A. Morell, "Superstructure in $Pb(Mg_{1/3}Nb_{2/3})O_3$ ceramics revealed by high resolution electron microscopy," Mater. Res. Bull., vol. 23, no. 3, pp. 357–361, 1988.
[33] L. A. Bursill, H. Qian, J. Peng, and X. D. Fan, "Observation and analysis of nanodomain textures in the dielectric relaxor lead magnesium niobate," Phys. B Condens. Matter, vol. 216, no. 1–2, pp. 1–23, 1995.
[34] E. A. Little, "Dynamic behavior of domain walls in barium titanate," Phys. Rev., vol. 98, no. 4, p. 978, 1955.
[35] R. Blinc, "Soft modes in ferroelectrics and antiferroelectrics.," 1974.
[36] N. Zhang et al., "The missing boundary in the phase diagram of $Pb(Zr_{1-x}Ti_x)O_3$," Nat. Commun., vol. 5, no. 1, pp. 1–9, 2014.
[37] B. Jaffe, R. S. Roth, and S. Marzullo, "Piezoelectric properties of lead zirconate-lead titanate solid-solution ceramics," J. Appl. Phys., vol. 25, no. 6, pp. 809–810, 1954.
[38] D. M. Hatch, H. T. Stokes, R. Ranjan, S. K. Mishra, D. Pandey, and B. J. Kennedy, "Antiferrodistortive phase transition in $Pb(Ti_{0.48}Zr_{0.52})O_3$: Space group of the lowest temperature monoclinic phase," Phys. Rev. B, vol. 65, no. 21, p. 212101, 2002.
[39] W. Cao and L. E. Cross, "Theoretical model for the morphotropic phase boundary in lead zirconate–lead titanate solid solution," Phys. Rev. B, vol. 47, no. 9, p. 4825, 1993.

[40] B. Noheda, D. E. Cox, G. Shirane, J. A. Gonzalo, L. E. Cross, and S. E. Park, “A monoclinic ferroelectric phase in the $Pb(Zr_{1-x}Ti_x)O_3$ solid solution,” Appl. Phys. Lett., vol. 74, no. 14, pp. 2059–2061, 1999.
[41] Ragini, R. Ranjan, S. K. Mishra, and D. Pandey, “Room temperature structure of $Pb(Zr_{1-x}Ti_x)O_3$ around the morphotropic phase boundary region: A Rietveld study,” J. Appl. Phys., vol. 92, no. 6, pp. 3266–3274, 2002.
[42] N. Zhang, H. Yokota, A. M. Glazer, and P. A. Thomas, “The not so simple cubic structure of $Pb(Zr_{1-x}Ti_x)O_3$ (PZT): complex local structural effects in perovskites,” Acta Crystallogr. B, vol. 67, no. 6, pp. 461–466, 2011.
[43] K. A. Schönau et al., “Nanodomain structure of $Pb(Zr_{1-x}Ti_x)O_3$ at its morphotropic phase boundary: investigations from local to average structure,” Phys. Rev. B, vol. 75, no. 18, p. 184117, 2007.
[44] Y. M. Jin, Y. U. Wang, A. G. Khachaturyan, J. F. Li, and D. Viehland, “Adaptive ferroelectric states in systems with low domain wall energy: Tetragonal microdomains,” J. Appl. Phys., vol. 94, no. 5, pp. 3629–3640, 2003.
[45] Y. U. Wang, “Diffraction theory of nanotwin superlattices with low symmetry phase: Application to rhombohedral nanotwins and monoclinic M A and M B phases,” Phys. Rev. B, vol. 76, no. 2, p. 024108, 2007.
[46] D. Vanderbilt and M. H. Cohen, “Monoclinic and triclinic phases in higher-order Devonshire theory,” Phys. Rev. B, vol. 63, no. 9, p. 094108, 2001.
[47] H. Jaffe and D. A. Berlincourt, “Piezoelectric transducer materials,” Proc. IEEE, vol. 53, no. 10, pp. 1372–1386, 1965.
[48] Y. Xie, “Synthesis and characterization of piezo-/ferroelectric lead zirconate-titanate (PZT) single crystals and related ternary ceramics,” PhD Thesis, Science: Department of Chemistry, 2013.
[49] R. C. Buchanan, Ceramic materials for electronics: processing, properties, and applications. Marcel Dekker, Inc., 1986.
[50] Y. H. Bing, A. A. Bokov, Z. G. Ye, B. Noheda, and G. Shirane, “Structural phase transition and dielectric relaxation in $Pb(Zn_{1/3}Nb_{2/3})O_3$ single crystals,” J. Phys. Condens. Matter, vol. 17, no. 15, p. 2493, 2005.
[51] Y. Xu, Ferroelectric materials and their applications. Elsevier, 2013.
[52] N. F. Muhamad, R. A. M. Osman, M. S. Idris, and M. N. M. Yasin, “Physical and electrical properties of $SrTiO_3$ and $SrZrO_3$,” in EPJ Web of Conferences, vol. 162, p. 01052, 2017.
[53] D. E. Grupp and A. M. Goldman, “Giant piezoelectric effect in strontium titanate at cryogenic temperatures,” Science, vol. 276, no. 5311, pp. 392–394, 1997.
[54] H. Fujishita, S. Kitazawa, M. Saito, R. Ishisaka, H. Okamoto, and T. Yamaguchi, “Quantum paraelectric states in $SrTiO_3$ and $KTaO_3$: Barrett model, Vendik model, and quantum criticality,” J. Phys. Soc. Jpn., vol. 85, no. 7, p. 074703, 2016.
[55] J. Hemberger, M. Nicklas, R. Viana, P. Lunkenheimer, A. Loidl, and R. Böhmer, “Quantum paraelectric and induced ferroelectric states in,” J. Phys. Condens. Matter, vol. 8, no. 25, p. 4673, 1996.
[56] K. A. Müller and H. Burkard, “$SrTiO_3$: An intrinsic quantum paraelectric below 4 K,” Phys. Rev. B, vol. 19, no. 7, p. 3593, 1979.
[57] W. Zhong and D. Vanderbilt, “Effect of quantum fluctuations on structural phase transitions in $SrTiO_3$ and $BaTiO_3$,” Phys. Rev. B, vol. 53, no. 9, pp. 5047–5050, Mar. 1996.
[58] T. Schneider, H. Beck, and E. Stoll, “Quantum effects in an n-component vector model for structural phase transitions,” Phys. Rev. B, vol. 13, no. 3, p. 1123, 1976.

[59] H. WU and Q. JIANG, “The Calculation of Quantum Fluctuation and Dielectric Constants in Incipient Ferroelectrics,” J. Suzhou Railw. Teach. Coll., no. 4, p. 3, 2002.
[60] “Innovative Research and Products (iRAP) Inc. ET112: Piezoelectric Actuators and Motors—Types, Applications, new developments, Industry Structure and Global Markets, 2010.
[61] P. Sun et al., “High frequency PMN-PT 1-3 composite transducer for ultrasonic imaging application,” Ferroelectrics, vol. 408, no. 1, pp. 120–128, 2010.
[62] K. Ren, Y. Liu, X. Geng, H. F. Hofmann, and Q. M. Zhang, “Single crystal PMN-PT/epoxy 1-3 composite for energy-harvesting application,” Ieee Trans. Ultrason. Ferroelectr. Freq. Control, vol. 53, no. 3, pp. 631–638, 2006.
[63] X. Wang, “Evolutions of chemical and polar structures and electric properties in the Barium-Lead Zirconate-Titanate (BPZT) system,” PhD Thesis, Science: Department of Chemistry, 2019.
[64] G. Shirane, S. Hoshino, and K. Suzuki, “X-ray study of the phase transition in lead titanate,” Phys. Rev., vol. 80, no. 6, p. 1105, 1950.
[65] G. Shirane and S. Hoshino, “On the phase transition in lead titanate,” J. Phys. Soc. Jpn., vol. 6, no. 4, pp. 265–270, 1951.
[66] C. Miclea, L. Amarande, C. Tanasoiu, I. Spanulescu, and C. F. Miclea, “Piezoelectric properties of bismuth modified lead titanate ceramics,” in CAS 2005 Proceedings. 2005 International Semiconductor Conference, vol. 2, pp. 271–274, 2005.
[67] N. Ichinose and Y. Fuse, “Anisotropy of piezoelectric properties in the modified $PbTiO_3$ ceramics,” Ferroelectrics, vol. 106, no. 1, pp. 369–374, 1990.
[68] R. Tickoo, R. P. Tandon, K. K. Bamzai, and P. N. Kotru, “Microindentation studies on samarium-modified lead titanate ceramics,” Mater. Chem. Phys., vol. 80, no. 2, pp. 446–451, 2003.
[69] D. Damjanovic, T. R. Gururaja, and L. E. Cross, “Anisotropy in piezoelectric properties of modified lead titanate ceramics,” Am. Ceram. Soc. Bull., vol. 66, no. 4, pp. 699–703, 1987.
[70] N. Ichinose and Y. Fuse, “Anisotropy of piezoelectric properties in the modified $PbTiO_3$ ceramics,” Ferroelectrics, vol. 106, no. 1, pp. 369–374, 1990.
[71] J. Mendiola, B. Jimenez, C. Alemany, L. Pardo, and L. D. Olmo, “Influence of calcium on the ferroelectricity of modified lead titanate ceramics,” Ferroelectrics, vol. 94, no. 1, pp. 183–188, 1989.
[72] H. Fujishita and S. Hoshino, “A study of structural phase transitions in antiferroelectric $PbZrO_3$ by neutron diffraction,” J. Phys. Soc. Jpn., vol. 53, no. 1, pp. 226–234, 1984.
[73] E. Sawaguchi, H. Maniwa, and S. Hoshino, “Antiferroelectric structure of lead zirconate,” Phys. Rev., vol. 83, no. 5, p. 1078, 1951.
[74] A. K. Tagantsev et al., “The origin of antiferroelectricity in $PbZrO_3$,” Nat. Commun., vol. 4, no. 1, pp. 1–8, 2013.
[75] Z. Ren, “Study of Complex Ferroelectric and Antiferroelectric Systems,” PhD Thesis, Science: Chemistry, 2014.
[76] E. P. Smirnova, A. V. Sotnikov, O. E. Kvyatkovskii, M. Weihnacht, and V. V. Lemanov, “Phase evolution in $SrTiO_3$-$PbZrO_3$ solid solution,” J. Appl. Phys., vol. 101, no. 8, p. 084117, 2007.
[77] G. A. Samara, “Pressure and temperature dependence of the dielectric properties and phase transitions of the ferroelectric perovskites: $PbTiO_3$ and $BaTiO_3$,” Ferroelectrics, vol. 2, no. 1, pp. 277–289, 1971.
[78] L. E. Smart and E. A. Moore, Solid state chemistry: an introduction. CRC press, 2012.
[79] A. R. West, Basic solid state chemistry. John Wiley & Sons Incorporated, 1999.

[80] B. H. Toby and R. B. Von Dreele, “GSAS-II: the genesis of a modern open-source all purpose crystallography software package,” J. Appl. Crystallogr., vol. 46, no. 2, pp. 544–549, 2013.
[81] A. R. West, “Bonding in Solids,” Basic Solid State Chem. 2nd Ed West Sussex John Wiley Sons Ltd, pp. 90–95, 1999.
[82] E. Barsoukov and J. R. Macdonald, Impedance Spectroscopy: Theory, Experiment and Applications. Wiley-Interscience, Hoboken, NJ, 2005.
[83] I. P. Parkin, “Basic Solid State Chemistry Anthony R. West 2nd edn. John Wiley & Sons, Chichester, 1999 xvi+ 480 pages.\pounds 24.95 ISBN 0-471-98756-5 (pbk),” Appl. Organomet. Chem., vol. 14, no. 4, pp. 227–228, 2000.
[84] L. Jin, F. Li, and S. Zhang, “Decoding the fingerprint of ferroelectric loops: comprehension of the material properties and structures,” J. Am. Ceram. Soc., vol. 97, no. 1, pp. 1–27, 2014.
[85] R. F. Egerton, Physical principles of electron microscopy, vol. 56. Springer, 2005.
[86] G. W. Stachowiak, A. W. Batchelor, and G. B. Stachowiak, “Surface Micrography and Analysis,” in Tribology Series, vol. 44, Elsevierpp. 165–220, 2004.
[87] D. B. Williams and C. B. Carter, “The transmission electron microscope,” in Transmission electron microscopy, Springer, 1996, pp. 3–17.
[88] R. Guo, L. E. Cross, S. E. Park, B. Noheda, D. E. Cox, and G. Shirane, “Origin of the high piezoelectric response in $Pb(Zr_{1-x}Ti_x)O_3$,” Phys. Rev. Lett., vol. 84, no. 23, p. 5423, 2000.
[89] V. V. Lemanov, E. P. Smirnova, and E. A. Tarakanov, “Ferroelectric properties of $SrTiO_3$-$PbTiO_3$ solid solutions,” Phys. Solid State, vol. 39, no. 4, pp. 628–631, 1997.
[90] V. V. Lemanov, E. P. Smirnova, and E. A. Tarakanov, “Ferroelectricity in $SrTiO_3$: Pb,” Ferroelectr. Lett. Sect., vol. 22, no. 3–4, pp. 69–73, 1997.
[91] V. V. Lemanov, “Phase transitions in $SrTiO_3$-based solid solutions,” Phys. Solid State, vol. 39, no. 9, pp. 1468–1473, 1997.
[92] A. Altomare, C. Cuocci, A. Moliterni, and R. Rizzi, “Indexing a powder diffraction pattern,” 2019.
[93] L. B. McCusker, R. B. Von Dreele, D. E. Cox, D. Louër, and P. Scardi, “Rietveld refinement guidelines,” J. Appl. Crystallogr., vol. 32, no. 1, pp. 36–50, 1999.
[94] B. H. Toby, “R factors in Rietveld analysis: How good is good enough?,” Powder Diffr., vol. 21, no. 1, pp. 67–70, 2006.
[95] M. M. Vijatović, J. D. Bobić, and B. D. Stojanović, “History and challenges of barium titanate: Part I,” Sci. Sinter., vol. 40, no. 2, pp. 155–165, 2008.
[96] C. Pithan, D. Hennings, and R. Waser, “Progress in the synthesis of nanocrystalline $BaTiO_3$ powders for MLCC,” Int. J. Appl. Ceram. Technol., vol. 2, no. 1, pp. 1–14, 2005.
[97] A. Jain, P. KJ, A. K. Sharma, A. Jain, and R. PN, “Dielectric and piezoelectric properties of PVDF/PZT composites: A review,” Polym. Eng. Sci., vol. 55, no. 7, pp. 1589–1616, 2015.
[98] P. K. Panda and B. Sahoo, “PZT to lead free piezo ceramics: a review,” Ferroelectrics, vol. 474, no. 1, pp. 128–143, 2015.
[99] H. E. Weaver, “Dielectric properties of single crystals of $SrTiO_3$ at low temperatures,” J. Phys. Chem. Solids, vol. 11, no. 3–4, pp. 274–277, 1959.
[100] T. Wang, L. Jin, C. Li, Q. Hu, and X. Wei, “Relaxor ferroelectric $BaTiO_3$–$Bi(Mg_{2/3}Nb_{1/3})O_3$ ceramics for energy storage application,” J. Am. Ceram. Soc., vol. 98, no. 2, pp. 559–566, 2015.
[101] X. G. Tang, X. X. Wang, K.-H. Chew, and H. L. W. Chan, “Relaxor behavior of (Ba, Sr)(Zr,Ti)O_3 ferroelectric ceramics,” Solid State Commun., vol. 136, no. 2, pp. 89–93, 2005.

[102] C. Lei, A. A. Bokov, and Z.-G. Ye, “Ferroelectric to relaxor crossover and dielectric phase diagram in the $BaTiO_3$–$BaSnO_3$ system,” J. Appl. Phys., vol. 101, no. 8, p. 084105, 2007.
[103] D. Viehland, S. J. Jang, L. E. Cross, and M. Wuttig, “Deviation from Curie-Weiss behavior in relaxor ferroelectrics,” Phys. Rev. B, vol. 46, no. 13, p. 8003, 1992.
[104] C. A. Randall and A. S. Bhalla, “Nanostructural-property relations in complex lead perovskites,” Jpn. J. Appl. Phys., vol. 29, no. 2R, p. 327, 1990.
[105] R. D. Shannon, “Revised effective ionic radii and systematic studies of interatomic distances in halides and chalcogenides,” Acta Crystallogr. A, vol. 32, no. 5, pp. 751–767, 1976.
[106] I. Grinberg, V. R. Cooper, and A. M. Rappe, “Relationship between local structure and phase transitions of a disordered solid solution,” Nature, vol. 419, no. 6910, pp. 909–911, 2002.
[107] L. Shimoni-Livny, J. P. Glusker, and C. W. Bock, “Lone pair functionality in divalent lead compounds,” Inorg. Chem., vol. 37, no. 8, pp. 1853–1867, 1998.